

TOPICAL REVIEW • OPEN ACCESS

Suspended semiconductor nanostructures: physics and technology

To cite this article: A G Pogosov *et al* 2022 *J. Phys.: Condens. Matter* **34** 263001

View the [article online](#) for updates and enhancements.

You may also like

- [Graphene related materials for thermal management](#)
Yifeng Fu, Josef Hansson, Ya Liu *et al.*
- [Low energy electron microscopy and photoemission electron microscopy investigation of graphene](#)
K L Man and M S Altman
- [Noise temperature in graphene at high frequencies](#)
Raúl Rengel, José M Iglesias, Elena Pascual *et al.*



IOP | ebooks™

Bringing together innovative digital publishing with leading authors from the global scientific community.

Start exploring the collection—download the first chapter of every title for free.

Topical Review

Suspended semiconductor nanostructures: physics and technology

A G Pogosov^{1,2} , A A Shevyrin¹, D A Pokhabov^{1,2}, E Yu Zhdanov^{1,2} and S Kumar^{3,*} 

¹ Rzhnev Institute of Semiconductor Physics SB RAS, 13 Lavrentiev Ave., Novosibirsk 630090, Russia

² Department of Physics, Novosibirsk State University, 2 Pirogov Str., Novosibirsk 630090, Russia

³ Department of Electronic and Electrical Engineering, University College London, Torrington Place, London WC1E 7JE, United Kingdom

E-mail: pogosov@isp.nsc.ru and sanjeev.kumar@ucl.ac.uk

Received 27 August 2021, revised 8 February 2022

Accepted for publication 31 March 2022

Published 25 April 2022



Abstract

The current state of research on quantum and ballistic electron transport in semiconductor nanostructures with a two-dimensional electron gas separated from the substrate and nanoelectromechanical systems is reviewed. These nanostructures fabricated using the surface nanomachining technique have certain unexpected features in comparison to their non-suspended counterparts, such as additional mechanical degrees of freedom, enhanced electron–electron interaction and weak heat sink. Moreover, their mechanical functionality can be used as an additional tool for studying the electron transport, complementary to the ordinary electrical measurements. The article includes a comprehensive review of spin-dependent electron transport and multichannel effects in suspended quantum point contacts, ballistic and adiabatic transport in suspended nanostructures, as well as investigations on nanoelectromechanical systems. We aim to provide an overview of the state-of-the-art in suspended semiconductor nanostructures and their applications in nanoelectronics, spintronics and emerging quantum technologies.

Keywords: suspended, semiconductors, nanostructures, physics, technology, quantum point contact, quantum wire

(Some figures may appear in colour only in the online journal)


1. Introduction

From the viewpoint of electron transport, nanostructures are usually called conductors when their characteristic dimensions, reaching 100 nm or less, significantly exceed molecular dimensions. Nanostructures, however, are still too small for the phenomena we observe in them to be described by

physical laws applicable to micro- and macrostructures. Since the early 1980s, similar structures, which occupy an intermediate position between atomic and macroscopic objects, have been united by the term ‘mesoscopic’. Since then, successive studies of micro- and then nanostructures have demonstrated a range of physical phenomena specific to them. Nanostructures are deservedly considered a very special field of physics, and have grown tremendously over the past few decades.

Typically, semiconductor nanostructures are created on the basis of objects, one of the dimensions of which is already quite small. The most common nanostructure is a 2D electron gas. Nanostructures exhibit unusual properties when their

* Author to whom any correspondence should be addressed.

 Original content from this work may be used under the terms of the [Creative Commons Attribution 4.0 licence](https://creativecommons.org/licenses/by/4.0/). Any further distribution of this work must maintain attribution to the author(s) and the title of the work, journal citation and DOI.

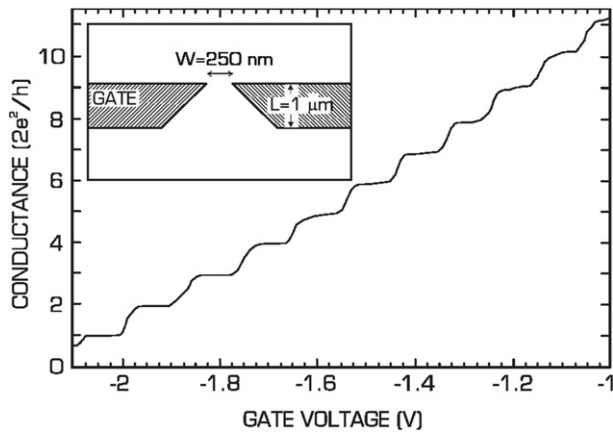


Figure 1. Conductance as a function of gate voltage. Inset: a typical QPC architecture. Reprinted (figure) with permission from [9], Copyright (1988) by the American Physical Society.

characteristic dimensions L become comparable to or less than certain lengthscales characterizing the conductor, which include, for example, the electron phase coherence length L_φ , the mean free path l and the electron wavelength λ [1]. In some cases (for example, at $L < l$), electron transport in them requires fundamentally new approaches, since the local connection between the current density and the electric field is lost, in others, as is well known, quantum interference and spin phenomena play a decisive role. The unusual properties of nanostructures have led to an increased interest in the study of quantum and spin-dependent electron transport, ballistic effects, and adiabatic transport, realized when strong magnetic fields are applied.

In the overwhelming majority of cases, semiconductor nanostructures are manufactured embedded in a substrate. There has, however, been growing interest in studying suspended nanostructures that can be detached from a substrate by selectively etching a sacrificial layer beneath them [2–8]. The technology of manufacturing suspended nanostructures is described in more detail in the subsequent sections for each kind of nanostructures considered in this review. The resulting suspended structures acquire a number of additional properties, such as additional mechanical degrees of freedom, enhanced electron–electron interaction, weakened heat removal into the substrate, etc.

This review will demonstrate that the suspension of nanostructures leads to new effects, thereby expanding the already extensive spectrum of physical effects observed in nanostructures. We will show through this article how the suspension of nanostructures provides a new class of quantum materials which not only possess enhanced physical effects compared to their ordinary non-suspended counterparts but also offer many new avenues for technological advancement.

This review article consists of three main sections each describing a unique nanostructure. The second section is devoted to quantum point contact (QPC), one of the examples of a simple nanostructure, but with a rich set of properties. Suspension-related phenomena connected with the enhancement of the electron–electron interaction, spin-dependent

electron transport, as well as the unusual multi-row transport in a single QPC are discussed. The third section examines the ballistic properties of nanostructures in the form of single and periodical Sinai billiards, dynamical chaos and commensurability effects observed in them, as well as peculiarities of these phenomena arising from suspension. It also includes a review of studies of electron transport in the adiabatic regime observed in quantizing magnetic fields. The features of suspended nanostructures related to the presence of additional mechanical degrees of freedom in them are considered in the fourth section. Such suspended nanostructures capable of performing mechanical vibrations are referred to as nanoelectromechanical systems. The mechanisms of excitation and detection of vibrations, those affecting the resonant frequency and the quality factor are considered. In addition to the influence of electrical parameters on the characteristics of vibrations, the back action is also discussed.

2. Suspended quantum point contacts (QPCs)

2.1. QPC and conductance quantization

QPC is an adiabatic constriction in a two-dimensional electron gas (2DEG), whose width is comparable to the Fermi wavelength of an electron and the length is much shorter than its mean free path. QPC is, perhaps, the simplest nanostructure demonstrating quantum transport. From the experimental point of view, QPC is a quasi-1D conductor which, like a quantum wire, has quantum confinement in the transverse direction, and is also characterized by adiabatic and ballistic transport in the longitudinal direction. The typical dependence of the QPC conductance on the channel width, which can be controlled, for example, using the voltage applied to split gates, is a stepped curve with plateaus at quantized values of conductance that are multiples of $2e^2/h$ (see figure 1) [9, 10]. The conductance quantization can be explained within the framework of the model of an ideal reflectionless one-dimensional (1D) electron waveguide connecting the source to the drain. The contribution of each electron mode to the conductance is $2e^2/h$, where the factor 2 is related to spin degeneracy. This universal result, independent of the dispersion law $\varepsilon(p)$, follows from the fact that the single-mode contribution to the current between source and drain having electrochemical potentials μ and $\mu + \Delta\mu$ is equal $I_0 = 2e \int_{\mu}^{\mu + \Delta\mu} \rho_{1D}(\varepsilon) \cdot u(\varepsilon) \cdot d\varepsilon$ (with spin taken into account), where upon multiplying the 1D density of states $\rho_{1D}(\varepsilon) = \frac{1}{h} \frac{\partial p}{\partial \varepsilon}$ and velocity $u(\varepsilon) = \frac{\partial \varepsilon}{\partial p}$, the dispersion law is canceled, and $I_0 = 2 \frac{e}{h} \Delta\mu$. The conductance, G of a quasi-1D channel with N filled subbands is determined by the ratio of the total current NI_0 to the applied voltage $\Delta\mu/e$:

$$G = N \times 2 \frac{e^2}{h}. \quad (1)$$

The model described above explaining integer quantization of conductance within a 1D channel is based on the single-particle approach.

There are many factors affecting the observation of conductance quantization, such as temperature, the shape and size of the quantum channel, the strength of the confining potential,

etc. There are optimal experimental conditions for observing the effect. Violation of these conditions smears the plateaus. First of all, a non-zero temperature leads to a non-zero probability of tunneling via the high-energy subbands as a result of thermal smearing of the Fermi–Dirac distribution. For reliable observation of the conductance quantization, the temperature should satisfy the condition $T \ll \Delta E/4k_B$, where ΔE , where ΔE is 1D-subband energy spacing, k_B is the Boltzmann constant [11]. The transport through the quantum channel should be ballistic. To prevent impurity scattering inside the channel, length L and width W of the quantum channel must be small compared to the mean free path l : $L, W \ll l$. Another important condition is the adiabaticity of the channel. The adiabaticity criterion is formulated as $dW/dx \lesssim 1/N(x)$, with $N(x) \approx k_F W(x)/\pi$ is the local number of subbands [12]. The violation of the adiabaticity results in mixing of the subbands. At the ends of the quasi-1D channel, where it is connected to 2DEG, partial reflection of electron waves [11] can occur. Backscattering and intersubband scattering can prevent the observation of conductance quantization. The shape of the potential is also important for observing the effect. Büttiker solved the problem of saddle-potential transmission in [13]. The ratio between the width and length of the QPC, optimal for observation of the plateaus, has been determined [14]. The strength of the potential also plays a role in observing the effect. For example, e–e interaction, especially in the case of shallow confinement, can dramatically change the electron spectrum [15].

It should be noted that, in addition to the integer quantization as described above, in the study of nonlinear effects measured with a large enough dc source–drain bias, half-integer conductance plateaus $G = \frac{m}{2} \times 2e^2/h$, $m = 1, 3, 5 \dots$ are observed. These features are also explainable in the framework of the single-particle approach. In this mode, the electrochemical potentials of the source and drain differ significantly, so that the number of subbands emerging from the source and drain is integer, but different [16–18]. In this case, when a dc source–drain voltage is applied corresponding to the energy difference between the two subbands, half-integer quantization plateaus are observed: 1.5, 2.5, 3.5, etc (in units of $2e^2/h$).

Electron transport through QPC has been a subject of immense interest over the past three decades for fundamental quantum physics. Of particular interest has remained the investigations on the many-body aspects of electron transport in QPCs. In other words, considerable interests have been associated with the features of conductance observed in the linear or Ohmic regime at values other than the integer multiples of $2e^2/h$. In most cases, the origin of such features is beyond the scope of the single-particle model which has aroused discussions on developing new theoretical models. These include, for example, the so-called ‘0.7-anomaly’—a feature of conductance observed at a value of $0.7 \times 2e^2/h$, which has been widely studied both experimentally and theoretically [19–29]. There are many theoretical attempts to unravel the nature of the ‘0.7-anomaly’, but despite the variety of proposed explanations, all models have in common that this feature cannot be described within the framework of a single-particle approach, but has a multiparticle origin, i.e., associated with electron–electron (e–e) interaction [30, 31].

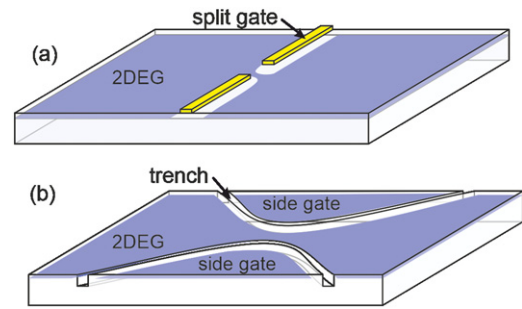


Figure 2. QPC formation methods: (a) split gate, (b) trench-etching method. Areas of non-depleted 2DEG are shown in blue.

In addition, it is important to mention the anomalous conductance plateau occurring at $0.25 \times 2e^2/h$ in the presence of a large dc source–drain bias. Based on the non-linear transport predicted by Glazman and Khaetskii [16], additional conductance plateaus at half integer of $2e^2/h$ appear as the 1D channel is widened. As discussed before, this should give rise to additional half conductance plateaus in non-linear transport appearing at 0.5, 1.5, 2.5, 3.5 etc in units of $2e^2/h$. However, experimentally, instead of a plateau at $0.5 \times 2e^2/h$, a strong, robust plateau usually occurs at $0.25 \times 2e^2/h$, which is explained to arise from the lifting of spin and momentum degeneracy. The spin behavior of the 0.25-anomaly was tested under a strong in-plane magnetic field of 16 T and it remained unchanged [32], thus confirming the feature to arise due to spin polarization within the 1D channel. The mechanism of spin polarization in this case remains unclear, as does the absence of other plateaus of conductance quantization, multiples of $0.25 \times 2e^2/h$ (0.5, 0.75, 1, 1.25, etc, in units of $2e^2/h$) in nonlinear transport.

The e–e interaction plays a crucial role in electronic transport in the QPC. One of its manifestations, in addition to the 0.7-anomaly, is the formation of the 1D Wigner crystal. In a low-density 1D system when the confinement is sufficiently weak, a line of 1D electrons undergoes a transformation into a zigzag and eventually into a two row situation on further reduction in carrier concentration. Experimentally, a two row situation is manifested by a missing first plateau at $2e^2/h$, and the $4e^2/h$ becomes the new ground state, [33–39]. Also, the zigzag assembly of 1D electrons or the 1D Wigner crystal, which happens just before the two rows formation, cannot be measured by the conventional conductance measurements, which was therefore imaged using transverse magnetic focusing technique [40]. Recently, in weakly confined 1D quantum wires in the regime of 1D Wigner crystallization, enhancing the asymmetry in confinement potential led to the observation of a wide variety of fractional conductance plateaus, both with odd and even denominator, ($1/6, 2/5, 1/5, 1/2$, etc in units of e^2/h) in the absence of a quantizing magnetic field [41, 42], hitherto unexpected phenomena. These fractional states were similar to those seen previously in the fractional quantum Hall effect, though have a different origin.

Another interesting feature associated with 1D based systems is the exploitation of spin–orbit phenomena. QPCs were utilized to the spin polarization electrically which does not

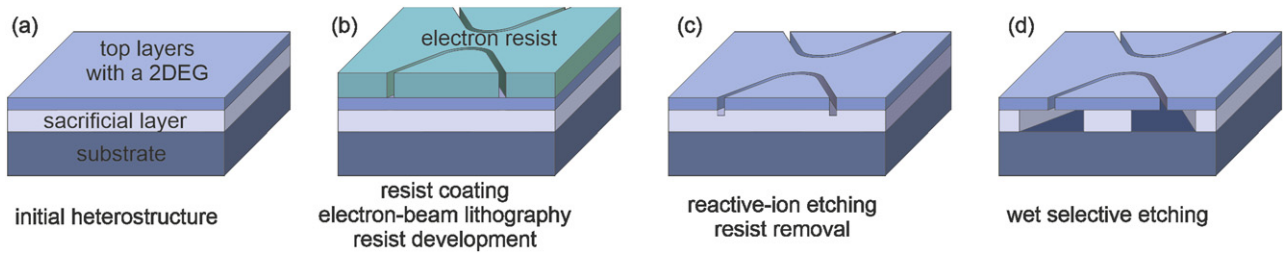


Figure 3. Basic steps used to create a suspended nanostructure. (a) Initial heterostructure grown using molecular-beam epitaxy containing a sacrificial layer. (b) The heterostructure is coated by electron resist (for example, PMMA). The resist is patterned using electron-beam lithography and developed. (c) The structure undergoes anisotropic reactive-ion etching (for example, in $\text{BCl}_3:\text{Ar}$ plasma) to a depth larger than the thickness of the top layers. After that, the resist is removed. (d) The structure is immersed into wet etchant (such as $\text{HF}:\text{H}_2\text{O}$ or $\text{HCl}:\text{H}_2\text{O}$ mixture). The sacrificial layer is attacked via the trenches in the top layers and selectively removed, resulting in suspension of the top layers.

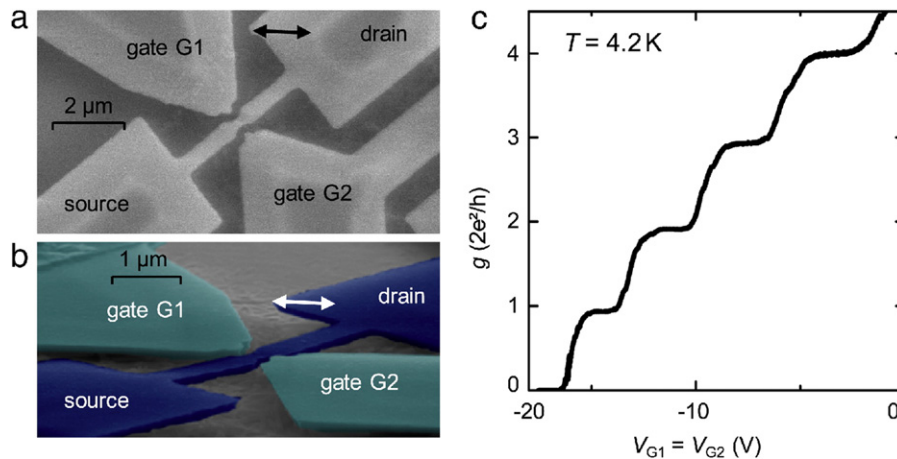


Figure 4. (a) SEM image of suspended QPC. (b) Side view of the device under a tilt angle of 75° . At the position marked by a white arrow, the full underetch of approximately $2\ \mu\text{m}$ is visible (the black arrow in (a)). (c) Two-terminal differential conductance g in units of $2e^2/h$ as a function of the gate voltages $V_{G1} = V_{G2}$. Reprinted from [60], Copyright (2010), with permission from Elsevier.

require the application of an external magnetic field [43]. The possibility of electrical manipulation of the electron spin opens up broad prospects for applications of future semiconductor spintronics [44], including the creation of injectors and spin detectors [45], as well as a semiconductor field effect spin transistor [43]. One of the possibilities to achieve spin polarization in the QPC is to apply an electric field to the QPC channel, which in turn leads to the so-called lateral spin-orbit coupling (LSOC) [46–48], which has been shown to result a conductance plateau at $0.5 \times 2e^2/h$. In addition, the spin polarization associated with the 0.7 conductance anomaly and direct observation of exchange driven spin interactions within the 1D channel were confirmed using transverse electron focusing technique [49–51].

2.2. Device fabrication

QPCs are typically created either by applying a voltage to a split metal Schottky gate or by using lithographic trenches separating the conductive channel from the side gates (see figure 2). In contrast to the QPC with a split gate, where the gate forms the confining potential and simultaneously controls it, in the QPC with side gates, the channel is formed lithographically by means of trenches, which leaves the possibility of

using side gates for modifying the confining potential, allowing them to be used almost independently and to apply a rather large voltage difference between them for introducing high asymmetric confinement potential for investigating interaction effects within the 1D channel. It was previously shown that applying a voltage difference between the side gates allows the creation of lateral electric fields sufficient to induce spin polarization in both InAs [46] and GaAs [52] based QPCs due to the LSOC effect. Another advantage of trench-type structures is that they allow independent application of the gate voltage, and hence the study of conductance as a function of two independent gate voltages [53, 54]. Such measurements reveal an unusual multichannel electron transport characterized by quantised conductance of individual channels within a single QPC [53–55]. Moreover, the channels can function independent of each other and demonstrate the effects of interaction between them. Another significant advantage is that the etching technique gives rise to strong lateral confinement with 1D subband energy separations of $5\text{--}20\ \text{meV}$ [21, 56, 57], which gives a higher energy resolution and allows one to observe the conductance features at higher temperatures. The trenched defined QPCs could provide an additional advantage over the split-gate devices in relation to studying the effects associated

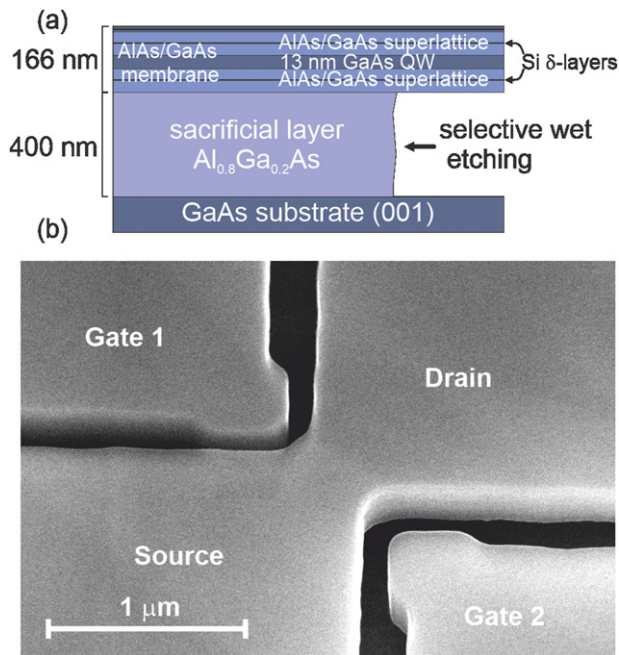


Figure 5. (a) GaAs/AlGaAs heterostructure with sacrificial layer and 2DEG. (b) SEM image of the suspended QPC obtained with an electron beam tilted at an angle of 30° to the surface. An area of approximately $1 \mu\text{m}$ wide on both sides of the lithographic trenches is suspended, so that the entire area shown in the figure is suspended, including the channel and adjacent source, drain, and gates regions, which remain attached to the sacrificial layer and substrate away from the QPC. Reprinted from [74], with the permission of AIP Publishing.

with e–e coupling, since metal gates located near the channel could shield the Coulomb interactions [15].

Suspended QPCs are mainly created by means of trenching (or etching technique). In addition to defining the QPC shape, the trenches provide access for the liquid etchant to the sacrificial layer. Usually the trenches are created by electron beam lithography and subsequent reactive-ion etching. The sacrificial layer are removed from under a nanostructure through open trenches by selective wet etching. Water solutions of HF or HCl acid are often used as an etchant. The main technological steps of creating the suspended nanostructures are illustrated in figure 3. The width of the suspended areas can be controlled with an optical microscope. There have been attempts to make suspended QPCs using metallic split gates. Such structures indeed demonstrated a pronounced quantization of conductance in the first few depletion cycles, however, in subsequent cycles, the quantization disappeared [58]. It was suggested that tunneling from the gates into the 2DEG affected the local electrostatic potential which possibly quenched the conductance quantization [59]. A freely suspended QPC—narrow etched constrictions, capacitively controlled via in-plane side gates—was investigated in reference [60] where a pronounced conductance quantization with large 1D subband energy separations of 10 meV was achieved (see figure 4). It may be noted that all attempts to create and experimentally study suspended QPCs so far have been made solely on the basis of GaAs/AlGaAs heterostructures, where a high carrier mobility ensures ballistic transport.

Suspended QPCs possess all the key properties of suspended nanostructures, namely, weakened heat transfer to the substrate, modified phonon spectrum, mechanical degrees of freedom, and enhanced e–e interaction. Note that the first suspended quantum wires were used specifically for the measurement of the quantum of thermal conductance [61], predicted for phonon transport in a ballistic 1D channel adiabatically coupled to reservoirs [62, 63]. In suspended QPCs, a giant acoustoelectric current driven by surface acoustic waves was observed. The magnitude of this current was much larger than that of a 2DEG [64, 65], due to the enhanced interaction between the suspended 2DEG and the surface acoustic wave. Some features of the acoustoelectric current, for example, negative current near pinch off, are attributed to enhanced backscattering caused by the strong electron–phonon coupling in suspended systems. Photoinduced current has also been studied in suspended submicron quasi-2D channels [66]. In addition, suspended QPCs were used as detectors of mechanical vibrations of the resonator coupled with it [67, 68]. The mutual influence of mechanical degrees of freedom and electrical properties of suspended QPCs will be reviewed in the section ‘nanoelectromechanical systems’. It may be noted that the suspension of QPCs in majority of cases preserves the fundamental characteristics of a 1D system, i.e., conductance quantization in units of $2e^2/h$. In this section, we will mainly focus on the features of conductance quantization caused by the enhancement of the e–e interaction and related phenomena.

2.3. e–e coupling enhancement in suspended QPC

An important difference between suspended structures and their non-suspended counterparts is the enhanced e–e interaction resulting from the selective etching of a part of the screening medium with a high dielectric constant from under the structure, as a result of which it partially ‘blocks’ the electric field lines inside the suspended membrane. The effect of amplification of e–e coupling was first predicted theoretically [69, 70].

As shown by numerical calculations (see detailed discussion below), the enhancement factor of the Coulomb interaction of two electrons due to the above-described effect of membrane suspension becomes more and more noticeable with increasing distance r between them, and at large distances $r \gg t$, where t is the membrane thickness, reaches quantity $(\epsilon + 1)/2$, where ϵ is the dielectric constant. Nevertheless, as will be shown below, the effects associated with this enhancement also play a noticeable role at a sufficiently high 1D electron density in the QPC channel, when the distance between neighboring electrons is less than the indicated scale. Enhancement of the e–e interaction leads to a number of interesting features. For example, a significant increase in the charging energy (by a factor of 4 to 170 K in temperature units) of a quantum dot in the Coulomb blockade mode after suspension was found [71, 72]. The enhancement of the e–e interaction is also confirmed by other experiments with suspended nanostructures [73].

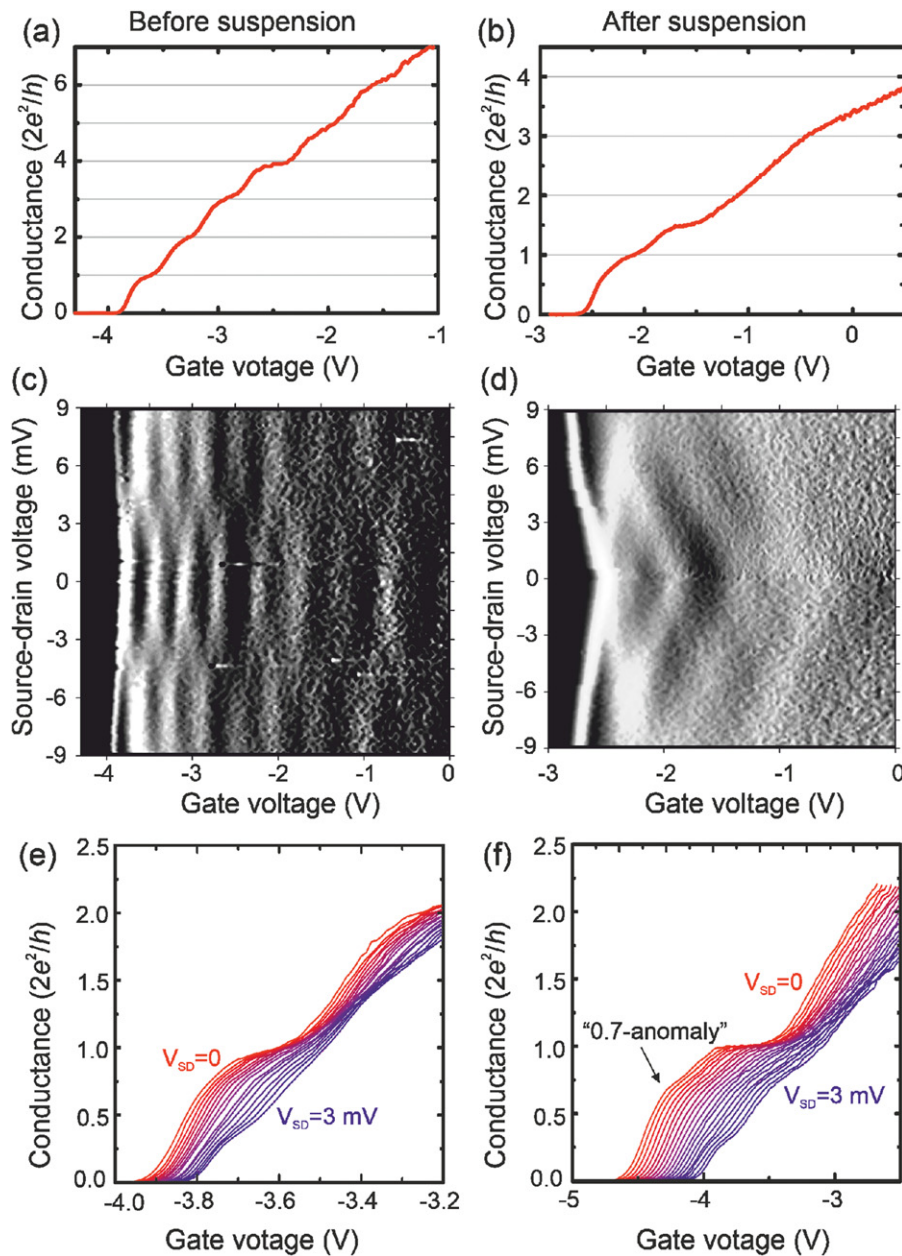


Figure 6. Conductance quantization (a) before and (b) after the suspension of QPC. A grayscale plot of transconductance as a function of gate and source–drain voltage (c) before and (d) after the suspension. Dark regions correspond to plateaus, and to the transconductance values close to zero, while the light regions correspond to the risers between them. Conductance plateaus evolution with a dc source–drain voltage: ‘0.7-anomaly’ unobserved (e) before suspension becomes observable (f) after suspension of QPC. The series of conductance characteristics of suspended QPC (f) were measured at non-zero gate voltage difference $\Delta V_G = 6$ V. Reprinted from [74], with the permission of AIP Publishing.

The effect of suspension of QPC on the conductance characteristics were investigated [74]. The QPC conductance was investigated by performing identical electrical measurements in the same experimental sample before and after the suspension. This allowed to carry out a comparative analysis of the results obtained before and after suspension of the QPC from the substrate. It was shown that suspended QPCs, as well as traditionally studied non-suspended ones, exhibit conductance quantization; however, when detached from the substrate, the ‘0.7-anomaly’ of conductance becomes more pronounced, which is most likely associated with increased

e–e interaction after suspension. Some details of this work are given below.

The QPC was a smooth 800 nm wide constriction in a 2DEG forming a channel with two in-plane side gates (gate 1 and gate 2) separated from the channel by lithographic trenches created by electron beam lithography followed by anisotropic reactive-ion etching (see figure 5). This QPC can be referred to as deep-etching structures, since the trenches were etched to the depth of the entire heterostructure, to the sacrificial layer. After measurements were carried out on a non-suspended QPC, the sacrificial layer was removed from

under the nanostructure using selective wet etching, and conductance measurements were repeated again in the suspended QPC.

Prior to suspension, the QPC exhibited a conventional conductance quantization pattern in units of $2e^2/h$. In figure 6(a) six plateaus can be distinguished. Conductance quantization was also observed after the suspension (see figure 6(b)), however only two plateaus are clearly distinguishable, with the second observed at a non-integer value of $1.5 \times 2e^2/h$, although the first conductance step is observed at the usual value of $2e^2/h$. Figures 6(c) and (d) show an evolution of conductance plateaus with applying dc source–drain voltage V_{SD} . Dark regions in figures 6(c) and (d) correspond to conductance plateaus or, the same, zero transconductance, i.e., numerical derivative of conductance with respect to gate voltage. The plateaus had a form of diamonds whose size along the V_{SD} axis corresponds to the energy distance between the levels of the transversal quantization [16–18], and practically did not change when suspended. When $|V_{SD}| > 3$ mV, the integer plateaus $N \times 2e^2/h$ disappeared, and half-integer plateaus $(N - 1/2) \times 2e^2/h$ were observed instead. Thus, the intersubband distance is approximately $\Delta E \approx 6$ meV, which is typical for the trench-type QPCs [21].

In order to demonstrate the effect of enhancing the Coulomb interaction located in the middle of a t -thick semiconductor membrane, consider the potential in this plane created by one of the electrons at the location of the other electron. In the case of a non-suspended membrane (see figure 7(a)), the electrostatic potential at a distance r from the electron is the sum of the potential of the electron itself and the charge of the image located at a point symmetrical with respect to the membrane surface:

$$\varphi_1(r) = -\frac{e}{4\pi\epsilon\epsilon_0 r} \left[1 + \frac{\epsilon - 1}{\epsilon + 1} \frac{1}{\sqrt{1 + (t/r)^2}} \right], \quad (2)$$

where e is the electron charge and ϵ_0 is the vacuum permittivity. In the case of a suspended membrane (see figure 7(b)) infinite number of image charges contribute to electrostatic potential:

$$\varphi_2(r) = -\frac{e}{4\pi\epsilon\epsilon_0 r} \left[1 + 2 \sum_{n=1}^{\infty} \left(\frac{\epsilon - 1}{\epsilon + 1} \right)^n \frac{1}{\sqrt{1 + (nt/r)^2}} \right]. \quad (3)$$

The ratio of the expressions (3) and (2) for $\epsilon \approx 13$ is shown in figure 7(c).

The distance r_{ee} between electrons in the QPC channel can be estimated from the 2D electron density as $r_{ee} \approx n_s^{-1/2} \approx 13$ nm or from the 1D density of states and the inter-subband energy distance $\Delta E \approx 6$ meV as $r_{ee} \approx 17$ nm, which at $t = 166$ nm corresponds to the parameter $r_{ee}/t = 0.07$ – 0.10 . Calculated by formulae (2) and (3), the ratio of the potentials of an electron in a suspended and a non-suspended membrane gives an increase in the e–e interaction due to suspension by about 1.3 times. A significant gain can be expected for long-range interaction (see figure 7(c)). Unlike 3D and 2D electron gases, long-range interaction screening in 1D is weak [75, 76],

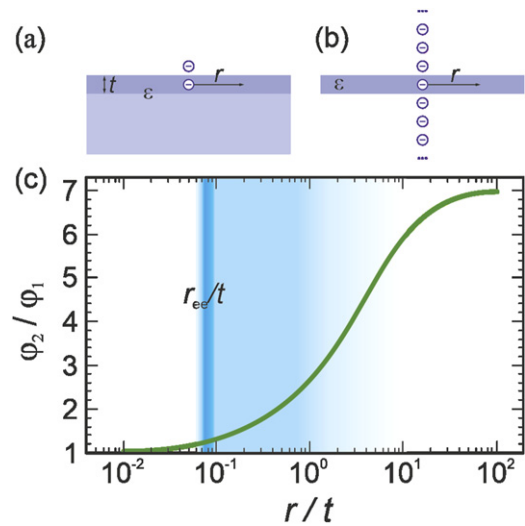


Figure 7. Method of image charges in (a) non-suspended and (b) suspended membrane with a 2DEG. (c) The ratio of the potentials created by an electron in a suspended membrane φ_1 and a non-suspended structure φ_2 as a function of the distance r from it.

and can manifest itself noticeably on the QPC length scales. The characteristic size of the 1D region in the QPC in the present case was about 200 nm. The e–e interaction at such distances is amplified by 3 times. It should be noted that even small changes in e–e coupling energy can make ‘0.7-anomaly’ much more noticeable. This effect is experimentally demonstrated in reference [20] by comparing samples with a 2D electron density that differs by a factor of 1.3, which corresponds to a change in the ratio of the interaction energy of neighboring electrons to their kinetic energy by only a factor of about $\sqrt{1.3} \approx 1.1$.

Strong e–e interactions can lead to the Wigner crystallization [15]. The formation of a 1D Wigner crystal in QPC does not show up directly in conductance measurements. However, a phase transition in a 1D Wigner crystal, the so-called ‘string-zigzag’ transition [77], resulting from softening of the confinement potential and (or) a decrease in the electron density, is recorded in conductance measurements as the weakening or disappearance of the first conductance plateau, and the new ground state corresponds to the conductance $4e^2/h$, the higher plateaus remained unaffected [33, 34, 39]. It is known [15] that a 1D Wigner crystal exists when the characteristic value of the energy of the Coulomb interaction of electrons is much greater than their kinetic energy. This condition can be written in the form $n_{1D}a_B \ll 1$, where $a_B = 10.3$ nm is the effective Bohr radius for gallium arsenide. We can expect a weakening of this condition due to the presence of image charges. In our case, $n_{1D}a_B \approx 0.62$, and we cannot say with certainty whether a Wigner crystal exists in any form (in reference [33], the value of $n_{1D}a_B$ was 0.3).

It was suggested that a 1D Wigner crystal transforms into a quasi-1D ‘zigzag’ structure when the characteristic energy of its interaction is comparable to the confinement potential energy [78]. In the case of the usual Coulomb interaction, this occurs when the condition $n_{1D}r_0 > 0.78$ [77] is satisfied,

where $r_0 = \sqrt[3]{e^2 \hbar^2 / 2\pi \epsilon \epsilon_0 m^* \Delta E^2}$ is the characteristic length scale of the transverse displacement at which the Coulomb interaction between neighboring electrons becomes comparable to the confinement potential ΔE , ϵ_0 is vacuum permittivity, m^* is effective electron mass. For suspended QPC [74], $r_0 \approx 22$ nm and $n_{1D} r_0 \approx 1.3$, i.e. the condition for the formation of the ‘zigzag’ is fulfilled. In general, the enhancement of the e–e interaction as a result of suspension makes both the formation of a Wigner crystal and its transformation into a ‘zigzag’ more probable, although the experimental results obtained cannot be considered as evidence of such a spatial ordering of electrons. This would require further experimental investigations, perhaps using transverse electron focusing to image the zigzag arrangement [40].

Another interesting effect associated with suspension is the appearance of an energy barrier at the interface between suspended and non-suspended 2DEG regions. The barrier height can be estimated using expressions (2) and (3) as $\frac{e}{4\pi\epsilon\epsilon_0 t} \left[2 \ln \left(\frac{\epsilon+1}{2} \right) - \left(\frac{\epsilon-1}{\epsilon+1} \right) \right] \approx 2$ meV [74], while the Fermi energy in 2DEG, calculated from the concentration and density of states, is 20 meV. The existence of such a barrier was confirmed experimentally [79].

Recently, it was shown theoretically that the e–e interaction in thin films can have qualitative differences, manifested in the attraction and pairing of electrons in certain spin states [80, 81]. As a rule, the observation of these effects is prevented by suppression of the e–e interaction by environment with high dielectric constant. So, freely suspended structures are promising systems for the experimental observation of spin–orbit-driven electron pairing effect.

2.4. Lateral spin–orbit coupling

The spin-split half-integer plateau $0.5 \times 2e^2/h$, the appearance of which is associated with the lifting of spin degeneracy, is of considerable interest due to their potential for spintronics. Generally, the spin degeneracy can be removed, for example, by an applied magnetic field. However, spin splitting can also occur in the absence of an applied external magnetic field, in an effective magnetic field arising due to spin–orbit coupling (SOC). SOC is characteristic both for bulk III–V materials, in which there is no center of inversion,—the Dresselhaus effect [82] and for quantum wells based on them, in which the asymmetry of the heterostructure in the growth direction leads to the presence of a built-in electric field—the Rashba effect [83]. SOC in 1D semiconductor structures has been widely studied [84–90]. A possibility to manipulate the electron spin by purely electrical means [91] without any ferromagnetic materials and external magnetic field seems attractive for future spintronics devices [44], including the creation of injectors and spin detectors [45], as well as a semiconductor field-effect spin transistor [43]. It was shown earlier that the electron spin in a QPC can be controlled via LSOC effect caused by lateral electric field applied to QPC by means of side gates [46–48, 92–95]. This effect has been steadily observed in InAs-based QPCs, in which g -factor is high. It was previously found that observation of the LSOC effect requires the asymmetry in the

confinement potential and strong e–e coupling. LSOC leads to splitting of spin subbands in the wave vector domain while preserving their energies unsplit [43]. The e–e interaction, in turn, makes it possible to move the spin subbands apart in energy [47] and thus to observe the effect experimentally.

Numerical calculations, performed by means of non-equilibrium Green’s function method, show that strong e–e interaction plays a more important role [47] than the strength of the SOC (g -factor value) in observing the lateral-electric-field-induced spin polarization. LSOC is just a trigger of spontaneous spin imbalance, while strong e–e coupling enhances the imbalance and results in the strong spin polarization [96]. Therefore, this effect may be expected in GaAs-based QPCs as well. It is important to note that the spin coherence length in GaAs is much higher than in InAs [97], and for practical applications, the prospect of controlled spin polarization due to the LSOC mechanism in GaAs-based structures seems to be more interesting. The observation of a half-integer conductance anomaly in GaAs-based QPCs due to LSOC was reported [98], but scattering by surface roughness at the channel edges [99] did not show the usual integer conductance quantization. The absence of integer plateaus does not allow one to draw a convincing conclusion that the discussed half-integer plateau has a spin nature. A variety of magnetic impurity effects such as the Kondo effect do give rise to a conductance feature close to the $0.5 \times 2e^2/h$.

Note that there are also other reports where the observation of a $0.5 \times 2e^2/h$ plateau in GaAs QPCs not associated with the LSOC mechanism are discussed. A 0.5-structure in zero magnetic field was observed in symmetric GaAs QPCs having a rather long length ($l = 2$ μm) [100], as well as in symmetric 1D quantum wires based on GaAs/AlGaAs heterostructures with a double quantum well [101]. In addition, the pronounced 0.5 conductance plateau was reported when the potential in the channel was tuned symmetrically by low-temperature probe microscopy [102]. Also, a 0.5-conductance anomaly was observed in zero magnetic field in GaAs QPCs with asymmetric split gate geometry [103]. The occurrence of a plateau at $0.5 \times 2e^2/h$ with ‘small distortion of the confinement caused by asymmetrical biasing of the split gates’ is also was reported in reference [36].

The LSOC effect in suspended GaAs-based QPCs was reported in reference [52]. The observed effect manifests itself in the experiment as the appearance of an additional half-integer plateau $0.5 \times 2e^2/h$ in addition to the integer ones when an asymmetric voltage is applied between the side gates in zero magnetic field. The suspended QPCs [52] based on GaAs/AlGaAs heterostructures represent adiabatic constrictions with a lithographic width of 800 nm, equipped with side gates separated from the channel by trenches 150 nm wide. The QPC channel was oriented in the crystallographic direction $\langle 110 \rangle$. The LSOC effect in suspended QPCs was demonstrated at 4.2 K. To create spin polarization in the channel between the gates, an asymmetric voltage $\Delta V_G = V_{G1} - V_{G2}$ was applied. All measurements were carried out in the same way in the samples before and after suspension.

At $V_G = V_{G1} = V_{G2}$, the conductance of the QPC as a function of V_G shows integer quantization. A grayscale plots

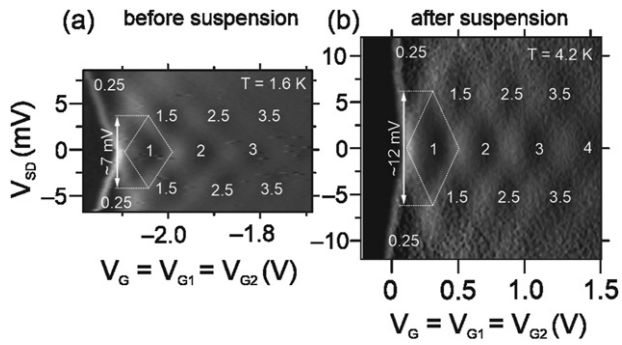


Figure 8. A grayscale plot showing transconductance $\partial G/\partial V_G$ as a function of source–drain voltage V_{SD} and symmetric gate voltage $V_G = V_{G1} = V_{G2}$ (a) before and (b) after suspension of QPC. Dark regions correspond to plateaus. Numbers on the plots indicate the conductance in $2e^2/h$ units. Reprinted from [52], with the permission of AIP Publishing.

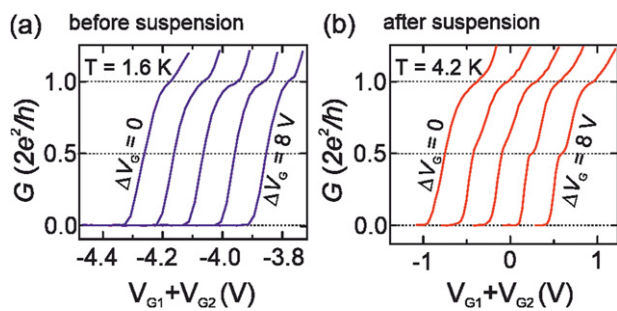


Figure 9. Conductance characteristics (a) before and (b) after suspension. Different curves correspond to different values of ΔV_G , ranging from 0 to 8 V. Reprinted from [52], with the permission of AIP Publishing.

of transconductance $\partial G/\partial V_G$ versus source–drain voltage V_{SD} and symmetrically applied voltages V_G are presented in figure 8 before and after suspension. In both cases, there is a ‘classical’ picture, although there is a striking difference in the size of diamonds along the V_{SD} axis corresponding to the 1D subbands separation [16, 18]. As a result of the suspension, the subband energy separation increases by a factor of approximately 1.7, from 7 meV to 12 meV. In addition to changing the vertical size of the rhombus, the horizontal size of the rhombuses has also changed, approximately 4 times. This is due to changes in the mutual capacitance between the side gate and the QPC conductive channel due to their separation from the high dielectric substrate ($\epsilon \approx 13$).

Figure 9 presents the conductance characteristics before and after suspension. Applying an asymmetric voltage to the side gates $\Delta V_G \neq 0$ of the suspended QPC gives rise to an anomalous quantization plateau $0.5 \times 2e^2/h$, whereas in the sample before suspension, no anomalous conductance quantization plateaus were observed.

Figure 10 shows the evolution of the conductance plateaus in the suspended QPC versus the source–drain voltage V_{SD} at a fixed voltage difference between the side gates $\Delta V_G = 8$ V. The grayscale plot of transconductance $\partial G/\partial(\Sigma V_G)$ in figure 10(a) shows areas that can be identified as $0.5 \times 2e^2/h$ and $0.85 \times 2e^2/h$ [21, 104], which were not observed

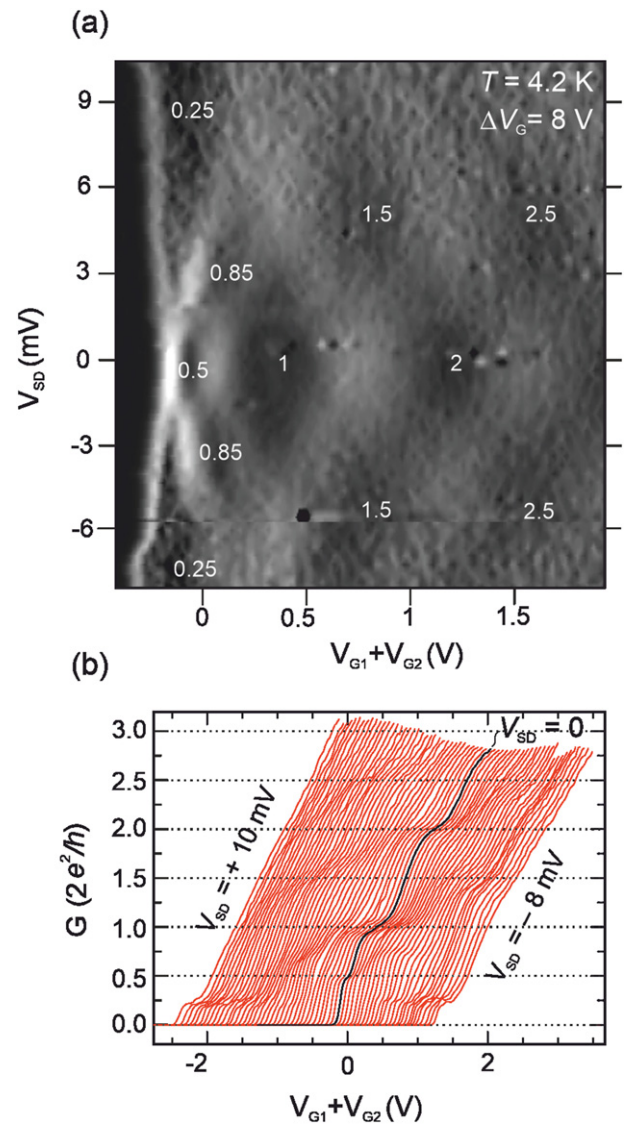


Figure 10. (a) Transconductance $\partial G/\partial(\Sigma V_G)$ as a function of gate voltage sum $\Sigma V_G = V_{G1} + V_{G2}$ and source–drain voltage V_{SD} . (b) Conductance characteristics at different values of V_{SD} ranging from -8 to $+10$ V. Reprinted from [52], with the permission of AIP Publishing.

at $\Delta V_G = 0$ (see figure 5(b)). A plateau of $0.5 \times 2e^2/h$ is observed at V_{SD} , while a plateau of $0.85 \times 2e^2/h$ appears only in the nonlinear regime at $V_{SD} \approx \pm 3$ mV. To be note that all the features in the grayscale plot in figure 10(a) are similar to the results obtained in reference [105] in the presence of a strong in-plane magnetic field of 12 T, which assured that the 0.5 plateau was spin polarized. Thus, the appearance of a $0.5 \times 2e^2/h$ plateau in zero magnetic field in an asymmetrically biased suspended GaAs-based QPC can be expected to arise from the LSOC effect.

Some recent reports have shown investigations where the gate controlled spin polarization have been carried out including the underlying theory. Recently, when studying InAs-based QPCs [106], a fourfold increase in the width of the spin plateau $0.5 \times 2e^2/h$ was found with a threefold increase in the QPC length at a given width. It was suggested that this may be due to the increased role of the e–e interaction in longer QPCs

[107]. Further the effect of channel width on the 0.5 conductance plateau was studied in an InAs-based QPC [108]. It was shown experimentally that the 0.5 plateau became more pronounced with decreasing QPC width. It was argued that with a decrease in the QPC width, first, the multimodeness decreases (i.e. with increase in the intersubband gap) and, second, the electron concentration decreases, as a result of which the electrostatic screening of the e–e interaction is weakened. Note that at the moment the dependence of the width of the plateau $0.5 \times 2e^2/h$ on the geometric proportions has been investigated only in QPCs based on InAs and only in the case of non-suspended samples. Recent theoretical work also discuss the use of InAs-based QPCs with four side gates arranged in pairs on both sides of the microconstriction [96, 109, 110] to enhance the lateral spin–orbit effect. In this configuration, an asymmetric voltage is applied to the two gates closer to the source, inducing spin polarization, and a symmetrical voltage is applied to the other two gates closer to the drain. By adjusting this voltage, the spin polarization effect was shown to get pronounced.

2.5. Multichannel electron transport

As noted above, a significant difference between trench-etched from gate-defined QPCs is the ability to apply sufficiently large voltage differences between the side gates ΔV_G . The study of conductance in suspended trench-etched GaAs-based QPC at sufficiently large ΔV_G in addition to observation of lateral-electric-field-induced spin polarization [52] revealed an unusual multichannel transport mode in a single QPC [53]. Conductive channels, as will be shown below, are formed along the lithographic trenches.

Note that conductive edge channels can occur in systems with strong SOC. Such channels can have both topological [111, 112] and non-topological origin [113–115]. For example, the occurrence of parallel channels near side walls of trenches was observed in InSb trench-type QPC [116]. However, the mechanism for the formation of additional channels in GaAs QPCs is uniquely different from the mechanism for the formation of topological or trivial edge states, since in GaAs the Fermi level is pinned in the middle of the band gap at the lithographic edges. In addition, GaAs cannot be classified as a material with strong SOC. At the moment, the nature of the appearance of additional conductive channels in GaAs QPCs is not completely understood and, probably, lies in the specific electrostatic conditions that are realized in the QPC as a result of the etching of trenches.

In general, double-channel electron transport in QPCs has been studied in some detail earlier. There are reports where the double-channel structure was artificially incorporated into the very structure of the samples. Such double-channel structures include vertically aligned paired QPCs [101, 117, 118] based on double quantum well heterostructures and laterally paired QPCs [119, 120]. Experiments seem interesting in which the two-channel structure of electron transport was not initially incorporated into the architecture of the samples, but arose as a result of spontaneous electron redistribution due to electrostatic repulsion. The transition from single-layer to

double-layer transport has been observed, for example, in heterostructures with a single wide quantum well [121]. Double-channel mode has also been implemented in single QPCs [33–39, 122]. The necessary conditions for observing double-row electron transport are low electron concentration and weak confinement. Under such conditions e–e interaction can lead to a change in the ground state and to formation of Wigner crystal. It is known that a ‘string-zigzag’ structural transition occurs with a weakening of the confining potential or an increase in the electron concentration in a 1D Wigner crystal [15, 77, 123]. Experimentally this results in conductance plateau appearing at $2e^2/h$ to disappear so that the new ground state corresponds to the conductance $4e^2/h$. This phase transition is associated with the transition from single-row to double-row electron transport primarily occurring due to the formation of two rows of electrons caused by enhanced e–e interaction which lifts the degeneracy between states, thus leading to anti-crossing between bonding and antibonding states in the phase diagram [35, 37, 39]. The formation of double-row configuration was clearly demonstrated in experiments using transverse magnetic electron focusing [40]. It may be noted that quantum wires discussed here were, firstly, not suspended, and, secondly, were formed within the top-gated split gate devices and the transition from single-row to double-row electron transport discussed in references [33–39, 122] refers only to the 1st populated 1D subband.

In recent studies on the conductance of GaAs single trench-type QPCs both suspended [53, 54] and non-suspended [55], double- and triple-channel electron transport was experimentally observed. In this case, the conductance of individual channels is quantized and independently controlled by lateral in-plane gates, both at a small and a large number of populated 1D subbands. We discuss below the transport in multi-channel trench-defined QPCs.

For the trench-defined QPCs [53] the side gates were allowed to perform the conductance measurements as a function of two independent gate voltages and, thus, to obtain the phase diagram of 1D subband populations in separate channels. The conductance G was measured as a function of gate voltage sum $\Sigma V_G = V_{G1} + V_{G2}$ at different fixed values of gate voltage difference $\Delta V_G = V_{G1} - V_{G2}$ and the transconductance $\partial G / \partial \Sigma V_G$ as a function of ΣV_G and ΔV_G was plotted.

The observed picture can be explained by the formation of three non-interacting parallel channels, the conductance of which are added. Figure 11 shows schematically the conductance of three separate channels. The total conductance is shown in figure 11(c) and is in excellent agreement with the experimentally obtained dependence (see figure 11(d)):

$$G = 2 \frac{e^2}{h} \times (n_1 + n_2 + n_3), \quad (4)$$

where numbers n_1, n_2, n_3 are shown in figures 11(a), (b) and (d), while their sum $(n_1 + n_2 + n_3)$ is shown in figure 11(c).

The conductance of an individual channel is a pattern of alternating nearly parallel lines. This means that the conductance of an individual channel is controlled by some linear combination of gate voltages $(\alpha V_{G1} + \beta V_{G2})$, where α and

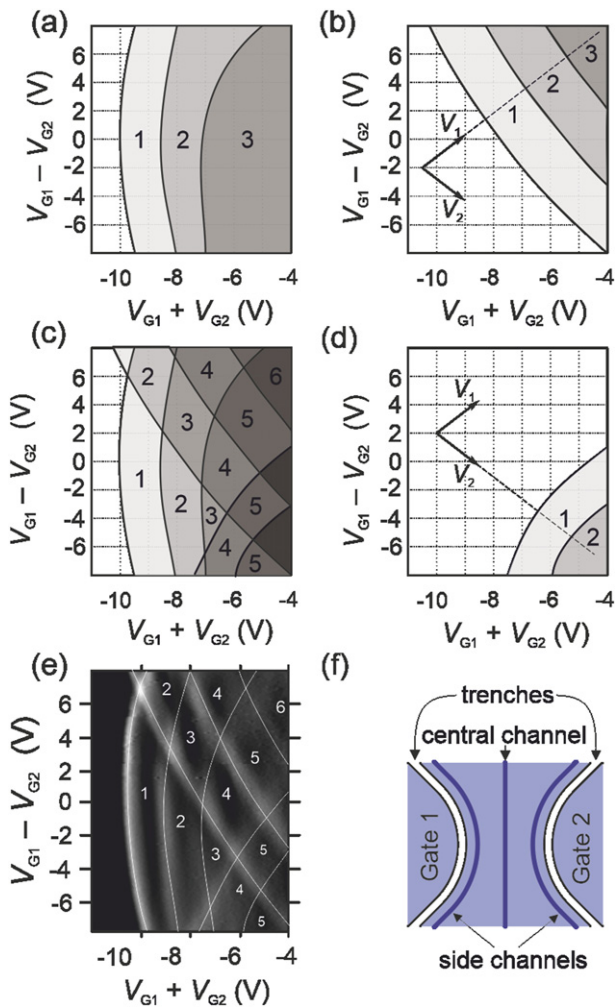


Figure 11. Conductance (represented as a gray-scale) of three conductive channels as a function of gate voltages. The conductance of (a) the central channel, (b), (d) two side channels, (c) their sum, and (e) the experimentally measured dependence. The numbers on the plot indicate the conductance in units of $2e^2/h$. (f) Schematic representation of three conductive channels in the QPC. Reprinted from [53], with the permission of AIP Publishing.

β are proportional to the gate-to-channel capacitance coefficients. Plateaus of conductance of one of the channels (see figure 11(a)) turn out to be elongated along the vertical axis and replace each other in the horizontal direction: conductance is determined mainly by the sum of voltages at the side gates ΣV_G and is almost independent of their difference ΔV_G . This behavior indicates that both side gates have almost the same effect on the conductivity of this channel, i.e. the corresponding mutual capacitances are approximately equal to each other. This fact allows us to consider this channel as located in the center.

The conductance of the other two side channels is governed by linear combinations $(\alpha V_{G1} + \beta V_{G2})$ and $(\beta V_{G1} + \alpha V_{G2})$, indicating a symmetry in the arrangement of the two channels relative to the middle of the QPC. It follows from the experiment that the ratio $\alpha/\beta \approx 5$. In other words, the side gate closest to the channel affects the conductance of the channel approximately 5 times stronger than the far one. Note that by

changing the gate voltages in this combination, it is possible to independently control the conductance of individual channels using two gates.

Knowing the typical 1D subband energy spacing $\Delta E \approx 12$ meV for suspended QPCs [53, 54], one can estimate the width of the channel w . If we assume that the confinement potential near the parabolic bottom, then the energy on the edge of the channel is determined by the expression:

$$E = m^* \omega^2 (w/2)^2 / 2, \quad (5)$$

where $\omega = \Delta E/\hbar$, m^* is an effective electron mass in GaAs. An estimation, for example, for the second subband, for which $E = 3\hbar\omega/2$, gives $w \approx 30$ nm, which is comparable to the electron Fermi wavelength in a 2DEG, but about 30 times less than the lithographic width W of the studied QPC. Thus, the channels can be considered as narrow. Since the QPC length ($L \approx 1 \mu\text{m}$) is sufficiently larger than the conducting channel width, the ‘channel-gate’ capacitance can be estimated using the model of a two-wire line. In this model, the ‘channel-gate’ capacitance is $C \propto 1/\ln(X/w)$, where X is the channel-gate distance. Therefore, the ratio of capacitance coefficients between a side gate and two channels equals

$$\frac{C_1}{C_2} = \frac{\alpha}{\beta} = \frac{\ln[(W/2 + \Delta X)/w]}{\ln[(W/2 - \Delta X)/w]} \approx 5, \quad (6)$$

where $W \approx 1.2 \mu\text{m}$ is the effective distance between gates, ΔX is the channel spatial displacement relative to the QPC middle line. The estimation gives $\Delta X \approx 530$ nm. Taking into account that the lithographic width of the QPC minus depletion regions width is about 600 nm, it can be concluded that the conducting channels are formed near the lithographic edges [53, 55].

The described experimental multichannel picture remains almost unchanged during several sample cooling cycles. Since each cooling cycle changes the realization of the random potential of impurities, the observed behavior is difficult to explain by impurity [124].

The possible reason for the appearance of several conducting channels inside a single QPC is the spontaneous correlated lateral redistribution of electrons in GaAs/AlGaAs heterostructures, which decreases the electrostatic energy. Such redistribution can be associated with the peculiarities of heterostructures used for device fabrication. Multi-channel QPCs were fabricated on the basis of heterostructures (see figure 12(a)) containing 13 nm-thick quantum well with high-mobility 2DEG, surrounded by AlAs/GaAs superlattice layers containing δ -layers of a Si donor impurities at a distance of 30 nm on both sides of the quantum well and low-mobility X-valley electrons that do not participate in conduction, but screen fluctuations of the impurity potential, leading to an increase in the mobility in the 2DEG. The concept of using low-mobility X-valley electrons in GaAs/AlGaAs heterostructures is described in [125] and is now widely used to create a high-mobility 2DEG. In structures in which there are no such electrons, etching of lithographic trenches and capturing of electrons to surface states at lithographic edges lead to edge depletion of the 2DEG and the formation of a single channel near the middle of the constriction (see figure 12(d)).

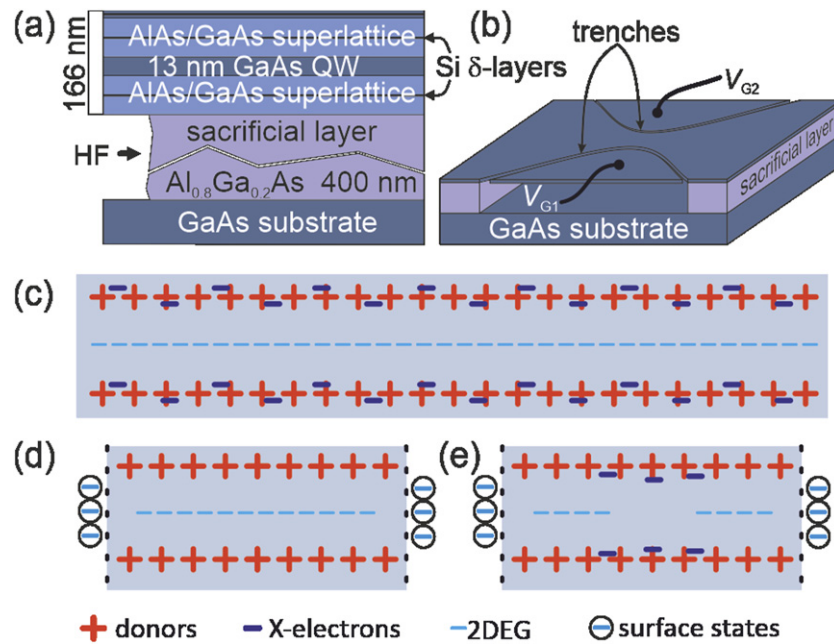


Figure 12. (a) Heterostructure with a 2DEG and a sacrificial layer. (b) Schematic representation of suspended QPC. Schematic image of the charge distribution in the heterostructure: (c) without lithographic edges, (d) in the presence of lithographic edges in the absence of X-valley electrons, and (e) in the presence of lithographic edges and X-valley electrons. Reproduced from [54], with permission from Springer Nature.

While in structures containing X-valley electrons, electrostatics is significantly different. Such X-electrons repelling from the trench surface electrons are collected near the middle of the microconstriction (see figure 12(e)), forming an additional repulsive potential (barrier) for electrons in the 2DEG. Such correlated redistribution can decrease the electrostatic energy. This explanation is consistent with the above described experimental dependences of conductance on voltages at the side gates. Similar ignominious distribution of electrons along the plane of strongly coupled electron–hole graphene bilayers having a form of charge density waves was theoretically predicted [126]. The effect of redistribution can be enhanced upon suspension due to the enhancement of the Coulomb interaction.

It should be noted that the above-mentioned physical mechanism associated with spontaneous correlated redistribution of charges in a heterostructure are still qualitative. The physical nature of multichannel electron transport in single GaAs QPCs requires further comprehensive experimental and theoretical research.

3. Ballistic and adiabatic electron transport in suspended nanostructures

3.1. Dynamical chaos in electron billiards

As is known, molecular beam epitaxy allows one to obtain a high quality 2DEG with the electron mean free path l exceeding more than $10 \mu\text{m}$. On the other hand, electron lithography followed by plasma-chemical etching makes it possible to create artificial scatterers about 100 nm in size within a high-mobility 2DEG. The motion of electrons in such

systems resembles the motion of balls on a billiard table, and by analogy these systems are called electron billiards.

There are several varieties of solid-state electron billiards implementations. The most thoroughly studied among them are periodic lattices of scattering discs, which are called antidots. Such structures with periodic scatterers can be considered as a models of artificial crystals. Antidot lattices were first experimentally investigated in ordinary non-suspended structures [127]. Initially, such structures were created to study purely quantum phenomena in a magnetic field, such as the energy spectrum expected to have the form of a ‘Hofstadter butterfly’ [128]. Magnetoresistance oscillations caused by this effect were indeed observed later [129, 130]. However, the first experiments [127, 131–133] showed that such systems most clearly manifest purely classical effects caused by the chaotic dynamics of electrons in the periodic potential of artificial scatterers. It is shown that these systems belong to the type of the so-called Sinai billiards [134], where chaos is not caused by the intrinsic scatterers disorder, but is a property of the motion itself and for this reason is called dynamical chaos. Experimentally, chaotic dynamics in periodic lattices of antidots manifests itself in high-amplitude oscillations of magnetoresistance. The characteristic dependence of the resistance on the magnetic field is shown in figure 13. In weak magnetic fields one can see oscillations with the main peak at magnetic field $B \approx 0.2 \text{ T}$ corresponding to the commensurability of the diameter of the electron cyclotron orbit with the lattice period: $2R_c = d$. Such oscillations are called ‘commensurability oscillations’. The oscillations shown in the figure in higher magnetic fields (above 0.3 T) are the well-known Shubnikov–de Haas oscillations.

Numerical simulation of the classical motion of electrons in antidot lattices in various magnetic fields made it possible

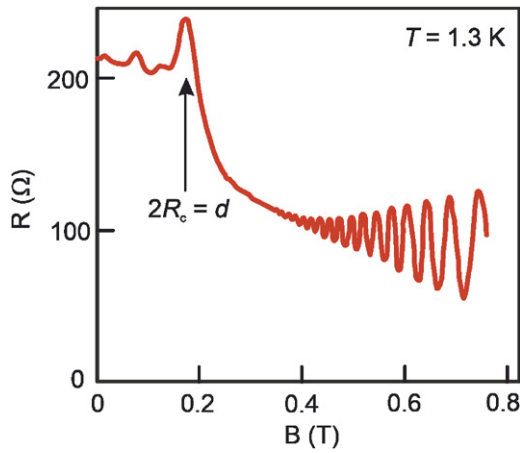


Figure 13. Magnetoresistance of the square antidots lattice, $d = 1.3 \mu\text{m}$. Reproduced from [135], with permission from Springer Nature.

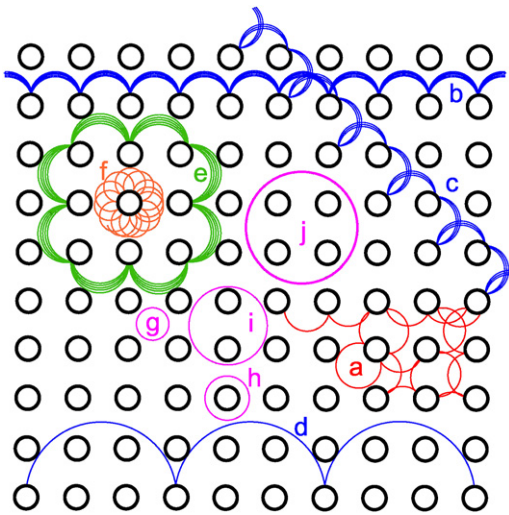


Figure 14. Typical electron trajectories in a square antidot lattice: (a) diffusive trajectory; (b)–(d) runaway trajectories; (e) localized skipping trajectory; (f) rosette trajectory; (g)–(j) pinned orbits. Reprinted from [136], Copyright (2017), with permission from Elsevier.

to identify specific trajectories responsible for the observed commensurability oscillations (see figure 14). The simulations show that, in addition to chaotic trajectories, regular electron trajectories also exist in antidot lattices. These regular trajectories are dynamically stable and occupy a finite phase space volume. Such a picture is typical for systems with dynamical chaos.

One of the explanations for the main commensurability peak, observed at $2R_c \approx d$, is associated with the appearance of ‘runaway’ trajectories ‘skipping’ along the rows of the antidots lattice (see figure 14, trajectory *b*) [137]. The behavior of these trajectories is illustrated in figure 15 demonstrating the section of the Poincaré map $(\varphi, \psi) \rightarrow (\varphi', \psi')$ in terms of angles φ and ψ , shown in the inset to the figure. The color indicates the number N of consecutive jumps occurring without failure [73]. Large white area corresponds to N exceeding 100. Moving away from this area gradually leads to destruction of stable regular motion. The trajectories that make at least

5–10 consecutive collisions (with the length comparable to the mean free path l) can be referred to as runaway trajectories. Such trajectories occupy significant volume of the phase space providing a noticeable contribution to the magnetoresistance. In addition, the figure demonstrates that the boundary of the stability region of runaway trajectories has a fractal structure.

Another explanation for the main commensurability peak is associated with pinned electron orbits surrounding one (see figure 14, trajectory *h*) or several (see figure 14, trajectories *i*, *j*) antidots depending on the magnetic field [138]. Apparently, this model is well applicable in dense lattices of antidots. However, in the typical case, when the lattices of antidots are rarefied, it was shown that it is the model of runaway trajectories that makes it possible to explain the entire spectrum of experimentally observed phenomena [139–142].

Dynamical chaos and the associated commensurability effects manifest themselves not only in the described oscillations of the magnetoresistance, but also in the oscillations of the thermopower of the same nature, also found experimentally [143]. Furthermore, an anomalous growth of the nonlocal resistance was found in magnetic fields corresponding to the commensurability conditions [139].

It should be noted that, in addition to the ballistic effects, the periodic structure of artificial scatterers in the 2DEG leads to the peculiarities of quantum interference phenomena, including mesoscopic fluctuations of conductance [144–147] and thermopower [148], weak localization [149] and Aharonov–Bohm effect [144, 145, 150, 151] as well as the metal–insulator transition [152, 153]. These effects arise at low temperatures, when the phase coherence length is greater or comparable to the characteristic dimensions of the antidot lattice. GaAs triangular lattices of antidots are also interesting because they can be used to create ‘artificial graphene’. Similar to graphene, two-dimensional electrons have linear dispersion in the potential having the symmetry of a honeycomb structure formed by such antidot lattice [154, 155].

In lattices of antidots, electron mean free path l is greater than the distance between adjacent scatterers, but less than the size of the entire lattice. When the sample size is reduced to a value less than l , the description of the transport properties in terms of the conductivity tensor, which gives a local relation between the electric field and the current, becomes inapplicable. Appropriate description of the transport properties of such systems can be obtained by the Landauer–Büttiker formalism [156]. An example of such a system studied experimentally is the ‘star’-like Sinai billiard, which is formed by six antidots placed in vertices of regular hexagon with small distances between them (see figure 16) [157]. Figure 16 demonstrates the magnetoresistance of such a billiard measured at a temperature of $T = 4.2 \text{ K}$. It is well known that in a 2DEG formed in GaAs/AlGaAs heterojunction, the classical magnetoresistance in weak magnetic fields is absent. However, figure 16 clearly shows magnetoresistance oscillations, and, moreover, they are sign-changing. The characteristic stable ballistic trajectories responsible for these anomalies arise at certain magnetic fields corresponding to the required curvature of the trajectories.

Another type of experimentally studied solid-state Sinai billiards is the ‘caterpillar’-like billiard. When studying the

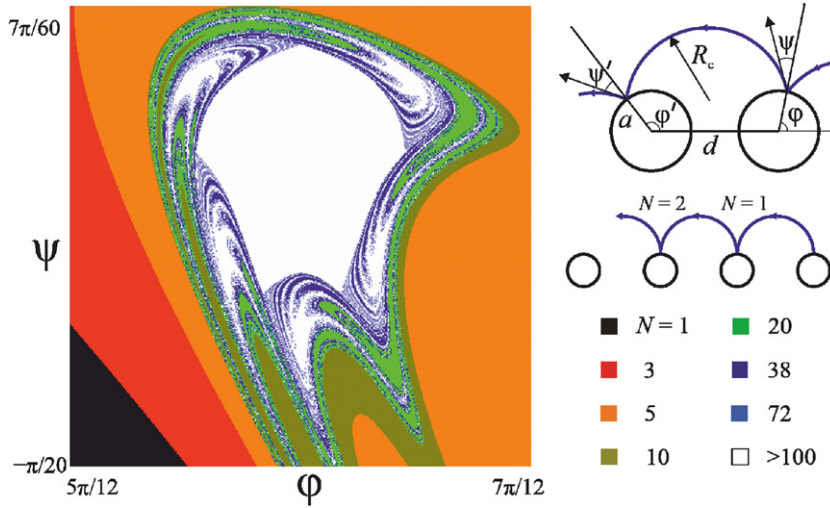


Figure 15. Calculated regions of the stability of outgoing trajectories ‘skipping’ along an antidot array in angular coordinates, where φ characterizes the electron angular position during the collision with an antidot, and ψ is the angle of electron reflection from an antidot. Color shows the number N of sequential jumps occurring without failure. Reproduced from [73], with permission from Springer Nature.

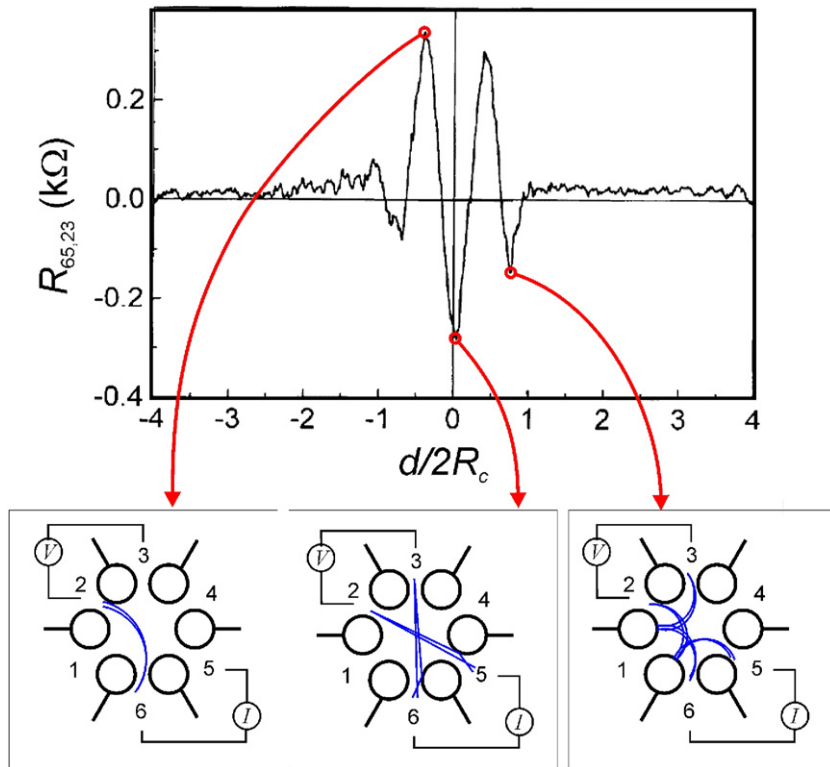


Figure 16. Magnetoresistance of ‘star’-like billiard and trajectories responsible for anomalous peaks. Reprinted from [2], Copyright (2017), with permission from Elsevier.

magnetoresistance and magnetic field dependences of the longitudinal and transverse (Nernst–Ettingshausen effect) components of the thermopower tensor in such a billiard, a generalization of the Landauer–Büttiker formalism to thermoelectric phenomena was given [158].

To be noted all these phenomena discussed above were studied in non-suspended electron systems, i.e. systems located in a semiconductor bulk. Particular interest in the study of suspended electron billiards arises due to their

features, such as weakened heat removal into a substrate and modified phonon spectrum inherent to suspended nanostructures. These features will be discussed in the following subsections. As is known in the presence of an electric field and the temperature gradient conductors are characterized by four kinetic coefficients, three of which are independent taking into account Onsager relations. These include conductance (resistance), discussed in subsection 3.2, thermopower and thermoconductance, discussed in subsection 3.3.

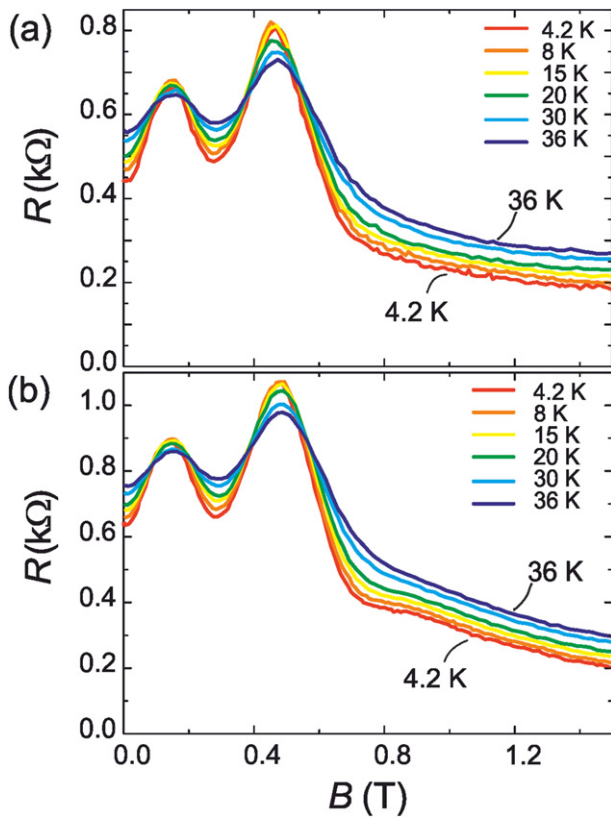


Figure 17. Temperature dependence of the magnetoresistance (a) non-suspended antidots lattice; (b) suspended antidots lattice. Reproduced from [73], with permission from Springer Nature.

3.2. Magnetoresistance of suspended electron billiards

When low-dimensional electron systems are suspended, an additional bottom surface appears. There are plenty of electron states at this surface causing the Fermi level pinning in the middle of the bandgap and leading to additional depletion. Suspension of 2DEG poses two major challenges, one is maintaining the carrier concentration within the 2DEG after suspension close to its non-suspended value, and the other is degradation in electron mobility after suspension. This is often discussed whether the characteristics of 2DEG could be retained after suspension. Experimental results show that it is possible to create suspended 2DEGs with a reasonable density of order of $5 \times 10^{11} \text{ cm}^{-2}$. High electron mobility is required to experimentally study ballistic effects in electron billiards. Suspension can be expected to significantly degrade mobility, because the bottom surface, being exposed after selective etching, is less smooth and more enriched with defects contributing to electron scattering. It is worth mentioning that the suspension of graphene leads, on the contrary, to an increase in carrier mobility due to distancing from the substrate which is abundant in scatterers [159]. This is in line with the fact that the charge carriers in graphene differ significantly from those in semiconductor nanostructures. The study of graphene-like structures is beyond the scope of this article. One can read more about these differences and about the studies of a 2DEG in 3D periodical systems based on graphene in, for example [160].

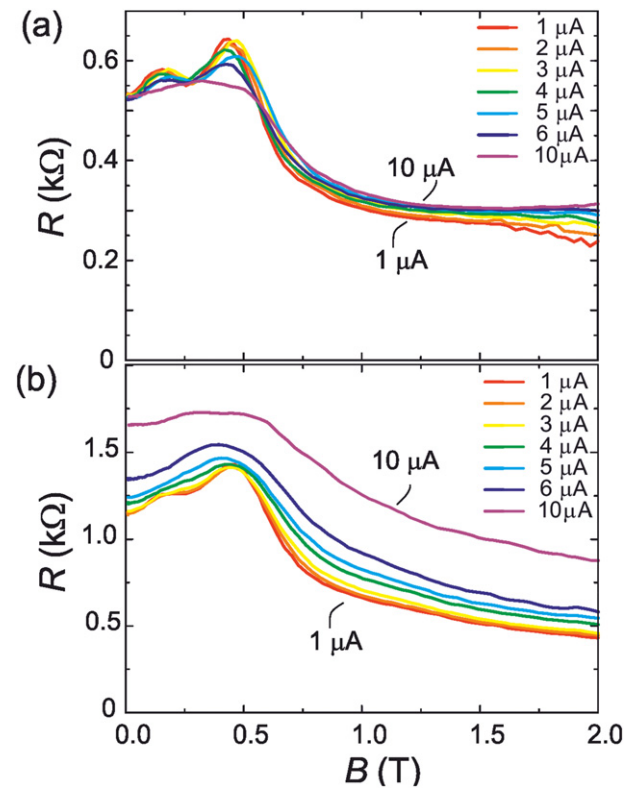


Figure 18. Dependence of the magnetoresistance (a) non-suspended antidots lattice; (b) suspended antidote lattice on the amplitude of dc current. Reproduced from [73], with permission from Springer Nature.

Additionally, a question arises whether electron systems can have high enough mobility in suspended nanostructures to study the ballistic effects. The answer largely depends on the thickness of the nanostructures, which determines the distance between the bottom surface and the 2DEG. For 100 nm membranes, the reported mobility is only $1.4\text{--}1.6 \times 10^4 \text{ cm}^2 \text{ V}^{-1} \text{ s}^{-1}$, however, even in this case geometric resonances were observed in magnetoresistance [8]. In suspended structures with slightly increased thickness (up to 130 nm), the measured mobility is much higher $5.75 \times 10^4 \text{ cm}^2 \text{ V}^{-1} \text{ s}^{-1}$ [161]. Later studies have shown that the mobility of a 2DEG contained in suspended structures can be significantly improved and increased up to $9 \times 10^5 \text{ cm}^2 \text{ V}^{-1} \text{ s}^{-1}$ at 160 nm thickness by placing the remote δ -doping layers in short-period AlAs/GaAs superlattices [125].

With these structures containing a high-quality 2DEG, it becomes possible to study ballistic transport effects in suspended electron billiards and, particularly, in suspended antidot lattices. Commensurability oscillations in such lattices were observed and shown to have ballistic origin by checking that the magnetoresistance curves remain unchanged when the temperature is varied below 4.2 K [162]. In contrast to other mesoscopic structures, such as, for example, QPCs, the first magnetoresistance measurements revealed no features of suspended antidot lattices in comparison to their non-suspended counterparts. Moreover, when temperature increases up to 50 K, the commensurability oscillations are almost identically

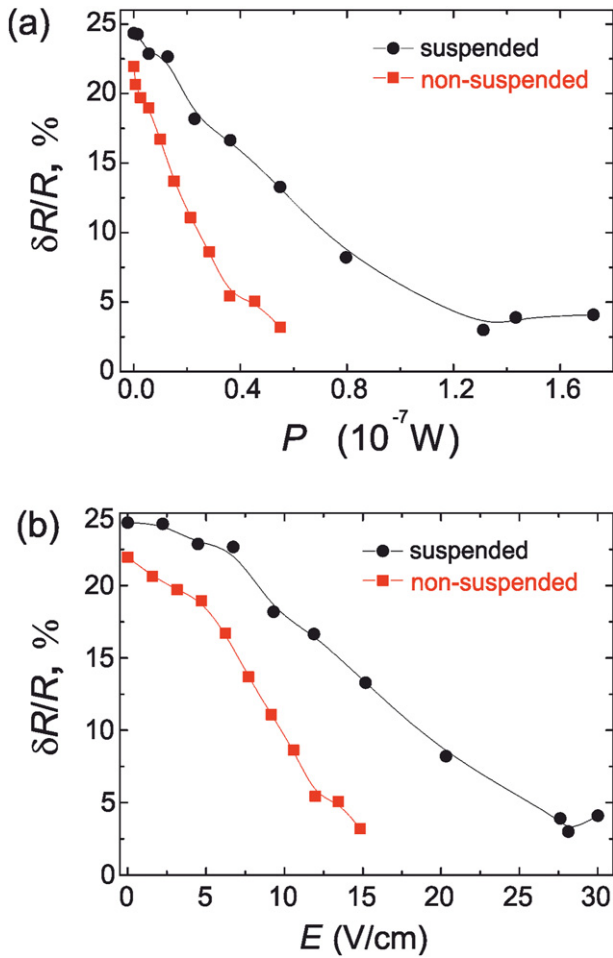


Figure 19. Dependence of the relative amplitude of the main peak of commensurate oscillations on (a) the power released in the sample and (b) the applied electric field for suspended and non-suspended samples. Reproduced from [73], with permission from Springer Nature.

suppressed, regardless of whether the samples are suspended or not [73] (see figure 17). This similarity can be explained by the fact that low- B magnetoresistance is determined by classical geometrical effects, and the suppression is caused by the temperature-induced Fermi-level spreading, which is identical in suspended and non-suspended samples.

However, further studies have shown that the suspended antidot lattices demonstrate prominent features in the nonlinear regime, when the commensurability oscillations are suppressed by passing a high dc current through the system, in addition to the small ac current used for the measurements [73] (see figure 18). As is known, the current may lead to such suppression via two main physical mechanisms. The first is the heating-induced dispersion of the Fermi velocity. Taking into account the weak thermal anchoring of the suspended nanostructures to the substrate, the heating current should be more suppressive in suspended than in non-suspended samples. The second suppression mechanism is the destruction of the stable runaway trajectories due to the drift of the circular electron orbits in crossed electric and magnetic fields [135]. In this case, an electric field should destroy the commensurability oscillations identically, regardless of whether the

samples are suspended or not. Surprisingly, experimental findings show that the commensurability oscillations are more robust in suspended rather than in non-suspended samples when a dc current is passed through the system (see figure 19). This observation contradicts both of the mentioned physical mechanisms and shows that some additional suppressive effects may play a significant role. These effects may be related to the presence of non-equilibrium charge carriers in the antidot lattice. In the case of suspended systems, shorter thermalization lengths can be expected because of stronger interaction between electrons. In this case, we can try to describe the system by a quasi-Fermi level gradually changing in space when moving from source to drain, and this description should be more correct for suspended rather than for non-suspended systems. In other words, when the dc current passing through the sample, suspended nanostructures are in more equilibrium state than their non-suspended counterparts. Further investigation is needed to confirm that such equilibration effects can explain the unusual robustness of the commensurability oscillations in suspended antidot lattices.

3.3. Thermal conductance and thermopower of suspended nanostructures

Generally speaking, thermal conductance and thermopower are determined by electron subsystem, phonon subsystem and their interaction. One of the important features of suspended nanostructures is the reduced phonon dimensionality. Indeed, in heterostructures detached from the substrate, phonons become quasi-two-dimensional at low temperatures. Let a be the thickness of the membrane, then the size quantization condition corresponds to wavelength $\lambda = 2a$ (half of the wavelength fits in the membrane) and temperature $T \sim \frac{\hbar\omega}{k_B} = \frac{2\pi\hbar s}{k_B\lambda} = \frac{\pi\hbar s}{k_B a}$, where s is the phonon velocity. For example, in GaAs/AlGaAs heterostructures, the phonon velocity varies within $3\text{--}6 \times 10^3 \text{ m s}^{-1}$ depending on their type, aluminum content and crystallographic orientation, which, in turn, with a membrane thickness of about 100 nm, corresponds to temperatures of 0.6–1.2 K. Thus, phonon quantization in the direction perpendicular to the membrane plane seems to be quite achievable from the experimental point of view. Similarly, by reducing the lateral dimensions of the suspended membranes, one can achieve quantization in the membrane plane. In particular, narrow suspended wires can be considered as 1D phonon waveguides.

One of the striking demonstrations of the phonon quantization is the observation of the quantum of thermal conductance. To explain the quantum limit of thermal conductivity, let us consider a single-mode phonon waveguide connecting two reservoirs with hot and cold phonons. At unity transmission coefficient between the reservoirs, the difference between the energy fluxes carried by hot and cold phonons in such a waveguide is

$$\Delta\Phi = \int_0^\infty \hbar\omega(k) \cdot (\eta_{\text{hot}}(\omega(k)) - \eta_{\text{cold}}(\omega(k))) \cdot v_g \frac{dk}{2\pi}, \quad (7)$$

where $v_g = \partial\omega/\partial k$ is the group velocity, and

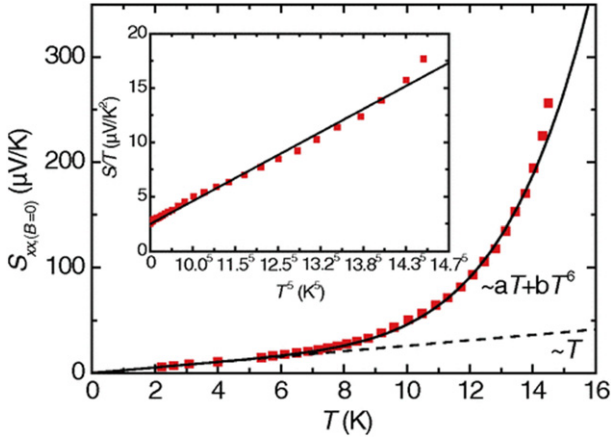


Figure 20. Temperature dependence of zero-field thermopower. Reprinted (figure) with permission from [164], Copyright (2012) by the American Physical Society.

$$\eta = \frac{1}{\exp\left(\frac{\hbar\omega}{k_B T}\right) - 1}$$

is the Bose–Einstein occupation factor for hot and cold phonons. Conversion of equation (7) to an integral over frequency in the linear approximation with respect to the temperature difference ΔT gives

$$\Delta\Phi = \int_{\omega_m}^{\infty} \hbar\omega \cdot \frac{\partial\eta}{\partial T} \Delta T \cdot \frac{\partial\omega}{\partial k} \frac{\partial k}{\partial\omega} \frac{d\omega}{2\pi}, \quad (8)$$

where ω_m is the cutoff frequency of the m th mode. As in the case of ballistic electrons, the group velocity cancels out with the density of states. At low temperatures, only the modes with zero cutoff frequency are excited ($\omega_m = 0$). For each of these modes, the thermal conductivity is

$$G_{\text{th}} = \frac{\Delta\Phi}{\Delta T} = \int_0^{\infty} \frac{\hbar^2 \omega^2}{k_B T^2} \cdot \frac{\exp\left(\frac{\hbar\omega}{k_B T}\right)}{\left(\exp\left(\frac{\hbar\omega}{k_B T}\right) - 1\right)^2} \frac{d\omega}{2\pi}. \quad (9)$$

From this expression, we obtain the value for the thermal conductance quantum

$$G_{\text{th}} = g_0 = \frac{\pi^2 k_B^2 T}{3h}.$$

The value of this quantum $g_0 = (9.5 \times 10^{-13} \text{ W/K}^2) \cdot T$ is small and its observation requires precise measurement equipment and special nanodevices. Such devices were created on the basis of suspended GaAs nanostructures of low heat capacity, containing thermal conductors with separate thermal transducers [7]. On their basis, supersensitive devices have been developed that have prospects for use in calorimetry and bolometry. Direct thermal conductance measurements were performed in a similar structure representing a phonon cavity suspended on four phonon waveguides fabricated from a 60 nm-thick silicon nitride membrane. These measurements made it possible to experimentally measure the value of the thermal conductance quantum in a 1D ballistic phonon channel

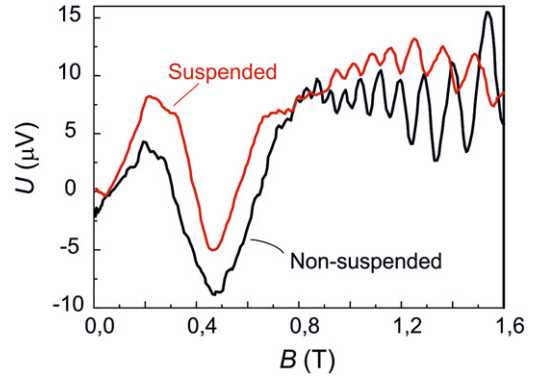


Figure 21. Commensurability oscillations of thermopower of suspended and non-suspended antidot lattices. Reproduced from [165]. © The Author(s). Published by IOP Publishing Ltd. CC BY 4.0.

[61]. The measured value $16g_0$ corresponds to four waveguides, in each of which four modes with zero cutoff frequency are excited.

In contrast to thermal conductance of the considered electrically insulating systems, the thermopower is determined by the electron subsystem and its interaction with the phonon one. There are two contributions to thermopower. The first of them is the diffusive thermopower associated with the dependence of conductivity on the Fermi energy. The second contribution is so-called phonon drag thermopower which is associated with electron–phonon interaction [163]. Temperature gradient induces a phonon flow. The phonons, scattering on electrons, partly transfer quasi-momentum to them, leading to an electron flow. In turn, this flow of electrons from hot to cold sample edges creates the phonon drag thermopower. In ordinary structures, the study of electron–phonon interaction is limited by the cases of interaction of three-dimensional phonons with either three-dimensional or low-dimensional electrons. In the case of suspended nanostructures, dimensionalities of both electron and phonon subsystems are reduced. In addition, in such structures, weakened heat removal to the substrate makes it possible to induce a large temperature gradient that facilitate the measurement of a small thermopower signal. This was realized, for example, in a suspended 320 nm-thick GaAs/AlGaAs Hall bar [164]. The measurements demonstrated that the phonon drag thermopower is strongly suppressed up to temperatures of the order of 7 K and has a power-law dependence different from that in the case of a bulk material (see figure 20). These features are presumably associated with a change in the electron–phonon interaction and the small size of the sample. However, it should be noted that their direct connection with the dimensional quantization of phonons is not obvious, since these features are observed at temperatures an order of magnitude higher than those corresponding to quantization.

In addition to nonstructured suspended membranes, thermopower measurements were also carried out in suspended antidot lattices. The magnetic field dependence of the ballistic thermopower [165] was investigated, which demonstrated commensurability oscillations, as well as the Shubnikov–de Haas oscillations following them (see figure 21). In contrast to

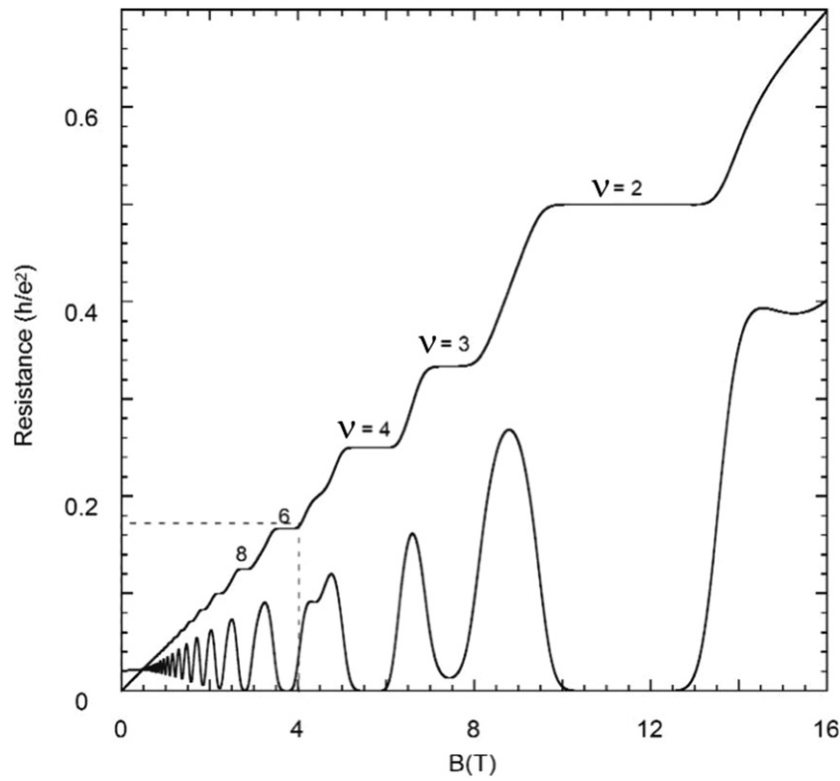


Figure 22. A conventional picture of the QHE: vanishing longitudinal and quantized transverse (Hall) resistance of a 2DEG as a function of magnetic field. Reproduced from [176]. Image stated to be in the public domain

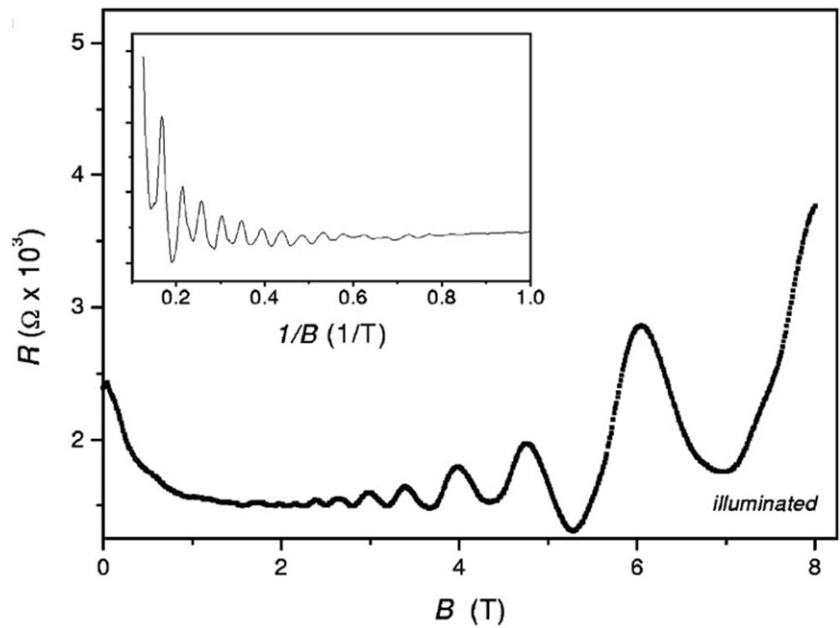


Figure 23. Longitudinal resistance of suspended Hall bar as a function of magnetic field. Vanishings are absent. The inset gives a $(1/B)$ plot demonstrating a single period of Shubnikov–de Haas oscillations. Reprinted (figure) with permission from [8], Copyright (2000) by the American Physical Society.

the magnetoresistance peaks, the thermopower ballistic resonances are N-shaped. This is easy to understand, given that the 2DEG is degenerate.

As is known, the thermopower of metals and degenerate conductors is small (of the order of $k_B T/E_F$), which can

be explained in terms of ‘electrons’ (particles with energies slightly above the Fermi surface) and ‘holes’ (particles with energies slightly below the Fermi surface). In the presence of temperature gradient, both of them move from the hot end of the sample to the cold one, so that the total transferred current

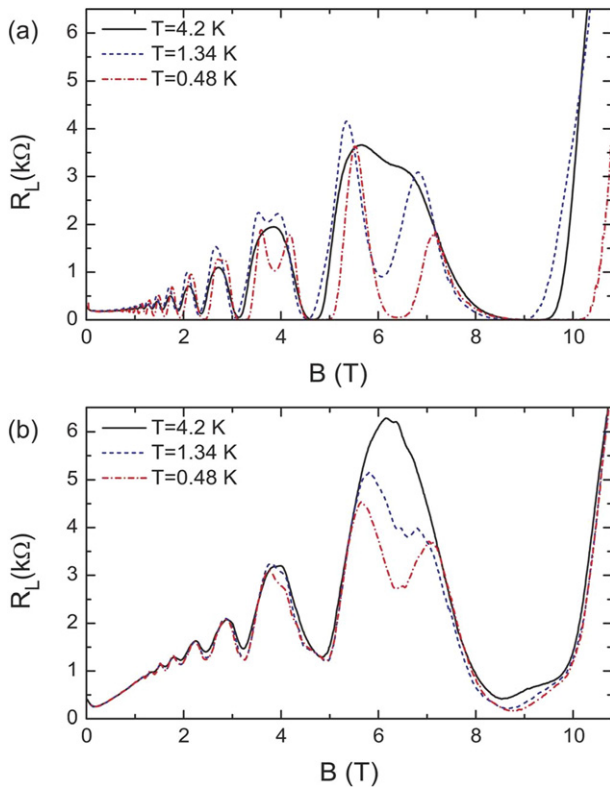


Figure 24. Longitudinal resistance of Hall bar as a function of magnetic field (a) before and (b) after suspension. Vanishings are absent in suspended samples. Reprinted from [79], with the permission of AIP Publishing.

is close to zero. Its non-zero magnitude is determined by the small difference between the ‘electron’ and ‘hole’ conductivities arising due to the small difference in their energies (this is why the thermoelectric current is proportional to the derivative of the conductivity with respect to energy).

The situation changes dramatically in the presence of geometric resonances typical for the systems with dynamical chaos. Indeed, the cyclotron radius of ‘electrons’ is slightly larger than that of ‘holes’, and both radii decrease with increasing magnetic field. The magnetic-field resonance that occurs at a certain cyclotron radius has a finite width and leads to a sharp increase in mobility. With an increase in magnetic field, ‘holes’ are the first to enter the resonance, their mobility increases sharply, and the thermopower becomes positive. With a further increase in the magnetic field, both types of quasiparticles are in resonance, their mobilities are almost equal, and the thermopower drops to zero. Then the ‘holes’ go out of the resonance; therefore, the thermopower is determined by ‘electrons’ and becomes negative. Finally, both of them go out of resonance, and the thermopower returns to a value close to zero.

Note that the discussed feature of the thermopower is observed against almost a zero background. Due to this, the thermopower measurement is a technique more sensitive than the conventional magnetoresistance. Nevertheless, the magnetic field dependence of the thermopower measured in suspended samples did not reveal additional features caused by the change in the phonon spectrum. Presumably, such features

could be revealed in the phonon drag thermopower, but the design of the studied samples made it possible to measure only the diffusion thermopower without the contribution of the phonon drag thermopower.

Moreover, the electron temperature distribution was shown to remain the same before and after suspension. This is caused by two reasons. First, the electron–electron interaction time was much shorter than the electron–phonon interaction time, and, thus, the thermopower magnitude was determined by the gradient of electron rather than phonon temperature. Second, the electron–phonon interaction time was much longer than the Thouless time, that is, the time that an electron spends in the sample. Thus, the physical picture of thermoelectric phenomena in suspended nanostructures is far from being complete. The most interesting effects related to the interaction between low-dimensional phonons and electrons may be discovered with specially designed samples and corresponding experiments.

3.4. Quantum Hall effect in suspended 2DEG

Despite more than 40 years of intensive research, some transport phenomena associated with the quantum Hall effect (QHE) [166] still attract considerable attention. They include, for example, 3D QHE [167], hysteresis phenomena [168, 169] and the QHE in fundamentally new systems such as graphene [170, 171] or topological insulators [172, 173]. Unusual phenomena in the QHE regime are also observed in suspended semiconductor structures with a 2DEG. To date, integer QHE is studied in such structures, while fractional QHE [174] has not been observed in them. As is known, the integer QHE manifests itself in the vanishing of the longitudinal resistance R_L and the quantization of the transverse resistance $R_H = h/(e^2\nu)$ at integer filling factors ν (see figure 22). One of the simplest and most illustrative models for explaining this effect is the model of edge channels [156, 175]. According to this model, in strong magnetic fields near integer filling factors, when the Fermi level lies between the Landau levels, a spatial separation arises between the edge channels and the bulk states at the Fermi level. When this spatial separation becomes greater than the magnetic length, electron tunneling from edge to bulk states ceases, which leads to suppression of backscattering and, as a consequence, to vanishing of R_L . Thus, in order to be convinced of the observation of a pronounced QHE regime, it is necessary to demonstrate both the quantization of R_H and the corresponding vanishing of R_L .

The first experiments in strong magnetic fields performed on suspended nanostructures [8, 161] demonstrated magnetoresistance oscillations, however without any pronounced QHE regime: magnetic field dependence of R_L was presented, while the magnetic field dependence of R_H was not shown (see figure 23). Moreover, in quantizing magnetic fields, the expected vanishings at integer filling factors were absent. This non-zero R_L is not associated with parallel conductivity, since $1/B$ spectrum of the oscillations shows only a single period (see inset to the figure 23).

With the advancement in fabrication technique, high mobility suspended nanostructures have been produced [177]

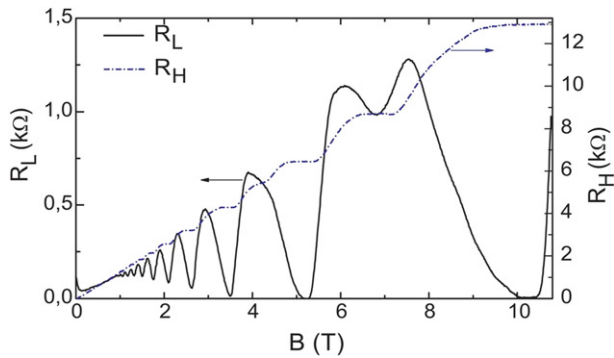


Figure 25. Vanishing longitudinal and quantized Hall resistance of suspended 2DEG in samples where boundary between suspended and non-suspended areas is moved outside the Hall bar. Measurements performed at 4.2 K. Reprinted from [79], with the permission of AIP Publishing.

where the Hall magnetoresistance quantization plateaus were reported in a suspended 320 nm-thick Hall bar [177]. These quantization plateaus corresponded to the minima in the R_L , however, R_L vanishings was not observed even after mobility improvement. Moreover, it was shown later that, significant decrease in temperature down to sub-kelvin values also does not lead to R_L vanishing (see figure 24) [79]. The suspended Hall bars inevitably contain a boundary between suspended and non-suspended areas. At such a boundary, a potential barrier can arise, leading to backscattering of edge current channels [79], which, in turn, leads to the absence of vanishings in R_L . To test this hypothesis, samples were made in which the discussed boundary was moved outside the Hall bar, that is, the Hall bar was suspended together with the potential contacts. In such samples it was indeed possible to observe a clearly pronounced QHE regime with vanishings of R_L even at temperature 4.2 K (see figure 25). In addition to the AlGaAs/GaAs samples, suspended structures with a high mobility 2DEG in InGaAs/InAlAs heterostructures were created [178]. In these structures, vanishings of the longitudinal magnetoresistance and the corresponding quantization plateaus in the Hall resistance at temperatures below 1.6 K were found [179].

Investigation of electron transport in quantizing magnetic fields also included the study of nonlinear effects, namely, the breakdown of QHE by a direct current [180, 181], in a suspended 2DEG based on GaAs/AlGaAs [79] and InGaAs/InAlAs [179] heterostructures. The measurements were carried out in fixed magnetic fields corresponding to the integer filling factors, when the longitudinal resistance is zero. In addition to a weak alternating current used to measure the resistance, a direct current was also passed through the current contacts. The dependence of the longitudinal resistance on the value of the direct current was measured. When the current reached a critical value, the breakdown of the QHE regime happened, leading to a sharp increase in the resistance. The measurements were carried out on the same samples before and after their suspension. These comparative experiments showed that the breakdown of QHE in suspended Hall bars is achieved at critical currents several times lower than in non-suspended ones (see figure 26). According to the existing

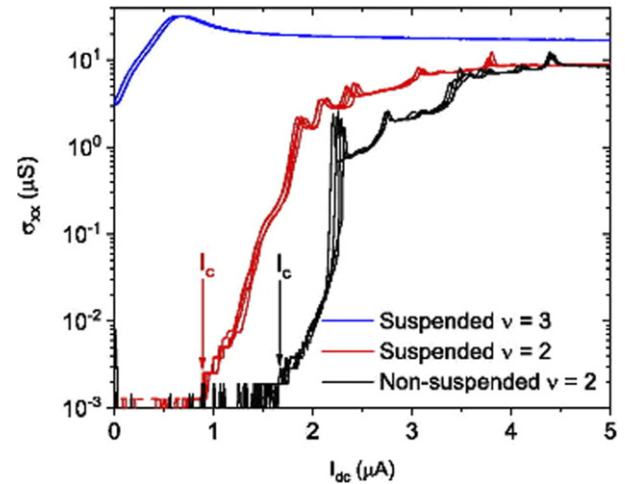


Figure 26. Breakdown of the QHE in non-suspended and suspended Hall bars. Reprinted from [179], with the permission of AIP Publishing.

models developed for ordinary, non-suspended structures, the critical current of the breakdown depends on the sample geometry (particularly, on the Hall bar width) and electrostatic interaction [182]. It can be assumed that suspension changes the actual width of the Hall bars due to the depletion. However, the critical current has been shown to depend logarithmically on the Hall bar width [183], so it is unlikely that small variations in the Hall bar width cause this difference. Most likely, the critical current decrease after suspension is related to the peculiarities of the heat balance in suspended structures. Due to the lack of heat removal directly through the substrate, overheating of the sample, and thus the QHE breakdown, are achieved at lower heating currents, which is consistent with the bootstrap-type electron heating model [184]. Furthermore, it was found that beyond the critical current, background impurity scattering in the suspended 2D channel regions leads to stochastic, resonant-like features appearing in the conductivity before the onset of the Ohmic regime [179].

It is interesting to note that QHE was observed not only in planar suspended heterostructures with 2DEG, but also in rolled semiconductor heterostructures with a cylindrical geometry. Creation of such structures is made possible by the use of built-in strain in lattice-mismatched heterostructures, which leads to the rolling of under-etched films [185]. The first experiments carried out on such samples did not demonstrate vanishings of the longitudinal magnetoresistance. Well-developed quantized Hall plateaus were observed, but not in the whole range of magnetic field. In magnetic fields higher than 10 T, strong deviations from the common quantum Hall characteristics develop. Instead of the plateaus, pronounced maxima appear and the Hall voltage starts to decrease with increasing field [186] (see figure 27). Subsequently, the use of high-quality samples based on a GaAs quantum well with barriers consisting of AlAs/GaAs short-period superlattices [125] made it possible to observe QHE in cylindrical heterostructures. For this, 192 nm-thick Hall bars were created on the surface of an AlAs/GaAs microtube with a radius of 24 μm (see figure 28(a)). The electron mobility in such a system was

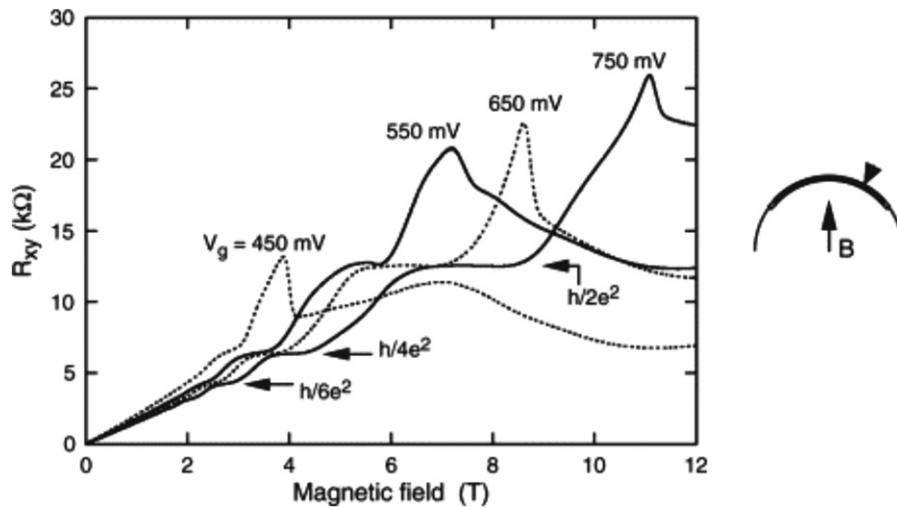


Figure 27. Hall magnetoresistance of suspended cylindrical 2DEG. Reprinted from [186], Copyright (2003), with permission from Elsevier.

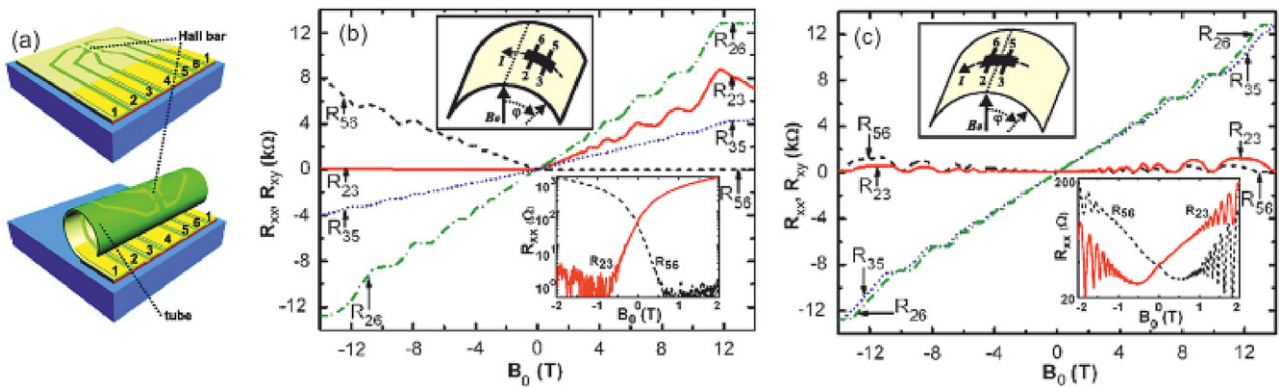


Figure 28. (a) Suspended Hall bar on cylindrical surface of an AlAs/GaAs microtube with a radius of 24 μm . Longitudinal and transverse resistances of the cylindrical 2DEG vs magnetic field measured for different orientations of one and the same Hall bar with respect to the magnetic-field direction. The external magnetic field is oriented normally to the surface (b) at a position somewhere outside the region between the contacts and (c) roughly at the central point of the Hall bar. The upper insets show the experimental geometries, and the lower insets show longitudinal resistances vs magnetic field on a logarithmic scale. The direction of the current I and the direction of the external magnetic field B_0 are shown with the dashed line and solid arrow, respectively. The resistances measured between different pairs of probes 2, 3, 5, and 6 are indicated with subscripts. Reprinted (figure) with permission from [187], Copyright (2007) by the American Physical Society.

about $10^6 \text{ cm}^2 \text{ V}^{-1} \text{ s}^{-1}$. It was shown that, in the cylindrical geometry, the Hall resistance behaves similarly to that in planar structures. Quantization plateaus are observed at the integer filling factors determined by the magnetic field component perpendicular to the cylindrical surface. At the same time, a giant asymmetry with respect to the direction of the magnetic field was found in the longitudinal magnetoresistance [187] (see figures 28(b) and (c)). This behavior is caused by the curvature of Landau levels in the presence of a transverse magnetic field gradient [188, 189] in cylindrical samples and can be explained within the framework of the model of edge current channels using the Landauer–Büttiker formalism [156, 175].

4. Micro- and nanoelectromechanical systems

4.1. Micro- and nanomechanical resonators

Since the suspended nanostructures have additional mechanical degrees of freedom in comparison to their non-suspended

counterparts, they can be used as mechanical resonators having submicron dimensions [4, 190–193]. In experimental works, the nanomechanical resonators are most often shaped as double-clamped bridges and cantilevers, whose mechanical oscillatory modes can be predicted with relatively high precision using analytical methods [194]. Due to their small size, the nanomechanical resonators have high resonant frequencies (up to GHz range [195]). At the same time, they are characterized by relatively high quality factors (up to millions [196]), i.e. their resonant frequencies can be measured with high precision. In addition, due to small mass, their resonant frequencies and quality factors are sensitive to external influence of various types, including the added mass of lightweight particles on the surface, electrical and magnetic fields, temperature, pressure etc [195, 197, 198]. This makes the nanomechanical resonators suitable for developing sensors of various physical quantities.

The nanomechanical resonators can be relatively easily driven into the nonlinear regime of oscillations and, therefore, are actively used as an experimental test site for studying the nontrivial phenomena of nonlinear dynamics [199, 200]. The bistability of nonlinear oscillations can be used for creation of nanomechanical memory elements [201, 202]. In addition to operating at high resonant frequencies, they are also interesting as human-made objects, potentially demonstrating quantum-mechanical behavior at low temperatures [203].

Nanomechanical resonators can be created from various materials, including Si [204–207], SiC [208], SiN [200, 209, 210], AlN [211], carbon nanotubes [195, 212–214], graphene [215, 216], etc. From the point of view of mechanical properties, the resonators based on AlGaAs/GaAs heterostructures are featured by their single-crystal structure [3, 4, 67, 68, 192, 201, 217–239], which makes it possible to reach relatively high quality factors. Another important aspect is that the AlGaAs/GaAs nanomechanical resonators combine both mechanical and electrical functionality, with their mechanical motion being coupled to electron transport via electrostatic and piezoelectric physical mechanisms. Thus, they represent hybrid nanoelectromechanical systems, where electron-transport phenomena can be studied under unusual conditions, namely, in the presence of additional mechanical degrees of freedom. Besides the fact that the effects emerging due to the electromechanical coupling are interesting in themselves, they also enable efficient actuation of resonant vibrations and their detection using on-chip all-electrical methods. It should be noticed that the AlGaAs/GaAs-based resonators, as well as those based on other materials, can be also used as optomechanical systems [217, 218, 240–243], however, the discussion of this aspect of their functionality is beyond the scope of the present paper.

Fundamental and applied research in the field of nanomechanical resonators is based on the knowledge about the physical mechanisms underlying the driving of mechanical motion, its detection and dissipation. In the present review we briefly describe the actuation and transduction methods applicable to AlGaAs/GaAs based nanomechanical resonators, discuss the damping mechanisms limiting their Q -factors and describe the current progress in studying the low-dimensional electron systems coupled with the nanomechanical resonators.

4.2. Actuation of nanomechanical motion

There are many methods which can be used to drive the oscillations of nanomechanical resonators [244, 245], and most of them are inherited from their larger-scale analogues—micromechanical systems. Probably the most simple and robust way is to use an external piezoelectrical shaker [196, 197, 226, 246, 247]. Similar ‘external’ driving scheme is the photothermal actuation based on the heating of the resonator surface by a focused laser beam with an amplitude-modulated power [207, 215, 248, 249]. In this case, the vibrations are driven due to the heating-induced thermal expansion. This method becomes increasingly more difficult with reduction of the resonator size, because its dimensions become less than the laser spot diameter. Its effectiveness

additionally drops at resonant frequencies approaching thermal relaxation time. Photothermal excitation is not used to drive the systems with a 2DEG based on AlGaAs/GaAs heterostructures, because light can drastically change electron transport properties of the low-dimensional system [250, 251].

Oscillations of nanomechanical resonators can be driven using the magnetomotive scheme [198, 204, 206, 208, 211, 236, 252]. In this case, to drive the vibrations, the resonator is placed in a magnetic field, and an alternating electrical current is passed through it at the resonant frequency. To achieve a sufficiently large Lorentz force, a high magnetic field of several Tesla is needed, which is usually obtained using helium-cooled superconductive magnets. The magnetomotive scheme can be successfully used to drive the flexural vibrations of the double clamped bridges at the fundamental mode, however, its usage for driving the higher modes and for driving the resonators of arbitrary shapes is limited.

The most interesting, especially for the possible applications, are the actuation schemes that can be implemented on-chip, with a minimal need for external devices. Among these methods, the most straightforward are the piezoelectric [4, 192, 201, 220] and capacitive [195, 209, 212–216, 221, 222] methods. In the first case, an alternating voltage is applied between the conductive layers being a part of the resonator, for example, between a 2DEG and a metal gate covering its surface. Alternatively, the voltage can be applied between different doped layers grown in a single epitaxial process [219]. Due to the piezoelectric effect, the electric field appearing between the layers induces mechanical stress which, in turn, can create a bending moment driving the vibrations. In addition to the alternating voltage, a dc voltage can be applied to tune the actuation efficiency [219] and the resonant frequency. As shown in reference [220], the efficiency of the piezoelectric driving of nanomechanical resonators based on AlGaAs/GaAs heterostructures is mainly limited by the resistance of the 2DEG leads which, together with the large parasitic inter-electrode capacitance, forms a low-pass filter significantly reducing the actual voltage between the resonator and the gate in comparison to that applied between the contact pads. Nonetheless, the piezoelectric actuation can be used to drive flexural and torsional vibrations of the resonators with submicron dimensions even at room temperature.

One of the alternative ways to on-chip drive the oscillations is to use the electrostatic interaction between a resonator and a nearby gate, mechanically separated from the resonator (see figure 29(a)). Voltage V_G applied between them induces a force acting on the resonator

$$F = \frac{\partial C}{\partial x} \frac{V_G^2}{2}, \quad (10)$$

where C is the gate-resonator capacitance and x is the generalized coordinate (such as the displacements of a cantilever tip or a bridge center). If the voltage is a sum of dc and ac components $V_G = V_{DC} + V_{AC} \cos \Omega t$, then there is an ac force at frequency Ω , which can drive the resonant vibrations:

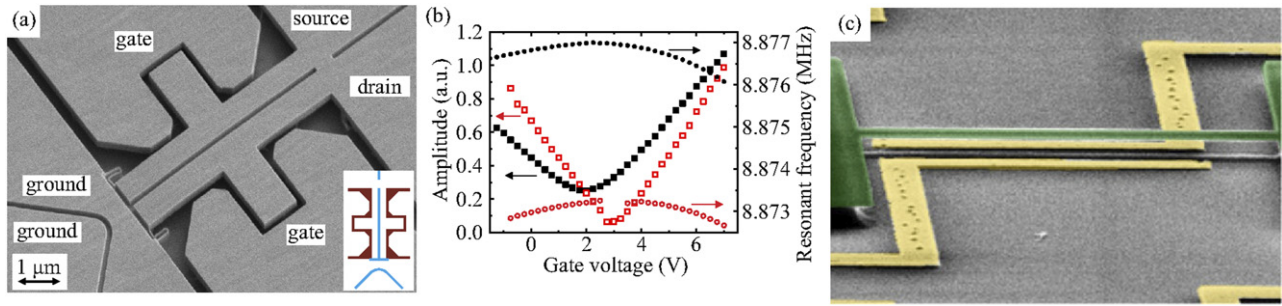


Figure 29. (a) A scanning electron microscope image of an AlGaAs/GaAs resonator with a 2DEG whose vibrations can be driven using in-plane side gates by capacitive electrostatic force. Reprinted from [228], with the permission of AIP Publishing. (b) Measured amplitude and resonant frequency as functions of the dc gate voltage component. Data shown in black are obtained before a short illumination, in red—after illumination. Reprinted from [221], with the permission of AIP Publishing. (c) An example of a SiN nanomechanical resonator driven using bottom gates (colored in yellow) by dielectric gradient force. Reprinted (figure) with permission from [210], Copyright (2010) by the American Physical Society.

$$F_{AC} = \frac{\partial C}{\partial x} V_{DC} V_{AC} \cos \Omega t. \quad (11)$$

A feature of the low-dimensional electron systems based on the AlGaAs/GaAs heterostructures is the presence of relatively wide (of order of hundreds nanometers) electron-depleted regions near the lateral edges [253]. This depletion occurs due a large density of surface states causing the Fermi level pinning near the middle of the bandgap at the surface. Because of the depletion, suspended resonators with a 2DEG are conductive only if their width exceeds some critical value, which is usually larger than the resonator thickness. Thus, the resonant mode with the lowest frequency typically corresponds to the resonator motion in direction orthogonal to the surface (out-of-plane vibrations), while the in-plane vibrations are much stiffer and rarely observed.

For the capacitive actuation to be effective, the gate-resonator capacitance should strongly depend on the resonator displacement x in the direction corresponding to the driven vibrational mode. Thus, to drive the out-of-plane vibrations, it would be preferable to have a gate placed directly under the resonator. However, deposition of metal there is practically impossible. A solution which can be in principle used is to create the gates at the substrate as close as possible to the resonator (see figure 29(c)). However, this can be challenging to achieve after the resonator is mechanically suspended. Fortunately, it has been shown that the out-of-plane vibrations can be successfully driven using in-plane side gates, because the substrate having a high dielectric constant and being under the resonator breaks the system symmetry and makes the gate-resonator capacitance dependent on the out-of-plane displacement x of the resonator. The side gates can be easily created at the same stage when the topology of the resonator is defined by just anisotropic etching of narrow trenches down to the sacrificial layer, which mechanically separates the gates and the resonator. The electrostatic capacitive origin of the force driving the vibration can be experimentally confirmed by the two features of this actuation scheme. The first feature is the linear dependence of the oscillation amplitude on the dc gate voltage component predicted by equation (11). The second is related to the change of the effective spring constant of the system due to the electrostatic forces.

In the vast majority of cases, the capacitance C between the gate and the resonator depends nonlinearly on the resonator displacement x . Taking into account the first nonlinear term, it can be expressed in the following form:

$$C(x) = C_0 + C'x + C''x^2/2. \quad (12)$$

Substitution of this equation into equation (10) shows that there is a force component linearly dependent on x (here we are not interested in other components):

$$F_s = \frac{C''}{2} V_{DC}^2 x. \quad (13)$$

The coefficient $\frac{C''}{2} V_{DC}^2$ can be considered as an electrostatic spring constant, additive to the mechanical one. The presence of this force leads to a shift in the resonant frequency Ω_0 proportional to the squared dc gate voltage component:

$$\Delta\Omega_0 = -\frac{C'' V_{DC}^2}{4m\Omega_0}. \quad (14)$$

Since the coefficient C'' is usually positive, the capacitive gate-resonator interaction typically leads to a negative shift of the resonant frequency with V_g applied. This effect called electrostatic softening [212] is the second hallmark of the capacitive actuation which, together with the linear amplitude dependence was observed in [222], thus confirming that the in-plane side gate drives the out-of-plane vibrations via the capacitive actuation.

While equations (11) and (14) predict that, at $V_{DC} = 0$, the oscillation amplitude is zero and the resonant frequency is maximal, in experiment these two specific points often correspond to different non-zero gate voltages [212, 221] (see figure 29(b)). These voltage shifts from zero can be explained by the presence of built-in charges in the vicinity of the gate and the resonator. The numerical estimates reported previously [221] show that, in particular, the piezoelectrically induced alternating built-in charges which appear when an AlGaAs/GaAs-based resonator vibrates, can explain the magnitude of the voltage shifts (of the order of volts). Moreover, experiment shows that, when electrical charge is spatially redistributed by a short illumination at low temperatures, the voltages corresponding to the specific points further shift. This

shows that the features of the capacitive actuation can be used for the creation of charge sensing devices.

Additional experimentally observed discrepancy of the experimental results from that predicted by equation (11) is that the amplitude of the oscillations does not fall to zero at the gate voltage corresponding to the amplitude minimum. A hypothesis was proposed to explain this fact by the possible role of the poorly conducting 2DEG near the lateral edges [221]. Due to the poor conductivity, charge redistribution that occurs in these edge regions in response to an alternating change in the gate voltage lags from re-charging of the 2DEG bulk. Accordingly, the driving forces acting on the bulk and on the edge have different phases. Since electrostatic structure of the edge differs from that of the bulk, these forces are zeroed at different V_{DC} values. The presence of phase-shifted force acting on the edge can explain the observed non-zero amplitude at the minimum. Experimentally, this hypothesis is indirectly confirmed by the fact that q th amplitude minimum becomes much closer to zero after illumination, which makes confinement potential at the edge steeper, thus reducing the width of the poorly conducting near-edge regions [253].

4.3. Detection of nanomechanical motion

Similarly to the actuation schemes, the methods used to detect the motion [244, 245] of nanomechanical resonators can be conditionally divided into external and internal with respect to the system. In the case of the resonators with micro-scale lateral dimensions, one of the most sensitive methods to detect their motion is the use of external optical interferometers (Doppler vibrometers) [196, 197, 207, 215, 229, 248, 249, 254, 255]. However, as the resonator dimensions reduced, sensitivity of this method drops, since the size of a focused spot is limited by the diffraction limit. In most of the practical cases, the minimal size of the light spot is of the order of micrometers. For the interferometric methods to be effective, the motion direction should coincide with the optical path, and this limits their use for detection of in-plane motion. Finally, since light can drastically change electron-transport properties of semiconductor low-dimensional electron systems, the optical methods are not typically used to study the nanomechanical resonators based on AlGaAs/GaAs heterostructures with a 2DEG.

III–V materials, non having inversion symmetry, demonstrate piezoelectric properties, and, due to this, the mechanical resonators made from them are featured by the possibility to on-chip transduce their vibrations into an electrical signal. The first method utilizing the piezoelectric effect is based on the detection of the piezoelectrically generated voltage [4, 201, 223, 234]. To achieve this, the resonator is partially covered with a metal top gate, like in the case of piezoelectric actuation. Due to the reverse piezoelectric effect, oscillation-induced mechanical strain leads to electrical polarization of the resonator body, and a small, but still measurable voltage appears between the gate and the 2DEG contained in the resonator. If the size of the resonator is reduced, the role of the parasitic capacitance (that of the cables and that between

the contact pads) strengthens, and, in the case of nanomechanical resonators, the piezoelectric transduction scheme becomes difficult to implement. To partially overcome this drawback, a low-temperature voltage preamplifier placed in a close proximity to the experimental sample can be used [223].

Mechanical deformation of the resonators based on III–V materials also leads to a change in the conductivity of the 2DEG contained in them, and this piezoresistivity can be used to detect the motion [3, 224, 226, 230, 256] (see figure 30). The bending-induced conductivity change can arise due to the deformation potential and due to the piezoelectric effect. As has been experimentally shown in reference [224], in the case of the AlGaAs/GaAs resonators, the piezoelectric effect dominates. To check this, two nanomechanical cantilevers oriented in the orthogonal crystallographic directions were created with 2DEG constrictions placed near their clampings. Flexural oscillations of the cantilevers were identically driven in the direction perpendicular to the surface, and the alternating change in the resistances of the constrictions was measured at the oscillation frequency. The resulting deviations of the resistances were phase-shifted by 180° , indicating the dominating role of the piezoelectric effect in the resistance change.

According to the existing models [4, 224, 256], the bending-induced change in the resistance is determined by the change in the 2DEG density. When a resonator is bent, a piezoelectric bound charge appears in its bulk and at the surface. The 2DEG screens this additional charge by redistributing the electron density in such a way to minimize the energy of the system. The resultant spatial distribution of the bending-induced density change, strongly depends on the conditions at the surface. The simplest situation is when the surface is entirely covered by a metal gate. In the case of a thin AlGaAs/GaAs nanomechanical beam, the bending-induced density change is inversely proportional to the bending radius at a given point:

$$\delta n = \frac{e_{14}(t - d_{2DEG})}{4eR}, \quad (15)$$

where e_{14} is the piezoelectric constant of the resonator material, t is the resonator thickness, d_{2DEG} is the depth at which the 2DEG is placed, e is the elementary charge and R is the bending radius. If the surface is naked, then the density change is maximal at the boundary between suspended and non-suspended parts of the system, i.e. at the clampings, with its signs being opposite in these two parts. If the 2DEG constriction is created using a metal split gate, then the spatial distribution of the density change resulting from the bending becomes similar to that induced by a change in the gate voltage. Thus, the bending works as the ‘piezoelectric gating’ which can be used to modulate the 2DEG density [256]. It should be noticed that, in the case of the split-gate devices, to maximize the magnitude of the electrical response to the mechanical vibrations, the 2DEG should be placed in the middle of the resonator thickness, i.e. at the neutral plane, where the mechanical strain is zero.

To overcome the difficulties associated with high-frequency measurements in the presence of parasitic capacitances and at relatively high resistances of the samples, the heterodyne down-mixing technique can be used [212, 222, 247]. Notice

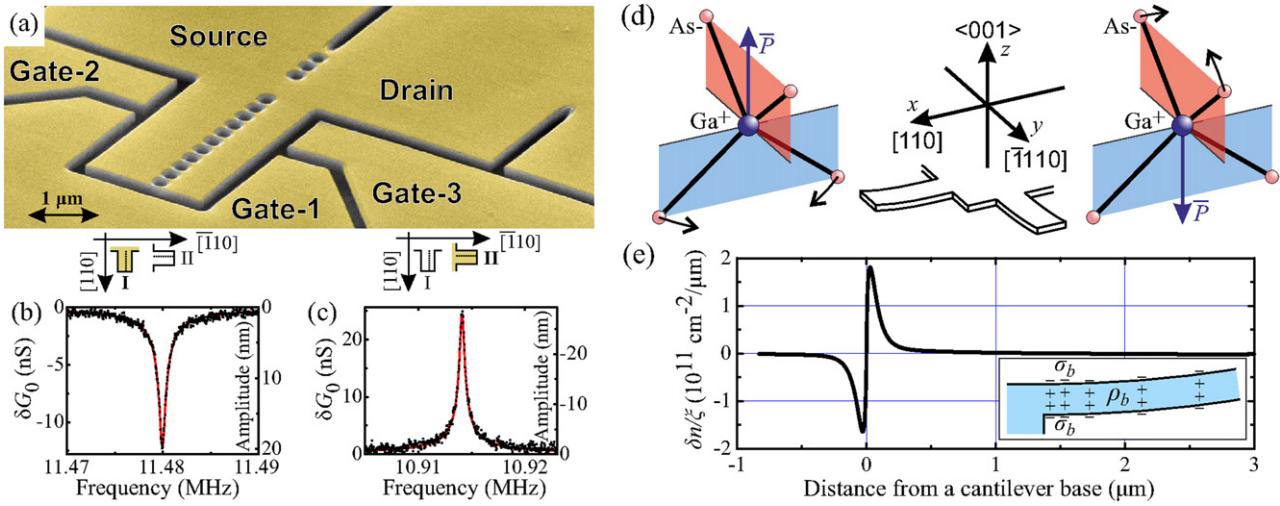


Figure 30. (a) A nanomechanical cantilevered resonator containing a 2DEG. A wide gap between the etched halls is a 2DEG constriction, whose conductance is sensitive to mechanical vibrations. (b) and (c) Resonators oriented in the orthogonal crystallographic directions demonstrate opposite piezoelectric responses to mechanical vibrations. (d) Simplified picture showing the origin of the piezoelectric response anisotropy. (e) Electron density change δn per unit displacement ζ of the cantilever free end as a function of the distance from the clamping. The shown dependence is calculated for $[110]$ -oriented cantilever and should be negated for $[-110]$ -oriented cantilever. Reprinted (figure) with permission from [224], Copyright (2016) by the American Physical Society.

that the nanoelectromechanical system itself can play the role of the mixer. Let conductance G of a 2DEG constriction linearly depend on mechanical displacement x of the resonator from its equilibrium position

$$G = G_0 + \frac{\partial G}{\partial x} x. \quad (16)$$

Let the resonator perform periodic oscillations

$$x = a \cos(\Omega t + \phi), \quad (17)$$

where the phase ϕ is measured relatively to the driving force. The oscillation-induced conductance change

$$G = \frac{\partial G}{\partial x} a \cos(\Omega t + \phi) \quad (18)$$

can be detected by application of a dc source–drain voltage to the constriction and by measuring the current flowing through it at the driving frequency Ω . However, at a high frequency, all the parasitic components of the circuitry complicate the measurements and should be taken into account. Moreover, with rare exceptions, the bandwidth of the existing lock-in amplifiers is limited by several hundreds kHz. Alternatively, an ac source–drain voltage having a frequency close to the driving one can be applied to the constriction

$$V = V_0 \cos(\Omega - \omega)t, \quad (19)$$

where ω is a low frequency convenient for the measurements. The resulting current $I = VG$ flowing through the 2DEG constriction contains a low-frequency component

$$\delta I = V_0 \frac{\partial G}{\partial x} a \cos(\omega t + \phi) \quad (20)$$

proportional to the oscillation amplitude a and sensitive to their phase ϕ . The measurement of this current component makes

it possible to detect the high-frequency vibrations and, at the same time, to partially eliminate the drawbacks of the measurements at high frequencies. To reduce the noise influence on the output signal, it is usually reasonable to choose frequency ω higher than the cutoff frequency of the $1/f$ noise. An additional advantage of using the heterodyne down-mixing technique is the elimination of high-frequency cross-talk.

4.4. Dissipation

There is a series of physical mechanisms underlying the dissipation of oscillatory energy in nanomechanical resonators. In the existing comprehensive reviews these mechanisms are discussed in detail [190, 191, 257]. The damping mechanisms can be conditionally divided into extrinsic and intrinsic with respect to the system. The former include the radiation of phonons into the material bulk from the clampings (clamping loss) [258], the damping from the surrounding medium [254], Ohmic losses in the circuitry etc. The internal loss mechanisms include those related to the interaction between phonons (Akhiezer [259] and thermoelastic [260] damping), defect motion, Ohmic losses [4] in the resonator, surface losses [225], the dissipation due to two-level systems [191, 261] etc. In the case of the AlGaAs/GaAs resonators, the dissipation processes are not very well investigated, and the quality factors cannot be predicted in advance. In the present review article we will focus at some specific features related to the dissipation in the AlGaAs/GaAs resonators.

A common observation is that the quality factor decreases with down-scaling of the resonators, i.e. with increasing surface-to-volume ratio [205, 252, 257] (see figure 31). This fact shows that the dissipation is largely determined by the surface processes, especially in the case of single-crystal resonators, where the surface is much more disordered than the

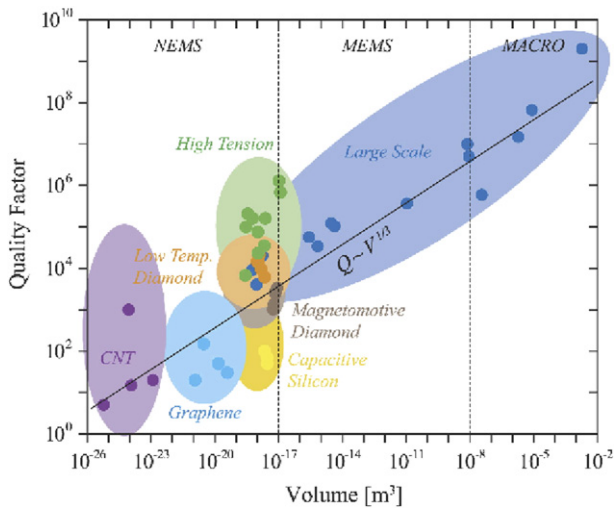


Figure 31. Q -factor dependence on the size of mechanical resonators. Reprinted from [257], Copyright (2014), with permission from Elsevier.

bulk. The role of the surface dissipation in GaAs nanomechanical resonators has been studied in reference [225]. It was shown that the surface modification by atomic layer deposition can strongly decrease the Q -factor.

A detailed experimental study of the dissipation in GaAs-based nanomechanical resonators has been reported in reference [252]. A feature of the resonators based on this material is the presence of dissipation (the inverse Q -factor) peaks at temperatures close to 30 K. Similar peaks in similar temperature range were observed on samples with different geometry and different material composition [226, 227] (see figure 32). This shows that the presence of these peaks is a universal feature of the nanomechanical resonators based on AlGaAs/GaAs heterostructures, and, thus, clarification of their origin is of special importance.

Specific temperatures at which these peaks are observed make it necessary to consider the thermoelastic damping [226, 260] as one of the possible physical mechanisms responsible for their appearance. The thermoelastic damping originates from thermodynamically irreversible heat flow induced by the temperature gradients accompanying the mechanical deformation. The thermoelastic damping contribution into the overall dissipation is proportional to the squared thermal expansion coefficient. With decreasing temperature, this coefficient decreases [262], reaches zero at approximately 50 K, then becomes negative and, after reaching a local maximum at nearly 30 K, tends to zero. Accordingly, the related dissipation should reach its minimum at the temperatures corresponding to zero thermal expansion coefficient and give a local maximum at nearly 30 K. Estimates show that the Akhiezer [225, 259] damping, arising due to the bending-induced modification of the phonon spectrum should be also maximized at the temperatures close to 30 K. Notice that the existing models of the dissipation originating from the phonon–phonon interaction are well developed for the case of diffusive phonon transport. For the resonators having submicron thickness, the mean free path of the phonons becomes larger than the system

dimensions, and the role of the thermoelastic and Akhiezer damping mechanisms requires a revision [61, 260]. The dissipation peaks at nearly 30 K can be also explained by the influence of defects, impurities and two-level systems [252, 261]. Experimentally observed quadratic dependence of the dissipation on magnetic field indicates that these centers are charged and possibly represent the electronic donor impurities.

It is natural to consider the intentionally introduced dopants as one of the potential dissipation sources. In the case of AlGaAs/GaAs heterostructures, the most often used dopant is (Si). It is well known that Si atoms can play the role of the shallow donors or, alternatively, they can form so-called DX-centers [250, 251, 263]. These centers represent the Si atoms shifted from a substitutional position toward one of the nearest interstitials. A well-known effect associated with the DX-centers is the persistent photoconductivity at low temperatures, i.e. the illumination-induced conductivity growth non disappearing after the light is turned off. According to the existing models, the persistent photoconductivity is attributed to the fact that, to be back-captured by a donor, a photoemitted electron needs to overcome a potential barrier associated with a lattice relaxation accompanying the capture process.

In reference [228], it was shown that the dissipation in AlGaAs/GaAs-based nanomechanical resonators also demonstrates the effect of persistent change, similar to the persistent photoconductivity. Moreover, a short illumination makes the dissipation peak at 30 K much less prominent and improves the Q -factor at that temperature. Since light can hardly lead to persistent effects in the phonon sub-system, the results so obtained show that the dissipation peak observed at 30 K is not associated with the thermoelastic and Akhiezer damping mechanisms. Taking into account the similarity of the persistent photoconductivity and the persistent Q -factor change, it probably makes sense that the latter can be also explained by the DX-centers, as suggested in reference [252]. The idea proposed in reference [228] to explain the dissipative role of the DX-centers is built on the assumption that these centers can be spatially reoriented [261, 264], with the preferable orientations being stress-dependent, and the characteristic relaxation time being comparable to the vibration period.

An important method which can be used to improve the quality factor of nanomechanical resonators is the introduction of longitudinal tensile stress (damping dilution). Tension increases the energy stored in the resonator, but it does not lead to a growth in the energy loss [210]. In other words, the tension increases the resonant frequency, with the width of the resonance remaining unchanged. For example, pre-stressed SiN membrane resonators demonstrate quality factors over a million [196].

The resonators are created from the top few layers of the heterostructure which are above the sacrificial one. To make a resonator tensed, there should be a lateral tensile stress in these layers, i.e. their lateral lattice constant a_R should exceed its natural value a_{Rn} . Usually, the nanomechanical resonators are thin enough for the growth of their material to be pseudomorphic, which means that $a_R = a_{SL}$, where a_{SL} is the lateral lattice constant of the sacrificial layer. Thus, to tense the resonator, the condition $a_{Rn} < a_{SL}$ should be fulfilled.

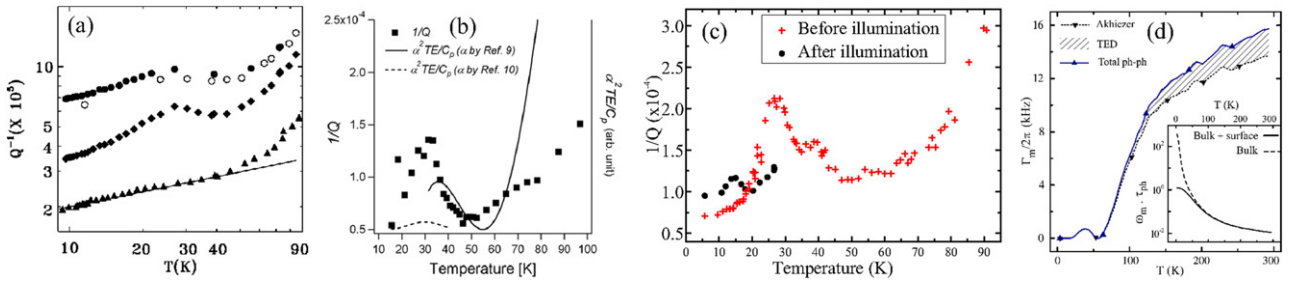


Figure 32. Dissipation peaks universally observed in AlGaAs/GaAs-based micro- and nanomechanical resonators at the temperatures close to 30 K. Reprinted (figure) with permission from [252], Copyright (2002) by the American Physical Society. [226] John Wiley & Sons. [Copyright © 2008 WILEY-VCH Verlag GmbH & Co. KGaA, Weinheim]. Reprinted from [228], with the permission of AIP Publishing. Reprinted (figure) with permission from [225], Copyright (2018) by the American Physical Society.

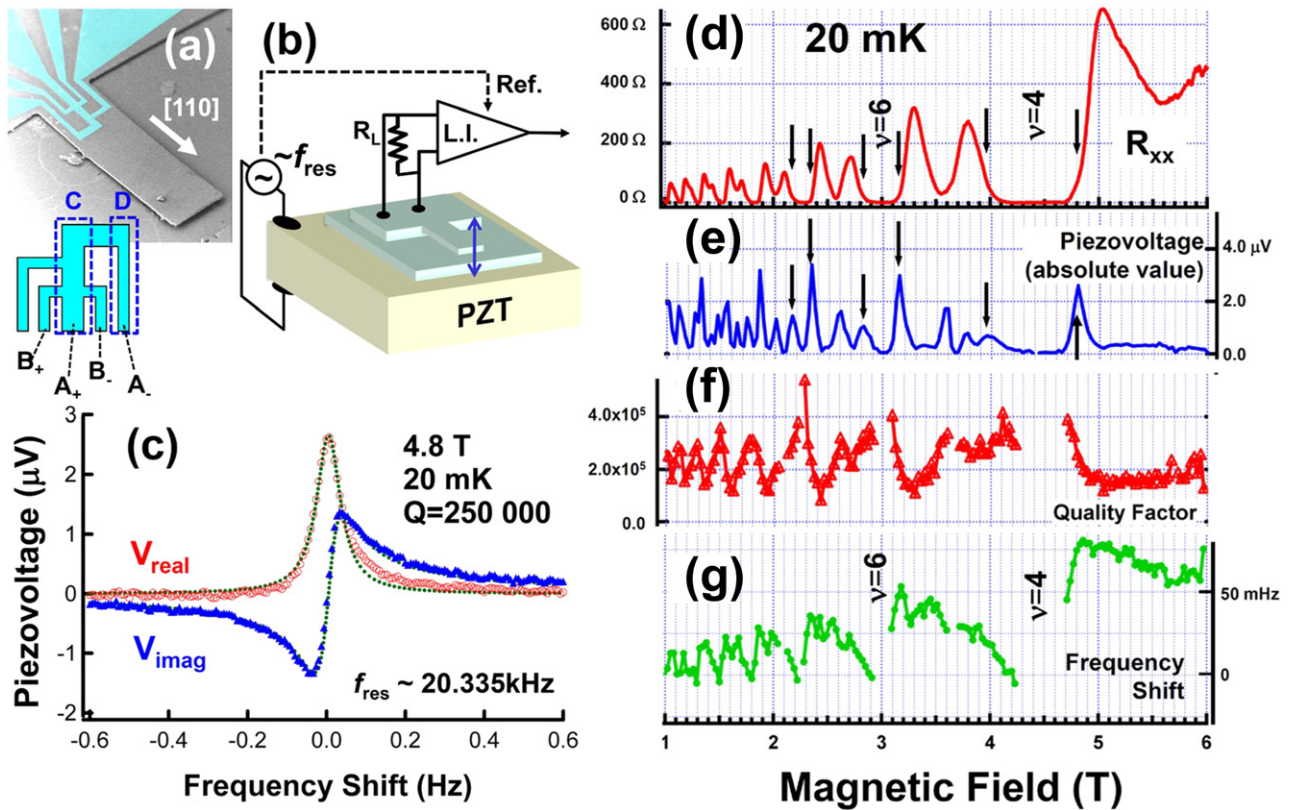


Figure 33. (a) Scanning electron microscope image of a micromechanical $200 \times 50 \times 1.3 \mu\text{m}$ resonator containing a 2DEG Hall bar (blue). (b) Schematic of the voltage measurement setup. (c) Magnetopiezovoltage generated as a function of actuation frequency at 4.8 T between contacts A_+ and A_- . Longitudinal resistance (d), piezovoltage (e), resonance frequency shift (f), and Q -factor (g) as functions of magnetic field. Reprinted from [232], with the permission of AIP Publishing.

AlGaAs/GaAs heterostructures are often considered as stress-free ($a_R \approx a_{Rn} \approx a_{SL}$), since the lattice constants of the $\text{Al}_x\text{Ga}_{1-x}\text{As}$ solid solutions are almost independent on the aluminum content x . Thus, a modification of the heterostructure by introduction of additional elements is needed to make its top layers tensed. This can be done by either increasing a_{SL} or reducing a_{Rn} . The former approach was realized in reference [229], where the resonators were created from a 200 nm-thick GaAs layer grown on the top of a metamorphic In-containing buffer thick enough for its top layers to be relaxed ($a_{SL} \approx a_{SLn}$). Since In introduction increases the lattice constant, the topmost GaAs layer is grown tensed, provided that its thickness remains less than the critical one. An

increase in the Q -factor from 1800 to 19 000 at room temperature was achieved using this method. The method based on a_{Rn} reduction was implemented in references [255, 265]. In reference [255], a standard AlGaAs sacrificial layer was used, but InGaP layers were introduced into the resonator material. The natural lattice constant of these layers is below that of AlGaAs, and thus, again, the created resonators are subjected to tensile strain. The reported Q -factors are up to 70 000 at room temperature. In reference [265], tensile-stressed GaNAs resonators were studied and shown to have a Q -factor of 120 000 at room temperature. Similar GaAs resonators had the Q -factor of only 4000.

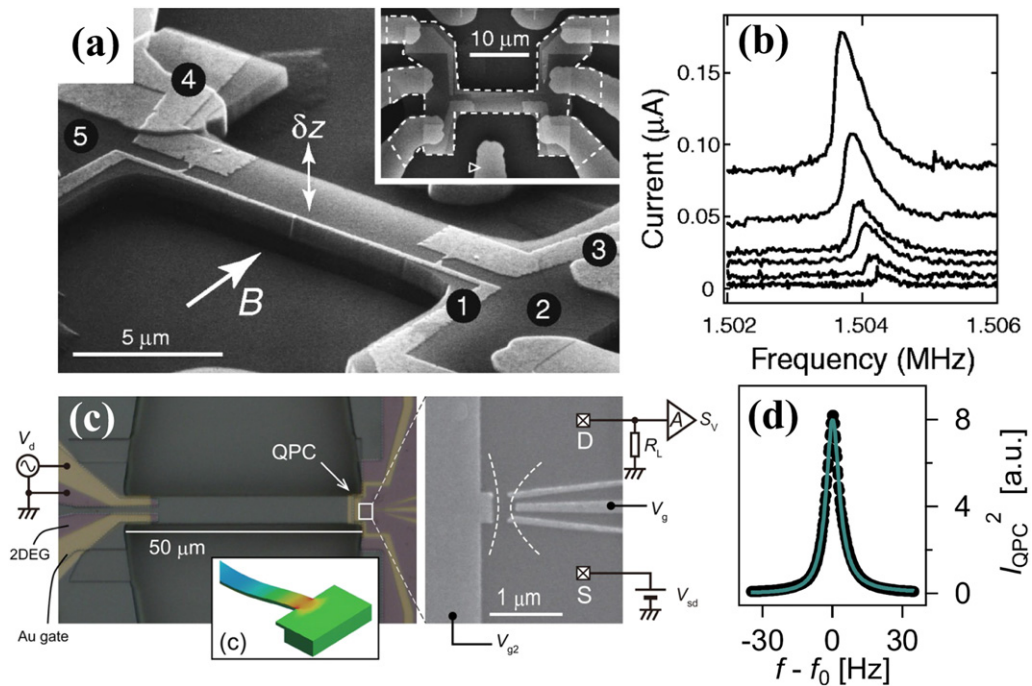


Figure 34. (a) and (c) QPCs integrated with nanomechanical resonators and used for sensing their mechanical motion. In (a) two QPCs are formed by gate pairs (1, 3) and (1, 4). Right: examples of the measured QPCs responses to mechanical vibrations. Reprinted from [67], with the permission of AIP Publishing. Reprinted from [68], with the permission of AIP Publishing.

4.5. Coupling between electron-transport phenomena and nanomechanical motion

At an early stage of investigation of the AlGaAs/GaAs-based electromechanical systems, the 2DEG was mostly exploited to sense the mechanical motion. In the pioneering work of Beck *et al* [230], a 2DEG-based field effect transistor was used to sense the flexural vibrations of a macroscopic (9×2.5 mm) cantilever, representing an entire semiconductor chip with one of the edges mechanically clamped. In reference [3], this technique was used to sense the non-resonant motion of a micro-machined ($65 \times 11.4 \times 0.25$ μm) cantilever for the scanning probe microscopy purposes. Additionally, a much smaller ($3 \times 2 \times 0.125$ μm) cantilever was presented, however, its mechanical functionality was not demonstrated.

In reference [231], a 2DEG contained in a double-clamped $6 \times 0.5 \times 0.114$ μm beam was used to detect the flexural oscillations of the latter using the piezoresistive response, i.e. by measuring an ac voltage generated on the vibrating beam when a dc current is applied to it. The resonant frequency of the vibrations corresponds to out-of-plane mode, and the vibrations are driven using an in-plane side gate. No amplitude dependence on dc component of the gate voltage was observed, and, based on this, the authors concluded that the vibrations are driven due to a physical mechanism different from the capacitive gate-resonator interaction. As an alternative, the dipole–dipole interaction was proposed to explain the driven vibrations.

As has been shown later, the 2DEG is not only sensitive to mechanical motion, but also imposes a back action on the mechanical properties of the micro- and nanomechanical resonators, with the magnitude and character of this back action

depending on the 2DEG electronic state (see figure 33). In reference [232], a micromechanical resonator containing a 2DEG was studied at high magnetic fields corresponding to the QHE. It was shown that the resonant frequency decreases, and the quality factor increases at the magnetic fields corresponding to the edges of the quantum-Hall-effect plateaus. Moreover, the 2DEG can play a significant dissipative role in nanoelectromechanical systems: the quality factor had almost doubled near the edges of the plateaus. Thus, the micromechanical measurements can be used to investigate the electron-transport phenomena in isolated systems, including the localized electron states in the 2DEG.

Another well-known electron-transport phenomenon which has been traced in the micromechanical measurements is the mesoscopic conductance fluctuations. In reference [266], a change in the resistance of a nanomechanical cantilever due to its mechanical oscillations was measured as a function of magnetic field. It was found that the electrical response to vibrations demonstrates a reproducible oscillatory dependence on the magnetic field, similar to the well-known universal mesoscopic conductance fluctuations.

In reference [233], a 2DEG based on a heterostructure containing paramagnetic Mn ions was created on the top of a suspended GaAs cantilever. By measuring the resonant frequency of the cantilever as a function of magnetic field, the total magnetization of the system was estimated. Thus measured magnetization demonstrated the de Haas–Van Alphen oscillations. It was shown that these oscillations had a series of unusual features. First, the oscillations were unusually smooth and did not demonstrate a sawtooth shape typical for high-mobility GaAs 2DEG. Second, they were aperiodic with respect to $1/B$. Third,

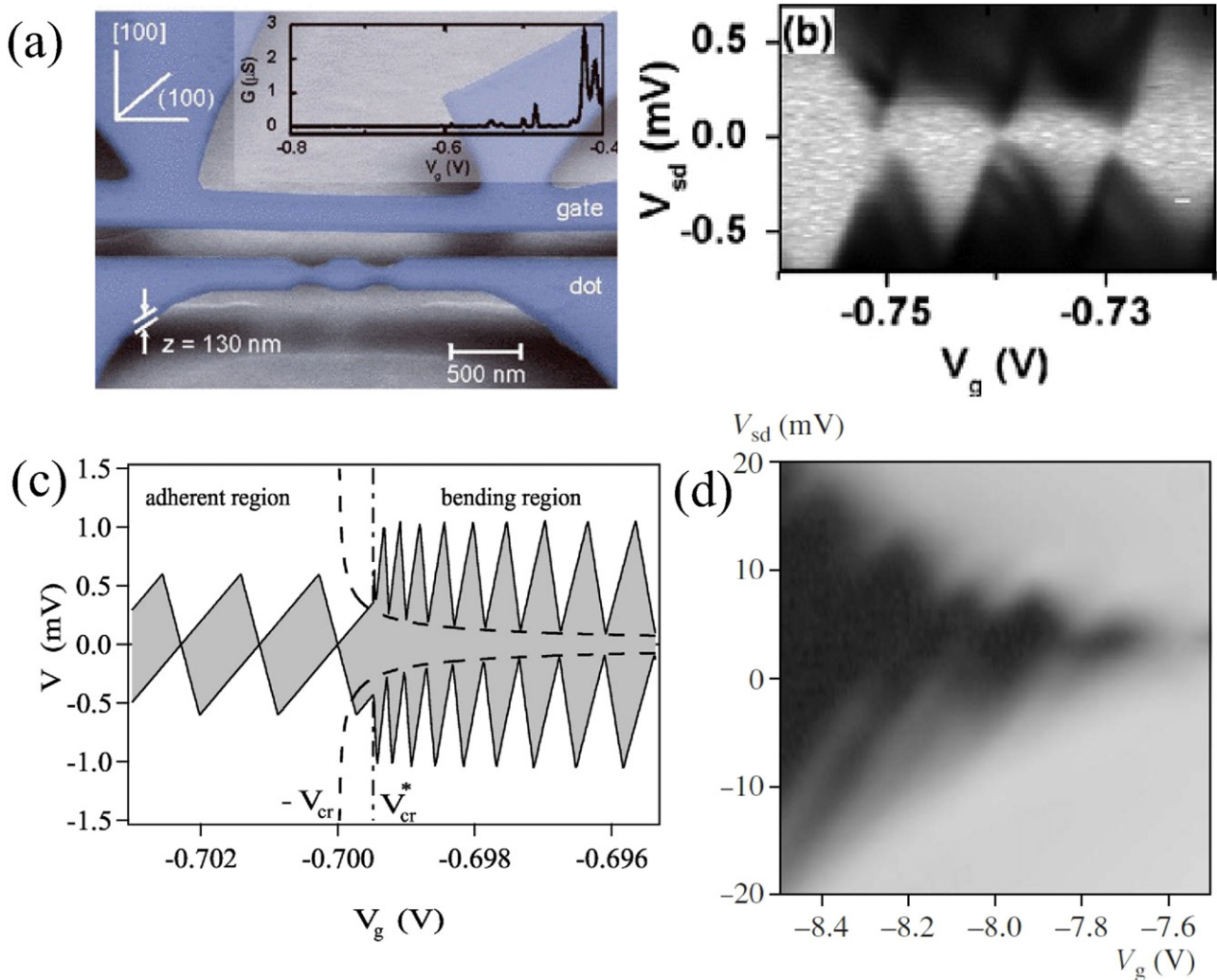


Figure 35. (a) Scanning electron microscope image of a suspended quantum dot. (b) and (d) Grayscale plots showing the conductance dependence on gate (horizontal axes) and source–drain (vertical axes) voltages in suspended quantum dots. Conductance is shown by color; dark regions correspond to zero value. Due to mechanical flexibility, the diamond-like black regions (Coulomb blockade diamonds) stick together, such the Coulomb peaks are not observed at zero source–drain voltage. The additional blockade can be explained by either emission of phonons (b) or by elastic deformation (d) accompanying electron tunneling. (c) Theoretically predicted elastic deformation blockade in suspended quantum dots. Reprinted (figure) with permission from [267], Copyright (2004) by the American Physical Society. Reprinted (figure) with permission from [268], Copyright (2003) by the American Physical Society. Reproduced from [72], with permission from Springer Nature.

with increasing temperature, their extrema shifted to lower B . It may be noted that, using a hybrid nanomechanical system integrated with a 2DEG, the features of the total density of electron states can be revealed, while the ordinary electron transport measurements are used to study only the density of states near the Fermi level.

Experimental studies of the micro- and nanomechanical resonators containing electron systems with a further reduced dimensionality were largely stimulated by the need to have a sufficiently sensitive on-chip motion detector to investigate the nanomechanical vibrations in the quantum regime (see figure 34). In reference [67], it was proposed to use a QPC combined with a nanomechanical resonator to sense oscillations of the latter. Although 1D conductance quantization was not demonstrated, the QPC was shown to be more sensitive to displacement than the ordinary 2DEG. Subsequently, it was shown [68] that the sensitivity of the QPC to

nanomechanical motion can be further improved by placing the QPC at the region of maximal mechanical strain, namely, near the clamped edge. The achieved sensitivity was 23 times the standard quantum limit.

The success of hybrid systems coupled with QPCs was later translated into novel mesoscopic systems such as quantum dots and single-electron transistors (SETs). In reference [234], it was theoretically proposed to place a metal gate of a SET over a clamped edge of a nanomechanical resonator and to use the SET as a sensitive detector of the piezoelectrically induced charge at the gate. Experimentally, however, this system was realized in a different configuration, namely, with the resonator capacitively coupled to the gate of an aluminum-based SET [235].

In addition, the nanomechanical resonators coupled to quantum dots were also studied. In reference [236], a system representing a suspended 2DEG-based quantum dot

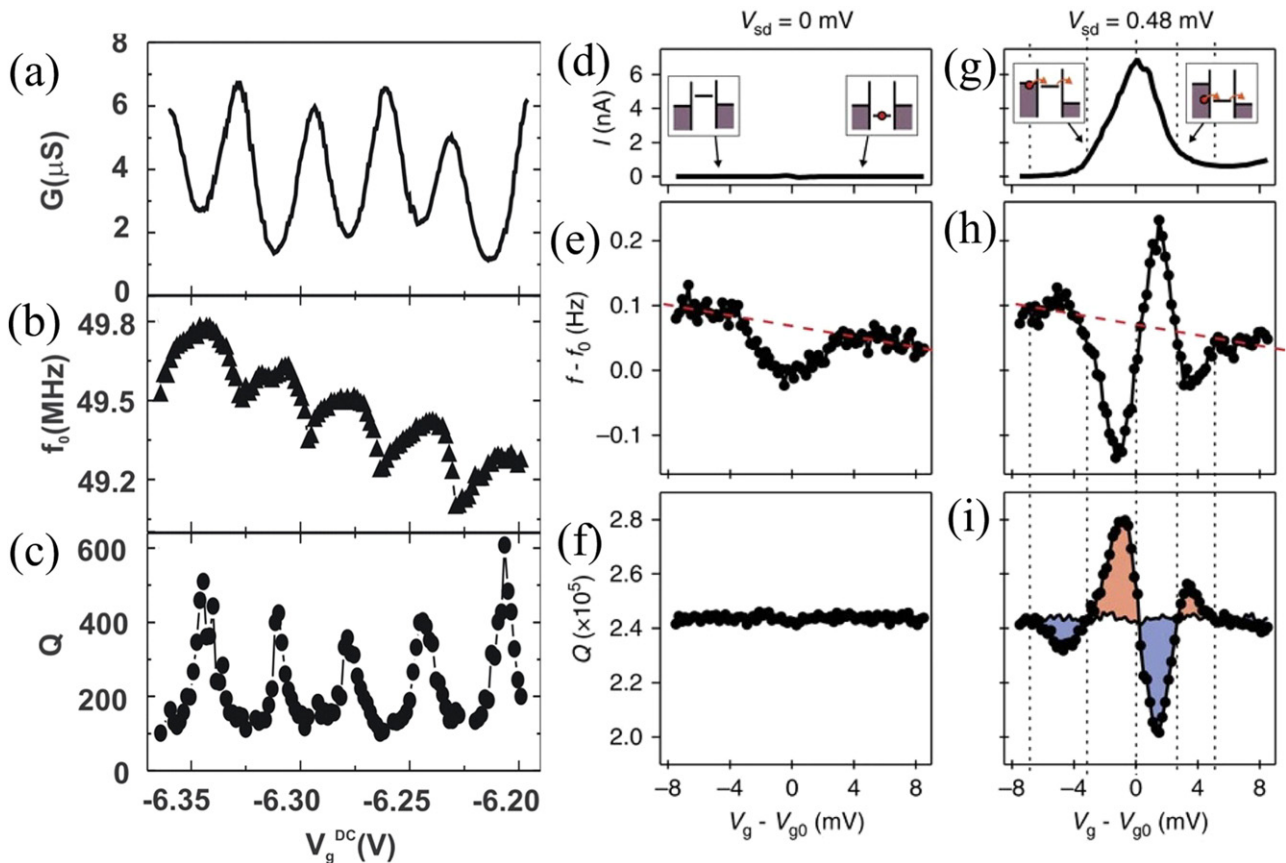


Figure 36. The back-action of single-electron tunneling near the Coulomb peaks (a), (d), (g) on the resonant frequency (b), (e), (h) and Q -factor (c), (f), (i) of nanomechanical resonators based on carbon nanotubes (a)–(c) and AlGaAs/GaAs heterostructures, From [214]. Reprinted with permission from AAAS. (d)–(i). In the latter case, the electron tunneling at non-zero source–drain voltage can lead to an enhance in the quality factor. Reproduced from [237]. CC BY 4.0.

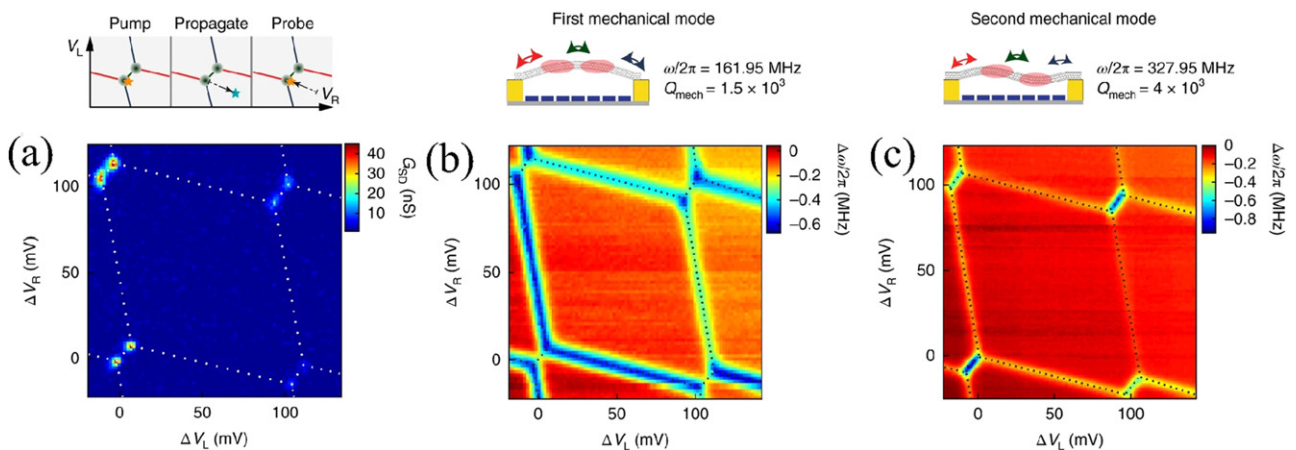


Figure 37. (a) Stability diagram showing conductance as a function of the gate voltages in a double quantum dot. Non-zero current is measured only in the triple points. (b) and (c) Stability diagrams showing the resonant frequency as a function of the gate voltages for the first (b) and second (c) vibrational model. The lines corresponding to dot-(Fermi sea) and inter-dot tunneling are visible. Reproduced from [213], with permission from Springer Nature.

neighboring a nanomechanical resonator has been created. The quantum dot was experimentally shown to demonstrate the Coulomb blockade, and the mechanical resonance detected using the magnetomotive technique was demonstrated, however, the coupling between them was not investigated. In reference [72], the elastic deformation blockade predicted by

Nishiguchi [267] was experimentally observed (see figure 35). The effect manifests itself as a blockade of electron tunneling additional to the Coulomb one, appearing due to the fact that the tunneling is accompanied by mechanical deformation of the beam containing the quantum dot, which requires additional energy. Experimentally, it is observed as the

absence of the Coulomb peaks at zero source–drain voltage in conductance dependence on the gate voltage. The peaks are, however, observed at non-zero source–drain voltage. Similar additional blockade was observed in reference [268], however, it was explained by the excitation of the local phonon modes accompanying electron tunneling.

Recently, the back-action effects in the resonant electromechanical systems with quantum dots have become a topic of considerable interest (see figure 36). First results of these studies were obtained in the systems based on suspended carbon nanotubes [214], where quantum dots naturally form between the contacts or can be formed by the gates [213]. A common observation is the presence of dips in the resonant frequency and quality factor measured as functions of the voltage applied to the gate controlling the quantum dot. These dips are observed at the gate voltages corresponding to the Coulomb peaks, where electrons can tunnel through the quantum dot. The back-action effects were also observed in AlGaAs/GaAs-based systems. In reference [237], the study of a bridge-like micromechanical AlGaAs/GaAs resonator with a quantum dot placed near one of its clamped edges was reported. At non-zero source–drain voltage, both the resonant frequency and the quality factor demonstrate features when the gate voltage is swept around the Coulomb peak. It is interesting that the Q -factor increases at the left slope of the peak and decreases at the right slope compared to its equilibrium values. Thus, electron transport through the quantum dot was shown to lead to both damping and amplification of the mechanical motion. The observed Q -factor variance is of the order of tens of percents, which is quite large. Furthermore, the back-action of a QPC on the resonator motion was also measured, and the results were attributed to the heating effects.

In the case of a single quantum dot at zero source–drain voltage, the system states in which electron tunneling is allowed can be always identified by electrical measurements (if we neglect the experimental limitations on the measurability of ultra-small currents) [269]. In the case of serially connected double quantum dots [270, 271], the situation is different, here for an electron to tunnel though, the electrochemical potential of the double quantum dots system should be equal and coincide with those of the source and drain chemical potentials. In a stability diagram showing the conductance dependence on the voltages applied to individual gates of the dots, this is possible only at specific positions called triple points (see figure 37(a)). There are also states of the system allowing electrons to tunnel between a quantum dot and the nearest Fermi sea, or, alternatively, between the dots. In these states, the system as a whole is insulating (if co-tunneling and inelastic processes are neglected), and the events of these types cannot be detected and studied using the ordinary electron transport measurements. In the stability diagram, these states are described by the lines connecting the triple points (see figure 37(a)). To visualize them, a nearby QPC can be used as a sensitive electrometer. Recently it was shown that these insulating states can be also detected if the double quantum dot is placed on a nanomechanical resonator, such as a suspended carbon nanotube [213]. It was experimentally shown

that the stability diagram of such system can be built by measuring the resonant frequency dependence on the gate voltages. Given AlGaAs/GaAs multiple quantum dots attract are promising candidates for spin qubits [272], investigation of the nanoelectromechanical systems on their basis could possibly lead to their applications for novel read-out techniques.

5. Conclusion

The observed studies show that almost any mesoscopic system, when suspended, can potentially demonstrate novel effects related to enhanced inter-electron interaction and large charging energy, weakened thermal anchoring to the substrate, phonon quantization, strong electron–phonon interaction, additional mechanical degrees of freedom, giant acoustoelectric current, enhanced LSOC effect and other specific features. Due to the listed peculiarities, the suspended nanostructures such as QPCs, 2DEG, quantum dots and nanomechanical resonators become a unique experimental test site for studying the phenomena of electron and phonon transport under specific unusual conditions. These effects may be promising for interdisciplinary research in such fields as nanoelectromechanical systems, phonon lasing, quantum computing, spin devices, sensors of various physical quantities and many others. Future progress in the study of suspended nanostructures may originate from investigation of the phenomena that are well-known, but not yet studied in suspended nanostructures, such as the weak localization, Pauli spin blockade, fractional QHE, spin-related phenomena etc.

Acknowledgment

We are grateful to RFBR and the Royal Society (RS), London (Project Number 21-52-10013) the UKRI Future Leaders Fellowship (MR/S015728/1) and the Royal Society (IEC\R2\202165) for financial support.

Data availability statement

The data that support the findings of this study are available upon reasonable request from the authors.

ORCID iDs

A G Pogosov  <https://orcid.org/0000-0001-5310-4231>

S Kumar  <https://orcid.org/0000-0002-5195-0175>

References

- [1] Beenakker C W J and van Houten H 1991 Quantum transport in semiconductor nanostructures *Semiconductor Heterostructures and Nanostructures* (Amsterdam: Elsevier) pp 1–228
- [2] Pogosov A G, Budantsev M V, Shevyrin A A, Zhdanov E Y and Pokhabov D A 2017 Electron transport *Advances in Semiconductor Nanostructures* (Amsterdam: Elsevier) pp 101–29
- [3] Beck R G, Eriksson M A, Topinka M A, Westervelt R M, Maranowski K D and Gossard A C 1998 *Appl. Phys. Lett.* **73** 1149–51

- [4] Yamaguchi H 2017 *Semicond. Sci. Technol.* **32** 103003
- [5] Blick R, Roukes M, Wegscheider W and Bichler M 1998 *Physica B* **249–251** 784–7
- [6] H ohberger E M, Kirschbaum J, Blick R H, Kotthaus J P and Wegscheider W 2003 *Physica E* **18** 99–100
- [7] Tighe T S, Worlock J M and Roukes M L 1997 *Appl. Phys. Lett.* **70** 2687–9
- [8] Blick R H, Monzon F G, Wegscheider W, Bichler M, Stern F and Roukes M L 2000 *Phys. Rev. B* **62** 17103–7
- [9] van Wees B J, van Houten H, Beenakker C W J, Williamson J G, Kouwenhoven L P, van der Marel D and Foxon C T 1988 *Phys. Rev. Lett.* **60** 848–50
- [10] Wharam D A *et al* 1988 *J. Phys. C: Solid State Phys.* **21** L209–14
- [11] van Wees B J, Kouwenhoven L P, Willems E M M, Harmans C J P M, Mooij J E, van Houten H, Beenakker C W J, Williamson J G and Foxon C T 1991 *Phys. Rev. B* **43** 12431–53
- [12] Yacoby A and Imry Y 1990 *Phys. Rev. B* **41** 5341–50
- [13] B uttiker M 1990 *Phys. Rev. B* **41** 7906–9
- [14] van der Marel D and Haanappel E G 1989 *Phys. Rev. B* **39** 7811–20
- [15] Meyer J S and Matveev K A 2008 *J. Phys.: Condens. Matter.* **21** 023203
- [16] Glazman L I and Khaetskii A V 1989 *Europhys. Lett.* **9** 263–7
- [17] Patel N K *et al* 1990 *J. Phys.: Condens. Matter.* **2** 7247–54
- [18] Patel N K, Nicholls J T, Martn-Moreno L, Pepper M, Frost J E F, Ritchie D A and Jones G A C 1991 *Phys. Rev. B* **44** 13549–55
- [19] Thomas K J, Nicholls J T, Simmons M Y, Pepper M, Mace D R and Ritchie D A 1996 *Phys. Rev. Lett.* **77** 135–8
- [20] Thomas K J, Nicholls J T, Appleyard N J, Simmons M Y, Pepper M, Mace D R, Tribe W R and Ritchie D A 1998 *Phys. Rev. B* **58** 4846–52
- [21] Kristensen A *et al* 2000 *Phys. Rev. B* **62** 10950–7
- [22] Sushkov O 2001 *Phys. Rev. B* **64** 155319
- [23] Cronenwett S M, Lynch H J, Goldhaber-Gordon D, Kouwenhoven L P, Marcus C M, Hirose K, Wingreen N S and Umansky V 2002 *Phys. Rev. Lett.* **88** 226805
- [24] Berggren K F and Yakimenko I I 2002 *Phys. Rev. B* **66** 085323
- [25] Reilly D J 2005 *Phys. Rev. B* **72** 033309
- [26] Sfigakis F, Graham A C, Thomas K J, Pepper M, Ford C J B and Ritchie D A 2008 *J. Phys.: Condens. Matter.* **20** 164213
- [27] Micolich A P 2011 *J. Phys.: Condens. Matter.* **23** 443201
- [28] Bauer F *et al* 2013 *Nature* **501** 73–8
- [29] Brun B *et al* 2014 *Nat. Commun.* **5** 4290
- [30] Zozoulenko I V and Ihnatsenka S 2008 *J. Phys.: Condens. Matter.* **20** 164217
- [31] Lunde A M, Martino A D, Schulz A, Egger R and Flensberg K 2009 *New J. Phys.* **11** 023031
- [32] Berggren K F and Pepper M 2010 *Phil. Trans. R. Soc. A* **368** 1141–62
- [33] Hew W K, Thomas K J, Pepper M, Farrer I, Anderson D, Jones G A C and Ritchie D A 2009 *Phys. Rev. Lett.* **102** 056804
- [34] Smith L W, Hew W K, Thomas K J, Pepper M, Farrer I, Anderson D, Jones G A C and Ritchie D A 2009 *Phys. Rev. B* **80** 041306
- [35] Smith L, Hew W, Thomas K, Pepper M, Farrer I, Anderson D, Jones G and Ritchie D 2010 *Physica E* **42** 1114–7
- [36] Hew W, Thomas K, Pepper M, Farrer I, Anderson D, Jones G and Ritchie D 2010 *Physica E* **42** 1118–21
- [37] Kumar S, Thomas K J, Smith L W, Pepper M, Creeth G L, Farrer I, Ritchie D, Jones G and Griffiths J 2014 *Phys. Rev. B* **90** 201304
- [38] Bayat A, Kumar S, Pepper M and Bose S 2017 *Phys. Rev. B* **96** 041116
- [39] Kumar S, Pepper M, Montagu H, Ritchie D, Farrer I, Griffiths J and Jones G 2021 *Appl. Phys. Lett.* **118** 124002
- [40] Ho S C *et al* 2018 *Phys. Rev. Lett.* **121** 106801
- [41] Kumar S, Pepper M, Holmes S, Montagu H, Gul Y, Ritchie D and Farrer I 2019 *Phys. Rev. Lett.* **122** 086803
- [42] Kumar S, Pepper M, Ritchie D, Farrer I and Montagu H 2019 *Appl. Phys. Lett.* **115** 123104
- [43] Chuang P *et al* 2014 *Nat. Nanotechnol.* **10** 35–9
- [44] Awschalom D D and Flatt e M E 2007 *Nat. Phys.* **3** 153–9
- [45] Chen T M, Pepper M, Farrer I, Jones G A C and Ritchie D A 2012 *Phys. Rev. Lett.* **109** 177202
- [46] Debray P *et al* 2009 *Nat. Nanotechnol.* **4** 759–64
- [47] Wan J, Cahay M, Debray P and Newrock R 2009 *Phys. Rev. B* **80** 155440
- [48] Ngo A T, Debray P and Ulloa S E 2010 *Phys. Rev. B* **81** 115328
- [49] Yan C, Kumar S, Thomas K, See P, Farrer I, Ritchie D, Griffiths J, Jones G and Pepper M 2018 *J. Phys.: Condens. Matter.* **30** 08LT01
- [50] Yan C, Kumar S, Pepper M, See P, Farrer I, Ritchie D, Griffiths J and Jones G 2017 *Nanoscale Res. Lett.* **12** 553
- [51] Yan C, Kumar S, Thomas K, Pepper M, See P, Farrer I, Ritchie D, Griffiths J P and Jones G A C 2017 *Appl. Phys. Lett.* **111** 042107
- [52] Pokhobov D A, Pogosov A G, Zhdanov E Y, Shevyrin A A, Bakarov A K and Shklyayev A A 2018 *Appl. Phys. Lett.* **112** 082102
- [53] Pokhobov D A, Pogosov A G, Zhdanov E Y, Bakarov A K and Shklyayev A A 2019 *Appl. Phys. Lett.* **115** 152101
- [54] Pokhobov D A, Pogosov A G, Zhdanov E Y, Bakarov A K and Shklyayev A A 2020 *Semiconductors* **54** 1605–10
- [55] Pokhobov D A, Pogosov A G, Zhdanov E Y, Bakarov A K and Shklyayev A A 2021 *Appl. Phys. Lett.* **118** 012104
- [56] Kristensen A, Jensen J B, Zaffalon M, S orensen C B, Reimann S M, Lindelof P E, Michel M and Forchel A 1998 *J. Appl. Phys.* **83** 607–9
- [57] Worschech L, Beuscher F and Forchel A 1999 *Appl. Phys. Lett.* **75** 578–80
- [58] Rossler C, Bichler M, Schuh D, Wegscheider W and Ludwig S 2008 *Nanotechnology* **19** 165201
- [59] Pioro-Ladri ere M *et al* 2005 *Phys. Rev. B* **72** 115331
- [60] R ossler C, Herz M, Bichler M and Ludwig S 2010 *Solid State Commun.* **150** 861–4
- [61] Schwab K, Henriksen E A, Worlock J M and Roukes M L 2000 *Nature* **404** 974–7
- [62] Rego L G C and Kirczenow G 1998 *Phys. Rev. Lett.* **81** 232–5
- [63] Angelescu D, Cross M and Roukes M 1998 *Superlattices Microstruct.* **23** 673–89
- [64] Kreft D J, Mourokh L G, Shin H, Bichler M, Wegscheider W and Blick R H 2016 *Phys. Rev. B* **94** 235305
- [65] Mourokh L G, Ivanushkin P, Kreft D J, Shin H, Bichler M, Wegscheider W, Zhao P, Tiemann L and Blick R H 2017 *Appl. Phys. Lett.* **110** 223102
- [66] Rossler C, Hof K D, Manus S, Ludwig S, Kotthaus J P, Simon J, Holleitner A W, Schuh D and Wegscheider W 2008 *Appl. Phys. Lett.* **93** 071107
- [67] Cleland A N, Aldridge J S, Driscoll D C and Gossard A C 2002 *Appl. Phys. Lett.* **81** 1699–701
- [68] Okazaki Y, Mahboob I, Onomitsu K, Sasaki S and Yamaguchi H 2013 *Appl. Phys. Lett.* **103** 192105
- [69] Chaplik A V and Entin M V 1972 *JETP* **34** 1335–9 http://www.jetp.ras.ru/cgi-bin/dn/e_034_06_1335.pdf
- [70] Keldysh L V 1979 *JETP Lett.* **29** 658–61 http://jetpletters.ru/ps/1458/article_22207.pdf
- [71] Pogosov A G, Budantsev M V, Lavrov R A, Plotnikov A E, Bakarov A K, Toropov A I and Portal J C 2006 *JETP Lett.* **83** 122–6
- [72] Pogosov A G, Budantsev M V, Shevyrin A A, Plotnikov A E, Bakarov A K and Toropov A I 2008 *JETP Lett.* **87** 150–3
- [73] Zhdanov E Y, Pogosov A G, Budantsev M V, Pokhobov D A and Bakarov A K 2017 *Semiconductors* **51** 8–13

- [74] Shevyrin A A, Pogosov A G, Budantsev M V, Bakarov A K, Toropov A I, Ishutkin S V and Shesterikov E V 2014 *Appl. Phys. Lett.* **104** 203102
- [75] Schulz H J 1993 *Phys. Rev. Lett.* **71** 1864–7
- [76] Reyes J A and del Castillo-Mussot M 1998 *Phys. Rev. B* **57** 9869–74
- [77] Chaplik A V 1980 *JETP Lett.* **31** 252–4 http://jetpletters.ru/ps/1344/article_20292.pdf
- [78] Mehta A C, Umrigar C J, Meyer J S and Baranger H U 2013 *Phys. Rev. Lett.* **110** 246802
- [79] Pogosov A G, Budantsev M V, Zhdanov E Y, Pokhabov D A, Bakarov A K and Toropov A I 2012 *Appl. Phys. Lett.* **100** 181902
- [80] Gindikina Y and Sablikov V A 2018 *Phys. Rev. B* **98** 115137
- [81] Gindikina Y and Sablikov V A 2019 *Physica E* **108** 187–90
- [82] Dresselhaus G 1955 *Phys. Rev.* **100** 580–6
- [83] Bychkov Y A and Rashba E I 1984 *JETP Lett.* **39** 78–81 http://jetpletters.ru/ps/1264/article_19121.pdf
- [84] Moroz A V and Barnes C H W 1999 *Phys. Rev. B* **60** 14272–85
- [85] Moroz A V and Barnes C H W 2000 *Phys. Rev. B* **61** R2464–7
- [86] Kohda M, Nakamura S, Nishihara Y, Kobayashi K, Ono T, Ohe J-i, Tokura Y, Mineno T and Nitta J 2012 *Nat. Commun.* **3** 1082
- [87] Kokurin I A and Averkiev N S 2015 *JETP Lett.* **101** 568–71
- [88] Wójcik P, Adamowski J, Wołoszyn M and Spisak B J 2015 *J. Appl. Phys.* **118** 014302
- [89] Nowak M P, Kolański K and Szafran B 2014 *Phys. Rev. B* **90** 035301
- [90] Nowak M P and Szafran B 2013 *Appl. Phys. Lett.* **103** 202404
- [91] Datta S and Das B 1990 *Appl. Phys. Lett.* **56** 665–7
- [92] Bhandari N, Dutta M, Charles J, Newrock R S, Cahay M and Herbert S T 2013 *Adv. Nat. Sci.: Nanosci. Nanotechnol.* **4** 013002
- [93] Yan C, Pepper M, See P, Farrer I, Ritchie D and Griffiths J 2020 *Sci. Rep.* **10** 2593
- [94] Wan J, Cahay M, Debray P and Newrock R S 2011 *J. Nano-electron. Optoelectron.* **6** 95–101
- [95] Das P P, Chetry K B, Bhandari N, Wan J, Cahay M, Newrock R S and Herbert S T 2011 *Appl. Phys. Lett.* **99** 122105
- [96] Jones A, Cahay M, Yakimenko I I and Berggren K F 2017 Signatures of spin polarization in four-gate quantum point contact structures *Contemporary Topics in Semiconductor Spintronics* (Singapore: World Scientific) pp 123–58
- [97] Ferrier M, Angers L, Rowe A C H, Guéron S, Bouchiat H, Texier C, Montambaux G and Mailly D 2004 *Phys. Rev. Lett.* **93** 246804
- [98] Bhandari N, Das P P, Cahay M, Newrock R S and Herbert S T 2012 *Appl. Phys. Lett.* **101** 102401
- [99] Das P P, Bhandari N K, Wan J, Charles J, Cahay M, Chetry K B, Newrock R S and Herbert S T 2012 *Nanotechnology* **23** 215201
- [100] Reilly D J *et al* 2001 *Phys. Rev. B* **63** 121311
- [101] Thomas K J, Nicholls J T, Pepper M, Tribe W R, Simmons M Y and Ritchie D A 2000 *Phys. Rev. B* **61** R13365–8
- [102] Crook R, Prance J, Thomas K J, Chorley S J, Farrer I, Ritchie D A, Pepper M and Smith C G 2006 *Science* **312** 1359–62
- [103] Wu P M, Li P, Zhang H and Chang A M 2012 *Phys. Rev. B* **85** 085305
- [104] Thomas K J, Nicholls J T, Simmons M Y, Pepper M, Mace D R and Ritchie D A 1998 *Phil. Mag.* **77** 1213–8
- [105] Chen T M, Graham A C, Pepper M, Farrer I and Ritchie D A 2008 *Appl. Phys. Lett.* **93** 032102
- [106] Das P P, Jones A, Cahay M, Kalita S, Mal S S, Sterin N S, Yadunath T R, Advaita M and Herbert S T 2017 *J. Appl. Phys.* **121** 083901
- [107] Jaksch P, Yakimenko I and Berggren K F 2006 *Phys. Rev. B* **74** 235320
- [108] Das P P, Cahay M, Kalita S, Mal S S and Jha A K 2019 *Sci. Rep.* **9** 12172
- [109] Charles J, Bhandari N, Wan J, Cahay M and Newrock R S 2013 *Appl. Phys. Lett.* **102** 062419
- [110] Wang Z, He J and Guo H 2019 *Physica B* **570** 24–8
- [111] Hasan M Z and Kane C L 2010 *Rev. Mod. Phys.* **82** 3045–67
- [112] Knez I, Rettner C T, Yang S H, Parkin S S, Du L, Du R R and Sullivan G 2014 *Phys. Rev. Lett.* **112** 026602
- [113] de Vries F K *et al* 2018 *Phys. Rev. Lett.* **120** 047702
- [114] Mittag C, Karalic M, Lei Z, Tschirky T, Wegscheider W, Ihn T and Ensslin K 2018 *Appl. Phys. Lett.* **113** 262103
- [115] Mueller S, Mittag C, Tschirky T, Charpentier C, Wegscheider W, Ensslin K and Ihn T 2019 *Phys. Rev. B* **96** 075406
- [116] Masuda T, Sekine K, Nagase K, Wickramasinghe K S, Mishima T D, Santos M B and Hirayama Y 2018 *Appl. Phys. Lett.* **112** 192103
- [117] Castleton I, Davies A, Hamilton A, Frost J, Simmons M, Ritchie D and Pepper M 1998 *Physica B* **249–251** 157–61
- [118] Thomas K J, Nicholls J T, Simmons M Y, Tribe W R, Davies A G and Pepper M 1999 *Phys. Rev. B* **59** 12252–5
- [119] Smith C G *et al* 1989 *J. Phys.: Condens. Matter.* **1** 6763–70
- [120] Simpson P J, Mace D R, Ford C J B, Zailer I, Pepper M, Ritchie D A, Frost J E F, Grimshaw M P and Jones G A C 1993 *Appl. Phys. Lett.* **63** 3191–3
- [121] Suen Y W, Santos M B and Shayegan M 1992 *Phys. Rev. Lett.* **69** 3551–4
- [122] Gumbs G, Huang D, Hon J, Pepper M and Kumar S 2017 *Adv. Phys. X* **2** 545–68
- [123] Meyer J S, Matveev K A and Larkin A I 2007 *Phys. Rev. Lett.* **98** 126404
- [124] Chen J C, Lin Y, Lin K T, Ueda T and Komiyama S 2009 *Appl. Phys. Lett.* **94** 012105
- [125] Friedland K J, Hey R, Kostial H, Klann R and Ploog K 1996 *Phys. Rev. Lett.* **77** 4616–9
- [126] Zarenia M, Neilson D and Peeters F M 2017 *Sci. Rep.* **7** 11510
- [127] Ensslin K and Petroff P M 1990 *Phys. Rev. B* **41** 12307–10
- [128] Hofstadter D R 1976 *Phys. Rev. B* **14** 2239–49
- [129] Albrecht C, Smet J H, von Klitzing K, Weiss D, Umansky V and Schweizer H 2001 *Phys. Rev. Lett.* **86** 147–50
- [130] Geisler M C, Smet J H, Umansky V, von Klitzing K, Naundorf B, Ketzmerick R and Schweizer H 2004 *Phys. Rev. Lett.* **92** 256801
- [131] Lorke A, Kotthaus J P and Ploog K 1991 *Superlattices Microstruct.* **9** 103–6
- [132] Weiss D, Roukes M L, Menschig A, Grambow P, von Klitzing K and Weimann G 1991 *Phys. Rev. Lett.* **66** 2790–3
- [133] Gusev G M, Kvon Z D, Kudryashov V M, Litvin L V, Nastaushv Y V, Dolgoplov V T and Shashkin A A 1991 *JETP Lett.* **54** 364–8 http://jetpletters.ru/ps/1250/article_18904.shtml
- [134] Sinai Y G 1970 *Russ. Math. Surv.* **25** 137–89
- [135] Gusev G M, Kvon Z D, Pogosov A G and Voronin M M 1997 *JETP Lett.* **65** 248–52
- [136] Baskin E M, Pogosov A G and Entin M V 1996 *JETP* **83** 1135–48 <http://jetp.ac.ru/cgi-bin/e/index/e/83/6/p1135?a=list>
- [137] Baskin E M, Gusev G M, Kvon Z D, Pogosov A G and Entin M V 1992 *JETP Lett.* **55** 678–82 http://jetpletters.ru/ps/1278/article_19333.shtml
- [138] Fleischmann R, Geisel T and Ketzmerick R 1992 *Phys. Rev. Lett.* **68** 1367–70
- [139] Budantsev M V, Kvon Z D, Pogosov A G, Plotnikov A E, Moshegov N T and Toropov A I 1996 *JETP Lett.* **63** 347–52
- [140] Budantsev M V, Kvon Z D, Pogosov A G, Moshegov N T, Plotnikov A E and Toropov A I 1996 *Surf. Sci.* **361–362** 739–41
- [141] Tsukagoshi K, Nagao T, Haraguchi M, Takaoka S, Murase K and Gamo K 1998 *Superlattices Microstruct.* **23** 493–7
- [142] Lüthi S, Vancura T, Ensslin K, Schuster R, Böhm G and Klein W 1997 *Phys. Rev. B* **55** 13088–92

- [143] Pogosov A G, Budantsev M V, Lavrov R A, Plotnikov A E, Bakarov A K and Toropov A I 2005 *JETP Lett.* **81** 462–6
- [144] Gusev G M, Kvon Z D, Litvin L V, Nastaushev Y V, Kalagin A K and Toropov A I 1992 *JETP Lett.* **55** 123–6 http://jetpletters.ru/ps/1269/article_19202.shtml
- [145] Budantsev M V, Kvon Z D, Pogosov A G, Litvin L V, Mansurov V G, Migal' V P, Moshchenko S P and Nastaushev Y V 1994 *JETP Lett.* **59** 645–50 http://jetpletters.ru/ps/1310/article_19805.shtml
- [146] Schuster R, Ensslin K, Wharam D, Kühn S, Kotthaus J P, Böhm G, Klein W, Tränkle G and Weimann G 1994 *Phys. Rev. B* **49** 8510–3
- [147] Budantsev M, Kvon Z, Pogosov A and Litvin L 1998 *Superlattices Microstruct.* **24** 291–3
- [148] Budantsev M V, Lavrov R A, Pogosov A G, Plotnikov A E, Bakarov A K, Toropov A I, Maude D K and Portal J C 2004 *JETP Lett.* **79** 166–70
- [149] Gusev G M, Kvon Z D, Pogosov A G and Basmaji P 1996 *JETP* **83** 375–8 <http://jetp.ac.ru/cgi-bin/rt/index/e/83/2/p375?a=list>
- [150] Nihey F and Nakamura K 1993 *Physica B* **184** 398–402
- [151] Dorn A, Sigrist M, Fuhrer A, Ihn T, Heinzl T, Ensslin K, Wegscheider W and Bichler M 2002 *Appl. Phys. Lett.* **80** 252–4
- [152] Nihey F, Kastner M A and Nakamura K 1997 *Phys. Rev. B* **55** 4085–8
- [153] Pouydebasque A, Pogosov A G, Budantsev M V, Plotnikov A E, Toropov A I, Maude D K and Portal J C 2001 *Phys. Rev. B* **64** 245306
- [154] Yang C H, Zheng S Y, Fan J, Jing X N, Ji Z Q, Liu G T, Yang C L and Lu L 2018 *Chin. Phys. Lett.* **35** 077301
- [155] Wang D Q, Reuter D, Wieck A D, Hamilton A R and Klochan O 2020 *Appl. Phys. Lett.* **117** 032102
- [156] Büttiker M 1986 *Phys. Rev. Lett.* **57** 1761–4
- [157] Budantsev M V, Kvon Z D, Pogosov A G, Moschegov N T, Toropov A I and Plotnikov A E 1997 *Proc. 12th Int. Conf., High Magnetic Fields in the Physics of Semiconductors* pp 519–22
- [158] Pogosov A G, Budantsev M V, Uzur D, Nogaret A, Plotnikov A E, Bakarov A K and Toropov A I 2002 *Phys. Rev. B* **66** 201303
- [159] Bolotin K, Sikes K, Jiang Z, Klima M, Fudenberg G, Hone J, Kim P and Stormer H 2008 *Solid State Commun.* **146** 351–5
- [160] Wang L 2017 *Doctoral Dissertation* University of South Carolina <https://scholarcommons.sc.edu/etd/4257/>
- [161] Hühberger E, Blick R, Beil F, Wegscheider W, Bichler M and Kotthaus J 2002 *Physica E* **12** 487–90
- [162] Pogosov A G, Budantsev M V, Zhdanov E Y and Pokhobov D A 2013 *Ballistic Electron Transport in Structured Suspended Semiconductor Membranes* vol 1566 (New York: AIP) pp 211–2
- [163] Gurevich L 1946 *J. Phys. USSR* **10** 67
- [164] Schmidt M, Schneider G, Heyn C, Stemmann A and Hansen W 2012 *Phys. Rev. B* **85** 075408
- [165] Zhdanov E Y, Pogosov A G, Budantsev M V, Pokhobov D A, Bakarov A K and Toropov A I 2015 *J. Phys.: Conf. Ser.* **643** 012079
- [166] von Klitzing K, Dorda G and Pepper M 1980 *Phys. Rev. Lett.* **45** 494–7
- [167] Tang F *et al* 2019 *Nature* **569** 537–41
- [168] Budantsev M V, Pokhobov D A, Pogosov A G, Zhdanov E Y, Bakarov A K and Toropov A I 2014 *Semiconductors* **48** 1423–31
- [169] Pokhobov D A, Pogosov A G, Budantsev M V, Zhdanov E Y and Bakarov A K 2016 *Semiconductors* **50** 1049–53
- [170] Zhang Y, Tan Y W, Stormer H L and Kim P 2005 *Nature* **438** 201–4
- [171] McIver J W, Schulte B, Stein F U, Matsuyama T, Jotzu G, Meier G and Cavalleri A 2019 *Nat. Phys.* **16** 38–41
- [172] König M, Wiedmann S, Brune C, Roth A, Buhmann H, Molenkamp L W, Qi X L and Zhang S C 2007 *Science* **318** 766–70
- [173] Yu R, Zhang W, Zhang H J, Zhang S C, Dai X and Fang Z 2010 *Science* **329** 61–4
- [174] Tsui D C, Stormer H L and Gossard A C 1982 *Phys. Rev. Lett.* **48** 1559–62
- [175] Chklovskii D B, Shklovskii B I and Glazman L I 1992 *Phys. Rev. B* **46** 4026–34
- [176] Matthews J and Cage M E 2005 *J. Res. Natl. Inst. Stand. Technol.* **110** 497
- [177] Schmidt M, Schneider G, Heyn C, Stemmann A and Hansen W 2011 *J. Electron. Mater.* **41** 1286–9
- [178] Chen C, Farrer I, Holmes S N, Sfigakis F, Fletcher M P, Beere H E and Ritchie D A 2015 *J. Cryst. Growth* **425** 70–5
- [179] Chen C, Holmes S N, Farrer I, Beere H E and Ritchie D A 2020 *Appl. Phys. Lett.* **116** 232106
- [180] Eber G, von Klitzing K, Ploog K and Weinmann G 1983 *J. Phys. C: Solid State Phys.* **16** 5441–8
- [181] Klauβ U, Dietsche W, von Klitzing K and Ploog K 1991 *Physica B* **169** 363–7
- [182] Eaves L and Sheard F W 1986 *Semicond. Sci. Technol.* **1** 346–9
- [183] Balaban N Q, Meirav U, Shtrikman H and Levinson Y 1993 *Phys. Rev. Lett.* **71** 1443–6
- [184] Komiyama S and Kawaguchi Y 2000 *Phys. Rev. B* **61** 2014–27
- [185] Prinz V, Seleznev V, Gutakovskiy A, Chehovskiy A, Preobrazhenskii V, Putyato M and Gavrillova T 2000 *Physica E* **6** 828–31
- [186] Lorke A, Böhm S and Wegscheider W 2003 *Superlattices Microstruct.* **33** 347–56
- [187] Vorob'ev A B, Friedland K J, Kostial H, Hey R, Jahn U, Wiebicke E, Yukecheva J S and Prinz V Y 2007 *Phys. Rev. B* **75** 205309
- [188] Müller J E 1992 *Phys. Rev. Lett.* **68** 385–8
- [189] Hofstetter E, Taylor J M C and MacKinnon A 1996 *Phys. Rev. B* **53** 4676–83
- [190] Schmid S, Villanueva L G and Roukes M L 2016 *Fundamentals of Nanomechanical Resonators* (Berlin: Springer)
- [191] Cleland A N 2003 *Foundations of Nanomechanics: From Solid-State Theory to Device Applications* (Berlin: Springer)
- [192] Mahboob I and Yamaguchi H 2016 *Nanomechanical Resonators Based on III–V Semiconductors* (Berlin: Springer) pp 2523–39
- [193] Greenberg Y, Pashkin Y A and Il'ichev E 2012 *Phys.-Usp.* **55** 382–407
- [194] Landau L D, Lifshitz E, Kosevich A and Pitaevskii L 1986 *Chapter III—Elastic Waves* 3rd edn (Oxford: Butterworth-Heinemann) pp 87–107
- [195] Chaste J, Eichler A, Moser J, Ceballos G, Rurali R and Bachtold A 2012 *Nat. Nanotechnol.* **7** 301–4
- [196] Adiga V P, Ilic B, Barton R A, Wilson-Rae I, Craighead H G and Parpia J M 2012 *J. Appl. Phys.* **112** 064323
- [197] Mamin H J and Rugar D 2001 *Appl. Phys. Lett.* **79** 3358–60
- [198] Cleland A N and Roukes M L 1998 *Nature* **392** 160–2
- [199] Lifshitz R and Cross M C 2008 *Nonlinear Dynamics of Nanomechanical and Micromechanical Resonators* (New York: Wiley) ch 1 pp 1–52 <https://onlinelibrary.wiley.com/doi/pdf/10.1002/9783527626359.ch1>
- [200] Ochs J S, Seitner M, Dykman M I and Weig E M 2021 *Phys. Rev. A* **103** 013506
- [201] Mahboob I and Yamaguchi H 2008 *Nat. Nanotechnol.* **3** 275–9
- [202] Kim C, Marsland R and Blick R H 2020 *Small* **16** 2001580
- [203] Poot M and van der Zant H S 2012 *Phys. Rep.* **511** 273–335
- [204] Cleland A N and Roukes M L 1996 *Appl. Phys. Lett.* **69** 2653–5
- [205] Carr D W, Evoy S, Sekaric L, Craighead H G and Parpia J M 1999 *Appl. Phys. Lett.* **75** 920–2

- [206] Presnov D E, Kafanov S G, Dorofeev A A, Bozhev I V, Trifonov A S, Pashkin Y A and Krupenin V A 2018 *JETP Lett.* **108** 492–7
- [207] Sampathkumar A, Murray T W and Ekinici K L 2006 *Appl. Phys. Lett.* **88** 223104
- [208] Huang X M H, Feng X L, Zorman C A, Mehregany M and Roukes M L 2005 *New J. Phys.* **7** 247
- [209] Truitt P A, Hertzberg J B, Huang C C, Ekinici K L and Schwab K C 2007 *Nano Lett.* **7** 120–6
- [210] Unterreithmeier Q P, Faust T and Kotthaus J P 2010 *Phys. Rev. Lett.* **105** 027205
- [211] Cleland A N, Pophristic M and Ferguson I 2001 *Appl. Phys. Lett.* **79** 2070–2
- [212] Sazonova V, Yaish Y, Üstünel H, Roundy D, Arias T A and McEuen P L 2004 *Nature* **431** 284–7
- [213] Khivrich I, Clerck A A and Ilani S 2019 *Nat. Nanotechnol.* **14** 161–7
- [214] Lassagne B, Tarakanov Y, Kinaret J, Garcia-Sanchez D and Bachtold A 2009 *Science* **325** 1107–10
- [215] Bunch J S, van der Zande A M, Verbridge S S, Frank I W, Tanenbaum D M, Parpia J M, Craighead H G and McEuen P L 2007 *Science* **315** 490–3
- [216] Weber P, Güttinger J, Noury A, Vergara-Cruz J and Bachtold A 2016 *Nat. Commun.* **7** 12496
- [217] Favero I 2014 *Gallium Arsenide Disks as Optomechanical Resonators* (Berlin: Springer) pp 149–56
- [218] Favero I, Sankey J and Weig E M 2014 *Mechanical Resonators in the Middle of an Optical Cavity* (Berlin: Springer) pp 83–119
- [219] Masmanidis S C, Karabalin R B, De Vlaminck I, Borghs G, Freeman M R and Roukes M L 2007 *Science* **317** 780–3
- [220] Shevyrin A A, Bakarov A K, Shklyayev A A, Arakcheev A S, Kurosu M, Yamaguchi H and Pogosov A G 2019 *JETP Lett.* **109** 261–5
- [221] Shevyrin A A, Pogosov A G, Bakarov A K and Shklyayev A A 2021 *Appl. Phys. Lett.* **118** 183105
- [222] Shevyrin A A, Pogosov A G, Budantsev M V, Bakarov A K, Toropov A I, Rodyakina E E and Shklyayev A A 2015 *Appl. Phys. Lett.* **106** 183110
- [223] Oda Y, Onomitsu K, Kometani R, Warisawa S-i, Ishihara S and Yamaguchi H 2011 *Japan. J. Appl. Phys.* **50** 06GJ01
- [224] Shevyrin A A, Pogosov A G, Bakarov A K and Shklyayev A A 2016 *Phys. Rev. Lett.* **117** 017702
- [225] Hamoumi M, Allain P E, Hease W, Gil-Santos E, Morgenroth L, Gérard B, Lemaître A, Leo G and Favero I 2018 *Phys. Rev. Lett.* **120** 223601
- [226] Okamoto H, Ito D, Onomitsu K and Yamaguchi H 2008 *Phys. Status Solidi c* **5** 2920–2
- [227] Harrington D A, Mohanty P and Roukes M L 2000 *Physica B* **284–288** 2145–6
- [228] Shevyrin A A, Pogosov A G, Bakarov A K and Shklyayev A A 2020 *Appl. Phys. Lett.* **116** 053104
- [229] Yamaguchi H, Kato K, Nakai Y, Onomitsu K, Warisawa S and Ishihara S 2008 *Appl. Phys. Lett.* **92** 251913
- [230] Beck R G, Eriksson M A, Westervelt R M, Campman K L and Gossard A C 1996 *Appl. Phys. Lett.* **68** 3763–5
- [231] Tang H X, Huang X M H, Roukes M L, Bichler M and Wegscheider W 2002 *Appl. Phys. Lett.* **81** 3879–81
- [232] Yamaguchi H, Okamoto H, Ishihara S and Hirayama Y 2012 *Appl. Phys. Lett.* **100** 012106
- [233] Harris J G E, Knobel R, Maranowski K D, Gossard A C, Samarth N and Awschalom D D 2001 *Phys. Rev. Lett.* **86** 4644–7
- [234] Knobel R and Cleland A N 2002 *Appl. Phys. Lett.* **81** 2258–60
- [235] Knobel R G and Cleland A N 2003 *Nature* **424** 291–3
- [236] Kirschbaum J, Höhberger E M, Blick R H, Wegscheider W and Bichler M 2002 *Appl. Phys. Lett.* **81** 280–2
- [237] Okazaki Y, Mahboob I, Onomitsu K, Sasaki S and Yamaguchi H 2016 *Nat. Commun.* **7** 11132
- [238] Shevyrin A A, Pogosov A G, Budantsev M V, Bakarov A K, Toropov A I, Ishutkin S V, Shesterikov E V and Arakcheev A S 2013 *Appl. Phys. Lett.* **103** 131905
- [239] Shevyrin A A *et al* 2012 *Appl. Phys. Lett.* **101** 241916
- [240] Klots A R *et al* 2014 *Sci. Rep.* **4** 6608
- [241] Xie H, Jiang S, Shan J and Mak K F 2018 *Nano Lett.* **18** 3213–20
- [242] Xie H, Jiang S, Rhodes D A, Hone J C, Shan J and Mak K F 2021 *Nano Lett.* **21** 2538–43
- [243] Zhou Y *et al* 2020 *Phys. Rev. Lett.* **124** 027401
- [244] Kouh T, Hanay M S and Ekinici K L 2017 *Micromachines* **8** 108
- [245] Ekinici K L 2005 *Small* **1** 786–97
- [246] Koenig D R, Weig E M and Kotthaus J P 2008 *Nat. Nanotechnol.* **3** 482–5
- [247] Bargatin I, Myers E B, Arlett J, Gudlewski B and Roukes M L 2005 *Appl. Phys. Lett.* **86** 133109
- [248] Lavrik N V and Datskos P G 2003 *Appl. Phys. Lett.* **82** 2697–9
- [249] Ilic B, Krylov S, Aubin K, Reichenbach R and Craighead H G 2005 *Appl. Phys. Lett.* **86** 193114
- [250] Chadi D J and Chang K J 1989 *Phys. Rev. B* **39** 10063–74
- [251] Mooney P M 1990 *J. Appl. Phys.* **67** R1–26
- [252] Mohanty P, Harrington D A, Ekinici K L, Yang Y T, Murphy M J and Roukes M L 2002 *Phys. Rev. B* **66** 085416
- [253] Takagaki Y, Kosugi T, Gamo K, Namba S and Murase K 1990 *Semicond. Sci. Technol.* **5** 634–7
- [254] Verbridge S S, Ilic R, Craighead H G and Parpia J M 2008 *Appl. Phys. Lett.* **93** 013101
- [255] Bückle M, Hauber V C, Cole G D, Gärtner C, Zeimer U, Grenzer J and Weig E M 2018 *Appl. Phys. Lett.* **113** 201903
- [256] Shevyrin A A and Pogosov A G 2018 *J. Phys.: Condens. Matter.* **30** 184003
- [257] Imboden M and Mohanty P 2014 *Phys. Rep.* **534** 89–146
- [258] Photiadis D M and Judge J A 2004 *Appl. Phys. Lett.* **85** 482–4
- [259] Kunal K and Aluru N R 2011 *Phys. Rev. B* **84** 245450
- [260] Lifshitz R and Roukes M L 2000 *Phys. Rev. B* **61** 5600–9
- [261] Nowick A and Berry B (ed) 1972 *Anelastic Relaxation in Crystalline Solids* (New York: Academic)
- [262] Sparks P W and Swenson C A 1967 *Phys. Rev.* **163** 779–90
- [263] Watanabe M O, Morizuka K, Mashita M, Ashizawa Y and Zohta Y 1984 *Japan. J. Appl. Phys.* **23** L103–5
- [264] fu Li M, Yu P Y and Weber R E 1992 *Appl. Phys. Lett.* **60** 1404
- [265] Onomitsu K, Mitsuhara M, Yamamoto H and Yamaguchi H 2013 *Appl. Phys. Express* **6** 111201
- [266] Yamaguchi H, Tokura Y, Miyashita S and Hirayama Y 2004 *Phys. Rev. Lett.* **93** 036603
- [267] Nishiguchi N 2003 *Phys. Rev. B* **68** 121305
- [268] Weig E M, Blick R H, Brandes T, Kirschbaum J, Wegscheider W, Bichler M and Kotthaus J P 2004 *Phys. Rev. Lett.* **92** 046804
- [269] Kouwenhoven L P, Marcus C M, McEuen P L, Tarucha S, Westervelt R M and Wingreen N S 1997 *Electron Transport in Quantum Dots* (Berlin: Springer) pp 105–214
- [270] van der Wiel W G, De Franceschi S, Elzerman J M, Fujisawa T, Tarucha S and Kouwenhoven L P 2002 *Rev. Mod. Phys.* **75** 1–22
- [271] Hanson R, Kouwenhoven L P, Petta J R, Tarucha S and Vandersypen L M K 2007 *Rev. Mod. Phys.* **79** 1217–65
- [272] Elzerman J M, Hanson R, Willems van Beveren L H, Vandersypen L M K and Kouwenhoven L P 2006 *Semiconductor Few-Electron Quantum Dots as Spin Qubits* (New York: Springer) pp 298–305